

<b>REPORT DOCUMENTATION PAGE</b>			Form Approved OMB NO. 0704-0188	
Public Reporting burden for this collection of information is estimated to average 1 hour per response, including the time for reviewing instructions, searching existing data sources, gathering and maintaining the data needed, and completing and reviewing the collection of information. Send comment regarding this burden estimates or any other aspect of this collection of information, including suggestions for reducing this burden, to Washington Headquarters Services, Directorate for information Operations and Reports, 1215 Jefferson Davis Highway, Suite 1204, Arlington, VA 22202-4302, and to the Office of Management and Budget, Paperwork Reduction Project (0704-0188,) Washington, DC 20503.				
1. AGENCY USE ONLY ( Leave Blank)		2. REPORT DATE		3. REPORT TYPE AND DATES COVERED
4. TITLE AND SUBTITLE			5. FUNDING NUMBERS	
6. AUTHOR(S)				
7. PERFORMING ORGANIZATION NAME(S) AND ADDRESS(ES)			8. PERFORMING ORGANIZATION REPORT NUMBER	
9. SPONSORING / MONITORING AGENCY NAME(S) AND ADDRESS(ES)  U. S. Army Research Office P.O. Box 12211 Research Triangle Park, NC 27709-2211			10. SPONSORING / MONITORING AGENCY REPORT NUMBER	
11. SUPPLEMENTARY NOTES The views, opinions and/or findings contained in this report are those of the author(s) and should not be construed as an official Department of the Army position, policy or decision, unless so designated by other documentation.				
12 a. DISTRIBUTION / AVAILABILITY STATEMENT  Approved for public release; distribution unlimited.			12 b. DISTRIBUTION CODE	
13. ABSTRACT (Maximum 200 words)				
14. SUBJECT TERMS			15. NUMBER OF PAGES	
			16. PRICE CODE	
17. SECURITY CLASSIFICATION OR REPORT <b>UNCLASSIFIED</b>	18. SECURITY CLASSIFICATION ON THIS PAGE <b>UNCLASSIFIED</b>	19. SECURITY CLASSIFICATION OF ABSTRACT <b>UNCLASSIFIED</b>	20. LIMITATION OF ABSTRACT  <b>UL</b>	

NSN 7540-01-280-5500

**Standard Form 298 (Rev.2-89)**  
Prescribed by ANSI Std. Z39-18  
298-102

Enclosure 1

## Table of Contents

Table of Contents .....	2
List of Figures .....	4
List of Tables .....	8
1. Objectives .....	9
2. Executive Summary .....	9
2.1 Recommendations: .....	12
3. MURI Team Structure .....	13
4. Major Accomplishments .....	14
5. Systems Engineering .....	16
5.1 System Level Modeling .....	18
5.2 Computational Fluid Dynamics Analysis of Fuel Cells .....	19
5.3 Intermediate Fidelity Models .....	20
5.4 Fundamental techniques .....	21
6. Microfabricated Fuel Processors .....	21
6.1 Overall Heat Loss and Energy Balance .....	23
6.2 Catalyst Preparation and Localization Using Fluidic Stop Valve .....	24
6.3 Autothermal Hydrogen Generation .....	26
6.3.1 Summary of Reaction Testing Results .....	28
6.4 Thermophotovoltaic Power Generation .....	29
6.5 Next Generation Microfabricated Fuel Processors .....	30
6.5.1 Suspended micro-reactor version III (SμRE III) .....	31
6.5.2 Microfabricated Fuel Processors by KOH Etching .....	33
6.6 Palladium-Based Micromembranes for Hydrogen Purification .....	35
6.7 Use of Reforming Catalysts in Palladium-Based Micromembranes for Ultra-Pure Hydrogen Generation .....	37
6.7.1 Autothermal Reforming of Methanol for Solid Oxide Fuel Cells .....	40
6.8 Vacuum Packaging .....	43
7. Catalysts for Reforming and Solid Oxide Fuels Cells .....	44
7.1 Oxidative Steam Reforming of Methanol .....	44
7.2 Steam Reforming of Propane .....	45
7.3 Alternative Anode Materials for Direct Hydrocarbon Conversion .....	46
7.4 Exploring Materials for Proton Conducting Solid Oxide Fuel Cells .....	49
8. Microfabricated Solid Oxide Fuel Cells .....	52
8.1 Greatly Enhanced Platinum Electrode Performance on Thin Film YSZ .....	53
8.2 Materials and Structural Analysis for Micro SOFC .....	57
8.3 Residual Stress and Microstructural Characterization of YSZ Material .....	57
8.4 Evolution of Residual Stress with Thermal Cycling of YSZ and Trilayer Stack .....	58
8.5 Elastic Property Characterization of Thin Film YSZ .....	59
8.6 Structural and Electrochemical Characterization of Two Proton Conducting Oxide Thin Films .....	60

8.7	Development of Large Free-Standing Electrolyte-supported Micro Fuel Cell Membranes.....	61
8.8	Fabrication and Testing of Electrolyte-supported Ultra-thin Film Fuel Cells .....	63
8.9	Girder-Grid Support Structure Design and Fabrication.....	64
9	Recommendations .....	68
10	References .....	68
11	MURI Program Statistics .....	70
11.1	Publications .....	70
11.1.1	Papers published in peer-reviewed journals.....	70
11.1.2	Papers published in non-peer-reviewed journals or in conference proceedings .....	72
11.1.3	Papers presented at meetings, but not published in conference proceedings .....	74
11.1.4	Manuscripts submitted, but not published .....	82
11.2	MURI Personnel.....	82
11.2.1	Graduate Students Supported.....	82
11.2.2	Post Doctorates Supported.....	83
11.2.3	Faculty Supported .....	83
11.2.4	Under Graduate Students:.....	83
11.2.5	PhDs Awarded: 7 .....	84
11.2.6	Master Degrees Awarded: 5 .....	84

## List of Figures

Figure 1: Overview of research thrust areas. ....	14
Figure 2: Methodology overview.....	17
Figure 3: Examples of interactions of methodology with rest of MURI effort .....	17
Figure 4: Conceptual illustration of considered processes .....	18
Figure 5: Effect of scale on process performance.....	19
Figure 6: Temperature (left) and velocity distribution (right) in the vertical heat exchanger of SµREIII (see Section 6.6.1) reactor.....	19
Figure 7: Conceptual process flowsheet for the intermediate fidelity modeling case-study. ....	20
Figure 8: Ratio between heat losses and electrical power (left plot) and optimal design parameters (right plot) vs. operating temperature, for a nominal power output of 1W. 20	
Figure 9: Optimal power profiles at startup for a nominal power output of 1W. ....	21
Figure 10: Schematic of the suspended-tube reactor. In the fabricated device, each tube is 200 µm wide by ~480 µm high. While a three-slab configuration is shown in this figure, the number of slabs can be varied. The silicon slabs wrap completely around each. ..	22
Figure 11: Illustration of how the suspended-tube reactor is used for simultaneous combustion and hydrogen production. The combustion heats up the entire silicon reaction zone at the end of the tubes so that endothermic hydrogen production may take place. Vacuum packaging and reflective shields, required to maximize the thermal isolation of the reaction zone, have been tested independently, but have yet to be integrated into the device. ....	22
Figure 12: Predicted steady-state heat loss and heat generation for a reactor at 800°C as a function of flow rate within each tube. (a) Combustion in single tube and (b) combustion in both tubes. The generation lines correspond to full conversion of a stoichiometric fuel/air mixture at the given flow rate in one channel. The “other fuels” includes butane, propane, methanol, and ammonia. ....	24
Figure 13: Procedure for introducing catalyst washcoats such that catalyst is not deposited in the inlet tube. ....	25
Figure 14: Enhanced contrast micrograph of water loaded into a channel containing a fluidic stop valve. The surfaces have been silanized with OTS to increase their hydrophobicity. The inset shows how this technique can be used to control the catalyst deposition within the suspended-tube reactor (catalyst is white). A glass-capped, oxidized silicon test wafer was used for the visualization. ....	26
Figure 15: Sequence of images (over the course of ~ 10 s) showing the ignition of hydrogen in the bottom channel of the reactor, with ammonia flowing in the top channel. ....	27
Figure 16: Ammonia conversion (stoichiometric combustion in simulated air) and autothermal reaction temperature as a function of ambient pressure during simultaneous combustion/cracking. Ammonia flow rate to the combustion side is 2 sccm. Ammonia flow to the cracking side is 10 sccm. ....	28

Figure 17: Schematic and photograph of the suspended-tube reactor in a TPV micro-generator configuration. ....	30
Figure 18: Stable and autothermal propane combustion in the suspended tube reactor. ....	30
Figure 19: S $\mu$ RE III schematics, (a) top view, (b) cross-section showing suspended silicon nitride tubes, heat exchangers and reaction chamber (grey = silicon, green = silicon nitride, blue = silicon dioxide, yellow = platinum). ....	31
Figure 20: S $\mu$ RE III fabricated device, top (a) and back (b) views. Rounding of corners is an etch artifacts. (c) Fracture S $\mu$ RE III device, showing reaction chamber, 2 sets of 8 tubes, and one heat exchanger. ....	32
Figure 21: Matching of vacuum data from S $\mu$ RE III with thermal model. ....	32
Figure 22: Fabrication outline for the (a) reaction zone and (b) supporting frame ....	33
Figure 23: Assembled micro fuel processor ....	34
Figure 24: Vacuum chuck assembly ....	34
Figure 25: H <sub>2</sub> combustion in atmosphere. ....	35
Figure 26: H <sub>2</sub> combustion at 50 mTorr ....	35
Figure 27: Catalytic combustion of propane. Wires are thermocouples for temperature measurements. ....	35
Figure 28: Reactor configuration for simultaneous combustion and reforming (left expanded view, right compact unit after bonding) ....	35
Figure 29: The palladium micromembrane architecture for purification of hydrogen. ....	36
Figure 30: Thermodynamic analysis of methanol partial oxidation. ....	37
Figure 31: SEM images of 23 weight % silver-palladium film (200 nm) after prolonged (24 hr) exposure to 5% methanol in helium at 400°C. ....	38
Figure 32: Conversion and selectivity of methanol partial oxidation over La <sub>0.95</sub> Co <sub>0.05</sub> NiO <sub>3-<math>\delta</math></sub> and Pd/Al <sub>2</sub> O <sub>3</sub> . O <sub>2</sub> /methanol feed = 0.5, SV = 4,500 ml/(g cat-min). ....	38
Figure 33: SEM images of the catalyst coating at clockwise increasing magnification: (a) uncoated silver-palladium membrane, (b) catalyst-coated membrane, (c) catalyst coating (2300x magnification), and (d) catalyst coating (13,000x magnification). ....	39
Figure 34: Results obtained for 23 weight % silver-palladium film washcoated with 1.69 gm of 8:1 LaNi <sub>0.95</sub> Co <sub>0.05</sub> O <sub>3</sub> / Al <sub>2</sub> O <sub>3</sub> catalyst, (a) at constant membrane temperature of 400°C and varying O <sub>2</sub> :CH <sub>3</sub> OH ratio, and (b) for varying membrane temperature. ....	40
Figure 35: Integrated reformer-burner unit for autothermal reforming of methanol. Left: Schematic of assembled unit. Right: Layout for silicon microfabrication. ....	41
Figure 36: Energy balance for reformer-burner unit. ....	42
Figure 37: Fabricated reformer-burner units. Left: burner and reformer units on wafer. Right: packaged device with fluidic connections. ....	42
Figure 38: Hydrogen permeation results. ....	43

Figure 39: Two-Step Bonding Process (black = silicon, blue = frit, yellow = metallization, orange = solder/glass).....	43
Figure 40: (■) Conversion, (♦) hydrogen and (▲) carbon dioxide selectivities, and (×) post-bed temperature for oxidative steam reforming of methanol over $\text{LaNiO}_3$ (left) and 5 wt% Pd/ $\text{Al}_2\text{O}_3$ (right) under full-fuel conditions. The reaction was conducted at a space velocity of $550,000 \text{ hr}^{-1}$ with a water/methanol ratio of 3 using simulated air as the oxygen source.....	45
Figure 41: $\text{LaNiO}_3$ film was deposited with fine porosity to catalyze the reaction without significantly lowering the permeability of the underlying Pd membrane. ....	45
Figure 42: (■) Hydrogen and (▲) carbon dioxide selectivities obtained on the reformat side of the Pd membrane microreactor at $400^\circ\text{C}$ . The reaction was conducted at a space velocity of $350 \text{ L}/(\text{g}_{\text{cat}}\cdot\text{hr})$ using a dilute 4% methanol feed without steam addition....	45
Figure 43: (a) $\text{H}_2$ yield, and (b) $\text{CH}_4$ , (c) $\text{CO}$ and (d) $\text{CO}_2$ selectivities as a function of reaction temperature for (—) 15 mol% Ni-coated BHA and (---) nickel aluminate with $\text{Ni}/\text{Al} = 0.75$ .....	46
Figure 44: XRD patterns for (a) Ni-Sn/YSZ cermet prepared by reduction of the oxide composite, and (b) Ni-Sn/YSZ cermet and (c) Ni/YSZ cermet after exposure to dry methane at $800^\circ\text{C}$ . $\text{Ni}_3\text{Sn}_1$ (1), $\text{Ni}_3\text{Sn}_2$ (2), Ni (+), YSZ (*), and carbon (#) peaks are denoted. ....	48
Figure 45: % size increase (solid lines) and % weight increase (dashed lines) in (■) Ni/YSZ and (▲) Ni-Sn/YSZ cermet anodes after exposure to dry methane at $800^\circ\text{C}$ for 1.5 h. ....	48
Figure 46: Cell potential (solid lines) and power density (dashed lines) for (left) Ni-Sn/YSZ and (right) Ni/YSZ anodes in humidified hydrogen at (•) $700^\circ\text{C}$ , (▲) $750^\circ\text{C}$ and (■) $800^\circ\text{C}$ .....	49
Figure 47: Cell potential (solid lines) and power density (dashed lines) for Ni-Sn/YSZ anode-supported cell in humidified methane at (•) $700^\circ\text{C}$ , (▲) $750^\circ\text{C}$ and (■) $800^\circ\text{C}$ . ....	49
Figure 48: Schematic of microfabricated proton conducting fuel cell. ....	50
Figure 49: XRD pattern of $\text{BaY}_{0.05}\text{Zr}_{0.95}\text{O}_3$ thin film on silicon wafer.....	51
Figure 50: Scanning electron micrographs of $\text{BaY}_{0.05}\text{Zr}_{0.95}\text{O}_3$ thin film on silicon wafer, with patterned features. ....	51
Figure 51: XRD pattern of $\text{La}_{0.67}\text{Sr}_{0.33}\text{MnO}_3$ thin film on silicon wafer.....	51
Figure 52: Control of film porosity by adjusting the viscosity of $\text{La}_x\text{Sr}_{1-x}\text{MnO}_3$ solution through ethylene glycol addition. $\text{La}_x\text{Sr}_{1-x}\text{MnO}_3$ /ethylene glycol weight ratios of (A) 1:0, (B) 1:1, (C) 1:2, and (D) 1:3 were used in the film preparation.....	51
Figure 53: A typical impedance spectrum for a thin film YSZ deposited on a silica substrate. Points are raw data, line is the fit from the equivalent circuit. The main portion of the graph displays the high frequency portion of the spectrum while the inset shows the complete spectrum (note the change in units). The frequency at selected point is given. (Key: I bulk electrolyte; II electrolyte grain boundary; III constriction resistance; IV electrode).....	54

- Figure 54: Arrhenius plot of YSZ grain conductivity, comparing compositions of roughly  $Y_{0.09}Zr_{0.91}O_{2-x}$  ( $\square$ , solid line) and  $Y_{0.16}Zr_{0.84}O_{2-x}$  ( $\square\square$ , dashed line). Points are the values measured for films in this study deposited at 600°C; lines are linear fits to data from literature..... 54
- Figure 55: The low frequency (electrode polarization) conductance normalized by the TPB length for the tape-cast YSZ ( $\blacklozenge$ ), untreated single crystal ( $\bullet, \circ$ ), single crystal with 100 nm of a 600°C-deposited YSZ film ( $\blacksquare, \square$ ), and single crystal with 100 nm of an unheated deposited YSZ film ( $\blacktriangle, \triangle$ ). Closed symbols represent (100)-oriented YSZ single crystal substrates while open symbols represent (111)-oriented single crystal substrates. The lines are extrapolations from literature..... 55
- Figure 56: The electrode activation polarization conductance at 400°C, including the Pt-YSZ composite films. Note, the Pt-YSZ films, being composite mixed ionic conductors, are active across their full area rather than being limited to the triple phase boundary (TPB) length like Pt or LSM. .... 56
- Figure 57: Symmetric thin-film stack of Pt-YSZ, YSZ and Pt-YSZ deposited as a prototype  $\mu$ -SOFC device ..... 57
- Figure 58: (left) YSZ residual stress vs. thickness - trend lines have been shown to clearly distinguish datasets, and (right) planar high-resolution SEM images of sputtered YSZ films of varying thickness. Scale bars are 100nm in length. Images indicate grain growth typically correlated with development of tensile stress in films. .... 58
- Figure 59: Residual stress evolutions with post-deposition thermal cycling: (*left*) behavior for room- and high-temperature deposited YSZ films, and (*right*) behavior of fuel cell stack of Pt-YSZ/YSZ/Pt-YSZ deposited on Si with Ti/SiN adhesion/mask layers. .... 59
- Figure 60: Measured Young's modulus of thin-film YSZ: (*left*) out-of-plane modulus from nanoindentation, and (*right*) in-plane modulus from center height measurement of buckled square membranes. Films are deposited at room temperature..... 60
- Figure 61: Proton conducting thin film residual stress and electrochemical characterization results: (*left*) residual stress vs. temperature for a 200nm thick BaCeYO film, and (*right*) conductivity vs. temperature for BaCeYO and SrCeTbO shown with results from prior work. Prior work is for BaCeYO unless otherwise noted..... 61
- Figure 62: (left) Optical microscope image of buckled YSZ/SiN membrane, and (right) interferometric image of buckled Pt-YSZ/YSZ/Pt-YSZ fuel cell membrane ( $\sim 130\mu\text{m}$  side length). .... 62
- Figure 63: Maximum stresses in a Pt-YSZ/YSZ/Pt-YSZ buckled trilayer stack as a function of square membrane sidelength for  $\Delta T=600^\circ\text{C}$ : (*left*) compressive and (*right*) tensile stress regions. The current analysis does not yet include residual stress. .... 62
- Figure 64: Observed postbuckled and uncracked Pt-YSZ/YSZ/Pt-YSZ samples for nonlinear analysis validation. Unfailed membranes demonstrates fabrication of viable large, ultra-thin fuel cell membranes..... 63
- Figure 65: Fuel cell device structure: (left) illustration of electrolyte-supported 2-sided fuel cell, and (right) cross-sectional SEM of a tri-layer fuel cell stack..... 64

Figure 66: Test reactor for $\mu$ SOFC testing .....	64
Figure 67: Preliminary power test results: 450nm thick Pt-YSZ/YSZ/Pt-YSZ electrolyte-supported fuel cell power curves.....	64
Figure 70: SEM cross-section images of (a) incompletely-filled girder mold, and (b) fully-formed silicon nitride girder in silicon mold. Note the large (3-4 micron, 10 micron deep) gaps resulting from incompletely filled girders.....	66
Figure 71: Cross-section ESEM image of fuel cell stack deposited upon girder support structure. ....	67
Figure 72: Top-Down view of four mask layers comprising the girder-grid supported solid-oxide fuel cell design. ....	67
Figure 73: Pictures of completed prototype girder-grid fuel cell wafer and individual chip. ....	68

### **List of Tables**

Table 1: Ammonia Cracking Summary .....	28
Table 2: Summary of Autothermal Combustion of Fuel/Air.....	29
Table 3: Material properties of potential anode additives to improve coke tolerance of Ni/YSZ cermets .....	47



## 1. Objectives

The MIT MURI program, Microchemical Systems for Fuel Processing and Conversion to Electrical Power, aimed to develop a fundamental understanding of the many different physical phenomena underlying fuel processing at millimeter to micron scale as well as to establish the engineering principles needed to realize portable electrical power generation from hydrocarbon fuels based upon advances in microfabrication, fuel cells, catalysis, materials characterization, and systems engineering. The MURI participants designed, microfabricated, and characterized microchemical systems capable of operating at elevated temperatures and being rapidly cycled between low and high temperatures. This effort entailed the development of novel fabrication strategies based on high temperature materials such as oxides not currently used in standard, mainly silicon-based, microfabrication methods. Systems engineering concepts and tools were developed for understanding and predicting the performance of integrated microchemical systems at steady state and during transients, i.e., startup and shut-down. Fundamental understanding of transport and reaction processes in microchemical systems were explored and incorporated into the engineering design principles and simulation tools for microreactor systems. A critical component was the development of fundamental understanding and engineering approaches to integration of materials with different thermophysical properties into systems undergoing large spatial and temporal temperature variations. The effort also involved a significant materials and synthesis effort, specifically the synthesis and characterization of novel solid oxide fuel cell materials as well as nanostructured tailored heterogeneous catalytic surfaces for microchemical systems.

## 2 Executive Summary

The multidisciplinary MIT MURI team has created broad understanding of fundamental physical processes underlying microchemical systems for fuel conversion and made specific advances in microfabrication of microsystems, fuel cells, catalysis, materials characterization, and systems engineering.

Systems engineering has been used to compare different alternatives and identifying a subset of all possible processes that are the most promising in terms of one or more given objectives. A methodology was developed based on decomposition into three levels of modeling detail: system-level models for process synthesis, intermediate fidelity models for optimization of sizes and operation, and detailed computational fluid dynamics models for geometric design. The system-level considered a variety of fuels including hydrogen, ammonia, various hydrocarbons and alcohols, and fuel cell types including solid oxide fuel cell (SOFC), polymer electrolyte membrane (PEM), single chamber solid oxide fuel cell, direct methanol fuel cell (DMFC) and proton conducting fuel cell based on ceramic technology (PCFC). Use of simulation and parametric mixed-integer optimization selected the most promising process structures along with idealized layouts among thousands of alternatives. The intermediate modeling effort included simple yet sufficiently physically realistic models to predict system performance. For example, these techniques enabled studies of start-up strategies for combined fuel cell battery systems and investigations of varying power demand. Detailed computational fluid dynamic models (CFD) have generated insight into the optimal component design, as well as a verification of the system-

level models. Many of the formulations employed for the optimal design and operation required advanced mathematical tools. Significant contributions were made in the fields of parametric mixed-integer optimization, optimization with embedded hybrid dynamic and differential-algebraic systems, as well as bilevel optimization. These tools apply to fields as well.

Suspended-tube reactor/heat exchangers were developed as a means to thermally isolate the chemical reaction zone in a fuel processor utilizing a portion of the fuel to generate heat for reforming the remaining fuel into hydrogen. The designs overcome the critical thermal management difficulties of small-scale fuel processors through the integration of thermally-insulating and thermally-conductive materials in a defined, microfabricated tube/slab structure. The suspended-tube reactor can also be used as a thermally-efficient combustor/recuperator in other power generation systems, such as in thermoelectric or thermophotovoltaic generators. The suspended-tube fuel processor is designed to generate hydrogen in a high-temperature reaction zone. Within this zone, two distinct reactions take place. In one section, a fuel is combusted over a catalyst to generate heat. This heat allows the entire reaction zone to be maintained at an elevated temperature with no electrical power input at steady-state. In addition, this energy is used by an endothermic process occurring in the second channel, in which a fuel (not necessarily the same fuel used for the combustion) reacts over a catalyst to form hydrogen and other side products.

In the evaluation of the fuel processing approaches, two reaction systems were considered: (1) catalytic combustion (various fuels), and (2) catalytic ammonia cracking. Simultaneous butane combustion and ammonia cracking were carried out in the suspended-tube reactor over Pt/Al<sub>2</sub>O<sub>3</sub> catalyst particles. During the autothermal portion of this experiment, net hydrogen production was achieved from the reactor with no electrical power input. Hydrogen combustion occurred to full conversion (> 99%) throughout a broad range of flow rates and when combined with ammonia cracking, significant production rates of hydrogen were achieved. Several microchemical systems have been developed to optimize performance and simplify microfabrication strategies. Substantial effort has been expended on the chip level vacuum packaging process, which is critical to the performance of the reactor. Several different microfabrication strategies for thermally efficient microreactors were considered to enhance reliability, reduce microfabrication cost, and establish design rules for thermally efficient fuel processors. CFD simulations as well as intermediate fidelity models were sufficient accurate and fast to enable design calculations and predict process performance.

Palladium-based micromembranes have been fabricated and demonstrated for hydrogen purification. These devices were capable of achieving hydrogen fluxes ranging from 4-40 mol/m<sup>2</sup>/s with hydrogen-to-helium selectivity in excess of 1000:1 under ideal conditions. Additionally, devices were able to maintain competitive hydrogen fluxes and selectivity in the presence of ammonia and carbon monoxide contaminants. These micromembrane systems have been extended to generation of high-purity hydrogen by incorporation of catalysts, specifically LaNi<sub>0.95</sub>Co<sub>0.05</sub>O<sub>3</sub> perovskite catalysts. With methanol fuel, a hydrogen selectivity of 47.0% was obtained at an oxygen-to-fuel ratio of 0.35:1 and temperature of 475°C, at an overall hydrogen yield of 92.1% and methanol conversion of 63%. Yields can be improved with pressurization of the feed gas, and methanol conversions can be increased by packing the feed channel with additional catalyst. An autothermal high-purity hydrogen generator, employing the above catalytic micromembrane technology, has been designed. The additional energy required for

autothermal operating is provided by combustion of rejected fuel, carbon monoxide and hydrogen in a separate chamber downstream of the membrane reactor.

The MURI effort has been addressing the challenges of microfabrication of solid oxide fuel cells (SOFCs) to exploit the many potential advantages of such structures. Thin film anodes and cathodes enhance ionic conductance in mixed ionic-electronic conducting electrodes. Reduced temperature thin film processing often leads to nano-scale microstructures reported to exhibit improved or distinctive catalytic activity and transport properties. The specific effects of nano-scale grain sizes and grain-boundary engineering are not well known and so their study has provided opportunities to not only improve performance characteristics, but also to obtain a more fundamental understanding of ionic conductivity in oxide materials. Lower processing and operating temperatures enabled the use of advantageous materials or structures that would be unstable at normal SOFC operating conditions. The use of microelectrodes, with well defined areas and triple phase boundary lengths, has allowed for a clear distinction to be made between electrodes for which all reactions are localized to the triple phase boundary and for those for which the full electrode area is active. Materials investigated include YSZ and CGO solid electrolytes and Pt and LSCO electrodes. Platinum electrodes with well controlled geometry were sputtered onto the surface of bulk YSZ and onto sputtered YSZ thin films. Films exhibiting nanometer grain sizes had a specific grain boundary conductivity enhanced by a factor of 30-100 compared to the bulk polycrystalline sample. Photolithography alone was unable to give technologically useful triple phase boundary lengths. In order to achieve the triple phase boundary lengths needed for a practical device, reactive co-sputtering was used to produce composite Pt-YSZ thin films with a bi-continuous network morphology and grain sizes on the order of 30 nm. Such intimate mixing of the electronic and ionic conducting phases created an effective mixed ionic-electronic conductor with the entire surface of the film electrochemically active to the electrode reaction. The best processing conditions resulted in electrodes with an area specific polarization resistance less than  $500 \Omega \cdot \text{cm}^2$  at  $400^\circ\text{C}$  and, by extrapolation,  $1 \Omega \cdot \text{cm}^2$  at  $608^\circ\text{C}$ . These films could enable operation of a micro-solid oxide fuel cell at intermediate temperatures ( $400\text{-}500^\circ\text{C}$ ).

Engineering of reliable, high temperature microchemical systems for energy conversion necessarily requires a through understanding of reactions at solid interfaces as well as stresses created by differences in thermal expansion coefficients. The MIT MURI has built structures for the testing and characterization of stresses induced in the electrolyte/electrode supported structures during processing as well as during heating-cooling cycles. In the design and fabrication of the microfabricated structures, alternate designs have been evaluated based on single and double chamber cells as well as process compatibility. New findings with significant impact to the design of the fuel cell stack include moving to a high-temperature co-sputtered deposition process which is needed for operation of the anode/cathode composite electrodes, identification of a stress generation (and relaxation) mechanism, a revised thermomechanical structural analysis scheme allowing for an expanded design space, and preliminary structural (fuel cell stack trilayer) testing to use in the validation of this analysis. Taken together, these findings have allowed the design, fabrication, and thermal cycling to operating temperature ( $600^\circ\text{C}$ ) of thermomechanically viable square fuel cell trilayer membranes of  $\sim 125 \mu\text{m}$  sidelength. The thermomechanical effort has also provided essential understanding to the successful realization of microfuel combustors and reformers as well as the hydrogen purification systems.

Finally, considerable efforts have been devoted to developing and characterizing novel nanostructured catalytic materials. A novel perovskite catalyst,  $\text{LaNiO}_3$ , was developed and synthesized for oxidative steam reforming of methanol. Under dilute fuel conditions, this nanostructured perovskite catalyst exhibited higher conversions than  $\text{Pd/Al}_2\text{O}_3$  above  $250^\circ\text{C}$  in a packed-bed reactor. In addition,  $\text{LaNiO}_3$  provided superior hydrogen selectivity compared to the noble metal catalyst. It was noteworthy that for the same weight loading, the catalyst bed for nanostructured  $\text{LaNiO}_3$  took up only 2/5 the bed volume of the noble metal system. Steam reforming of light hydrocarbons is one of the most important industrial processes for hydrogen production. Propane steam reforming was examined in this research since propane was an attractive fuel for portable hydrogen production. In this study, nanocrystalline nickel aluminates with various Ni/Al ratios were prepared by chemical co-precipitation. Addition of 2 wt% Re and 2 wt% V were found to improve both the catalytic activity and coking resistance.

The MIT MURI has involved 7 faculty, 20 graduate students, 10 postdoctoral fellows, and 6 undergraduates. Of the PhD student and Postdocs eight have gone onto academic positions. The program has so far produced 7 PhD thesis, 40 papers in peer reviewed journals, 20 papers in conference proceedings (some of which are very competitive in abstract selection), 2 papers are currently under review and another 12 with the latest MURI results are in final stages of preparation. The principal investigators have given 58 invited talks, and the program has contributed 50 talks, at major conferences. Additional details are given in Section 11.

## **2.1 Recommendations:**

Realization of microreactor based portable energy conversion system has to involve thermally efficient, integrated reformer and fuel cell systems. SOFC technology will have better energy efficiency than PEM systems, but also require significant advances in materials and sealing technology. In general, realization of high energy efficient ( $>30\%$ ) reforming based systems will demand significant new understanding of thermal management solutions, thermophysical properties of mixed materials systems, and integration techniques for power systems. These results would represent significant scientific and engineering contributions and would have broad technological impact.

Specific areas of research needs are:

- New understanding, systems engineering, and materials expertise to create integrated, high efficiency fuel reformer – fuel cell systems.
- Understanding of design rules and materials properties allowing the design of highly integrated and thermally efficient systems.
- Advances in fundamental electrocatalysis resulting in moderate temperature direct conversion hydrocarbon based fuel cells.
- Fundamental advances in catalysis and interfacial science enabling the realization of new chemical to electric energy schemes

### 3 MURI Team Structure

In order to address the many different aspects of microfabricated fuel processing systems, we assembled a multidisciplinary research team that combined the necessary expertise, specifically in the areas of thermomechanical properties of materials, materials synthesis, microfabrication, chemical reaction engineering, heat transfer, catalysis, simulations, and systems engineering. This multidisciplinary research program has set the following goals for the proposed effort:

- Systems engineering concepts and tools for understanding and predicting the performance of integrated microchemical systems at steady state and during transients, i.e., dynamic behavior. *Task Leader: Barton*
- Fundamental understanding of transport and reaction processes in microchemical systems. Development of engineering design principles and simulation tools for microreactor systems. *Task Leaders: Barton and Jensen*
- Development of design and microfabrication strategies for microchemical systems capable of operating at elevated temperatures and being rapidly cycled between low and high temperatures. This will entail the development of novel fabrication strategies involving high temperature materials such as oxides not currently used in standard, mainly silicon-based, microfabrication methods. *Task Leaders: Jensen and Schmidt*
- Synthesis and characterization of novel catalytic materials for low temperature partial oxidation and reforming as well as for novel SOFC electrodes. In particular, tailored heterogeneous catalytic surfaces for microchemical systems will be generated by forming nanostructured features on surfaces of micron-scale flow channels. *Task Leaders: Tuller and Ying*
- Fundamental understanding and engineering approaches to integration of materials with different thermophysical properties into systems undergoing large spatial and temporal temperature variations. *Task Leader: Wardle*

The organization of the multidisciplinary research thrusts needed to realize these goals is illustrated in Figure 1. Responsibilities of particular thrust areas were assigned to individual PIs in the MURI on the basis of expertise to ensure the research moves forward. As seen from the figure, the different tasks were highly interconnected. All the members of the MURI met at least every other week and smaller teams meet more frequently. These teams were made up by faculty, postdoctoral associates, and students to address particular research issues. The overlap and interactions among task areas grew as the program progressed and the team functioned as one cohesive unit at the end of the program.

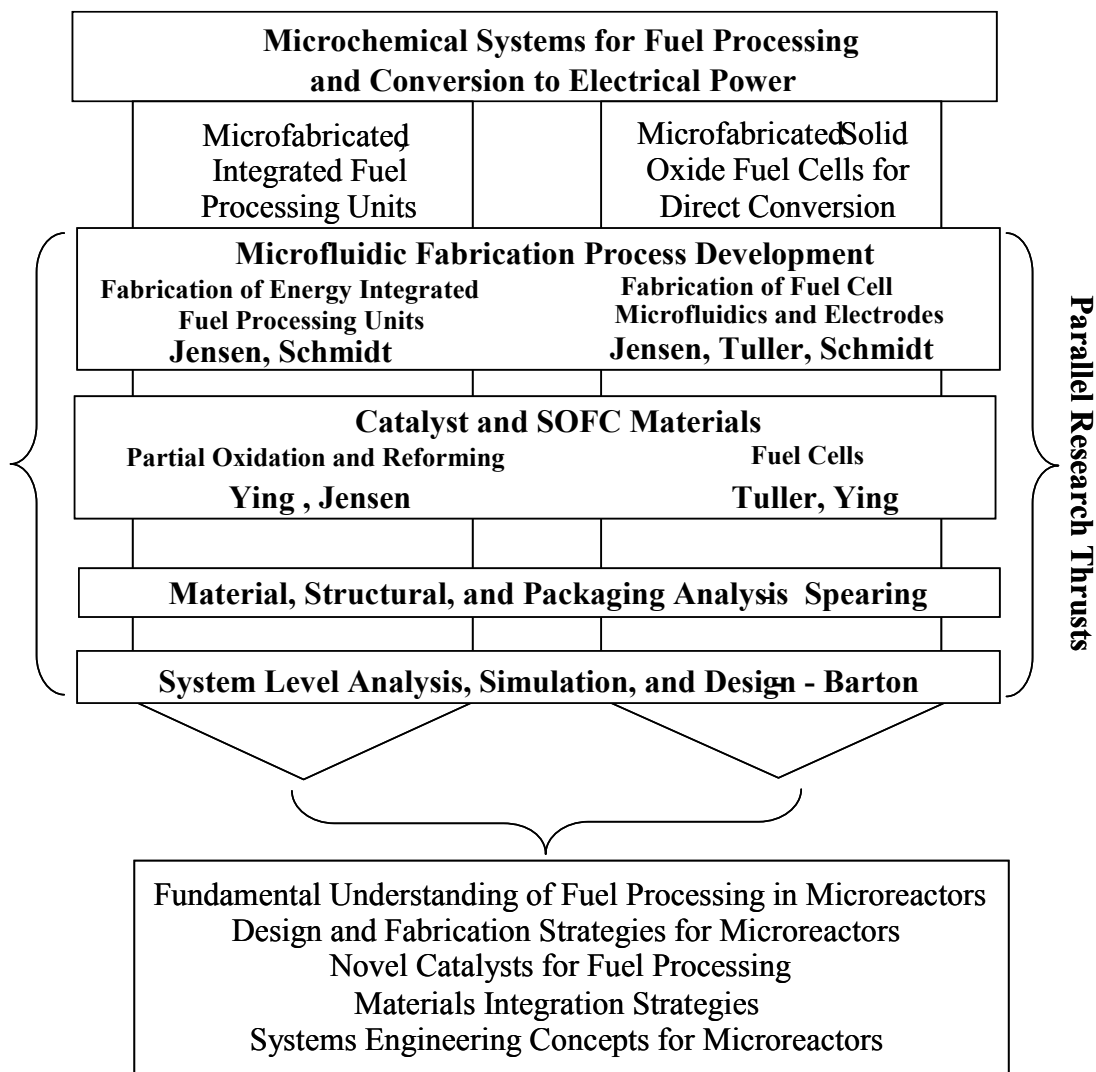


Figure 1: Overview of research thrust areas.

## 4 Major Accomplishments

The major accomplishments during the reporting period are summarized below. Additional details are given in the subsequent sections.

- Formulated a methodology for the optimal design and operation of microfabricated fuel cell systems based on decomposition into three levels of modeling detail and interdisciplinary interactions
- Developed system-level models for comparison of alternatives, including fuel combinations, heat integration and layout
- Developed intermediate fidelity models that allow design and operation (steady-state and transient) of fixed process structures

- Developed detailed models that allow geometry improvement as well as the derivation of modeling assumptions
- Developed numerical techniques necessary for the design problems considered
- Developed thermally efficient suspended-tube reactor/heat exchanger that addresses thermal management issues at small scales.
- Performed heat transfer analysis to form a complete description of the heat transfer in the suspended-tube reactor/heat exchanger including the effect of
- Developed methods for washcoating gel and slurry catalysts and for localizing these catalysts using fluidic stop valves.
- Demonstrated self-sustained (autothermal) catalytic combustion of hydrogen, ammonia, propane, and butane in air.
- Demonstrated controlled self-sustained combustion of hydrogen with simultaneous ammonia cracking to hydrogen at temperatures up to 900°C.
- Demonstrated net production of hydrogen through ammonia combustion and cracking in low-vacuum ambient at ~600°C
- Newly designed KOH etching based micro fuel processor cheap and quick to fabricate, with yields exceeding 95%.
- Glass brazing technique provides a leak-proof seal between borosilicate and silicon and is stable to 750°C.
- Autothermal, steady combustion of hydrogen and propane demonstrated with new device.
- Generation and purification of hydrogen from methanol partial oxidation in palladium membrane microreactor to produce CO-free hydrogen stream for PEM fuel cells.
- Autothermal methanol reformer combining hydrogen purification and combustion of residual methanol, CO, and H<sub>2</sub>.
- Optimized conditions and for bonding in vacuum with glass frit resulting in stable hermetic seal.
- Examined LaNiO<sub>3</sub> partial oxidation catalysts under full-fuel conditions at high space velocity.
- Developed Ni-Sn/Y<sub>2</sub>O<sub>3</sub>-stabilized ZrO<sub>2</sub> (Ni-Sn/YSZ) for the dry reforming of methane.
- Synthesized nickel aluminate catalysts for the steam reforming of propane.
- Demonstrated the effective promoters for improving the low-temperature catalytic activity and coking resistance of nickel aluminate catalysts.
- Produced lithographically defined model electrode/electrolyte structures for modeling fundamental fuel cell kinetics
- Designed system capable of in-situ examination of thin film electrochemical cells at elevated temperatures and controlled atmospheres

- Discovered ability to markedly enhance Pt electrode performance (by as much as a factor of 300) via low temperature (Si-free) processing
- Extended triple phase boundary length in Pt 10,000 fold via novel thin film processing routes. Predict power approaching  $1\text{W}/\text{cm}^2$  at  $400^\circ\text{C}$
- Developed nanostructured Pt-YSZ cermet with superior performance. Basis of symmetric micro-SOFC stack.
- Thin film YSZ was found to exhibit an increased conductivity over bulk YSZ, by as much as a factor of 20-30.
- Engineered controlled levels of mixed ionic-electronic conductivity in a model cathode material; Pr-Ce oxide.
- Modeled influence of geometrical factors on electrochemical performance
- Identified controlling mechanisms and quantified “tunability” of residual stresses in ultra-thin film YSZ electrolyte through primary deposition variables of working pressure and substrate temperature
- Measured mechanical properties of ultra-thin film YSZ electrolyte in conjunction with microstructural studies
- Created two proton conducting oxides in ultra thin-film form and measured their electrochemical and residual stress properties for low-temperature operation fuel cells
- Demonstrated expansion of fuel cell design space through experiments and non-linear post-buckling analysis to yield large, free-standing fuel cell membranes
- Experimentally verified operation of electrolyte-supported ultra-thin (450 nm) fuel cell devices by designing microfabrication routes using nonlinear design tools

## 5 Systems Engineering

With current computational possibilities and available algorithms it is impossible to solve for the optimal design and operation in one step because the devices considered involve complex geometries, multiple scales, time-dependence and parametric uncertainty. Therefore, a methodology is developed based on decomposition into three levels of modeling detail, namely system-level models for process synthesis, intermediate fidelity models for optimization of sizes and operation, and detailed computational fluid dynamics models for geometric design, see also Figure 2.



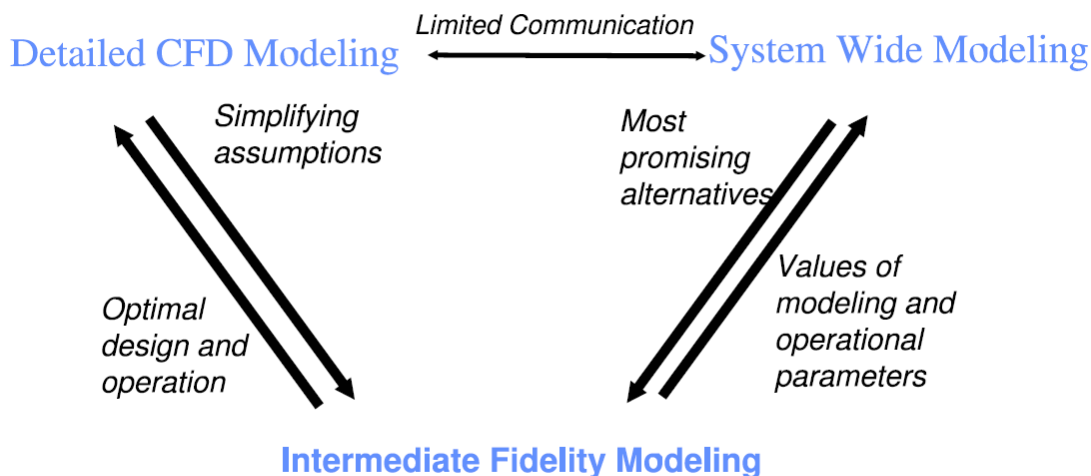


Figure 2: Methodology overview

The coupling between the three levels is done by engineering judgment. The chosen decomposition allows interactions within the MURI group, see also Figure 3. At the system-level the set of alternatives considered is based on fabrication limits, and system-level considerations are used to determine on which processes the fabrication effort should focus. Catalysis and reaction engineering efforts provide lumped reactions used in the system-level models, while sensitivity considerations at the system-level suggest the reactions on which catalysis effort should focus. For detailed modeling an initial geometry is provided by reactor engineering efforts, and computational fluid dynamic analysis suggest improvements on this geometry. At the intermediate fidelity level, kinetic models and limits of operating conditions are required and provided by reaction engineering and material characterization efforts. On the other hand, intermediate fidelity models provide optimal sizing of components and operating conditions.

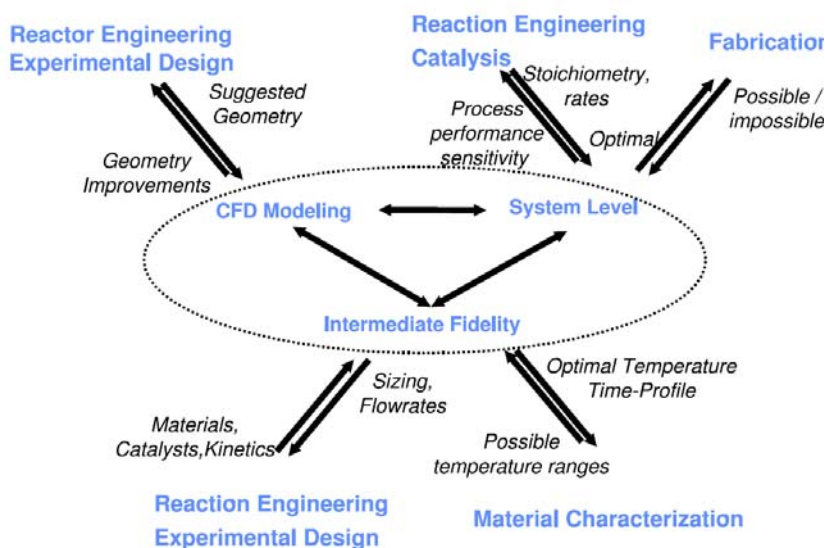


Figure 3: Examples of interactions of methodology with rest of MURI effort

## 5.1 System Level Modeling

At the system-level a variety of fuels including hydrogen, ammonia, various hydrocarbons and alcohols, and fuel cell types including solid oxide fuel cell (SOFC), polymer electrolyte membrane (PEM), single chamber solid oxide fuel cell, direct methanol fuel cell (DMFC) and proton conducting fuel cell based on ceramic technology (PCFC) are considered. As Figure 4 shows there are hundreds of alternative combinations, including heat integration and gas purification. Through the use of simulation and parametric mixed-integer optimization the most promising process structures along with idealized layouts are selected among thousands of alternatives. To facilitate use of the models a web interface is at <http://yoric.mit.edu/micropower.html> to registered users.

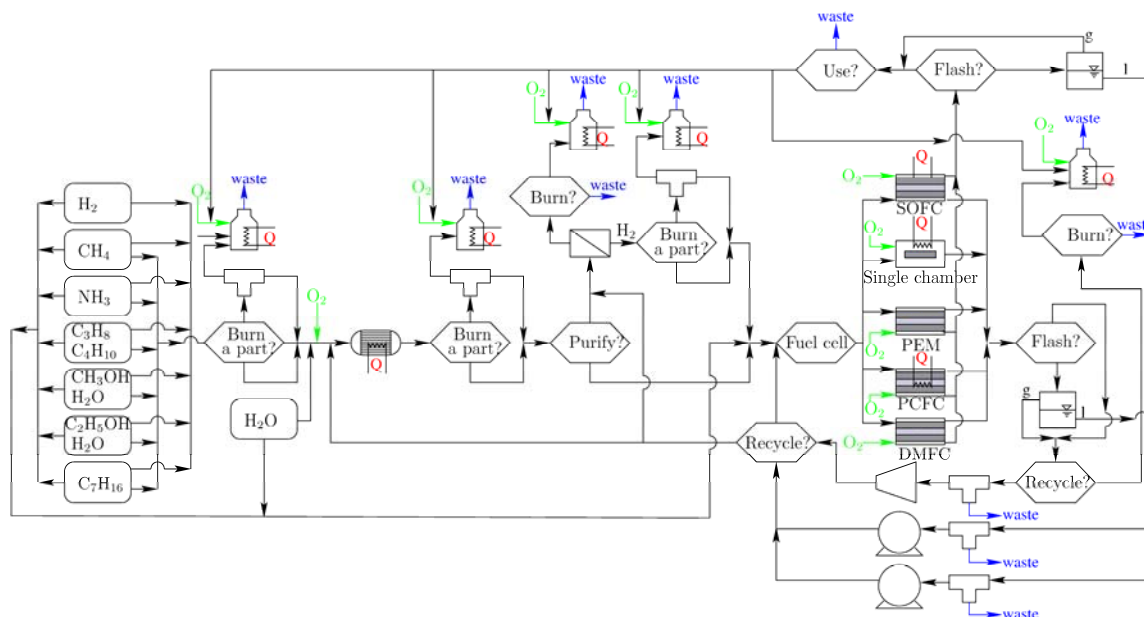


Figure 4: Conceptual illustration of considered processes

The two major scales of portable power generation are the power output and the mission duration. Figure 5 shows the achievable energy densities in Wh/(l system) for a process based on butane partial oxidation and an SOFC as a function of the power output for different values of mission duration. For low power outputs the heat losses dominate over the exothermicity and the achievable energy density increases with the power output. For higher power output the heat generation is sufficient and the process performance does not depend on scale. The energy density increases with duration and approaches the energy density with respect to the fuel volume.

It is also very interesting to note that depending on the scale a different process configuration may be optimal. PEM-based processes may for example achieve a higher energy density for low power outputs and duration, but will be outperformed by SOFC-based processes for higher power outputs and mission durations. This clearly motivates the use of advanced design tools such as parametric optimization to address the optimal product design.

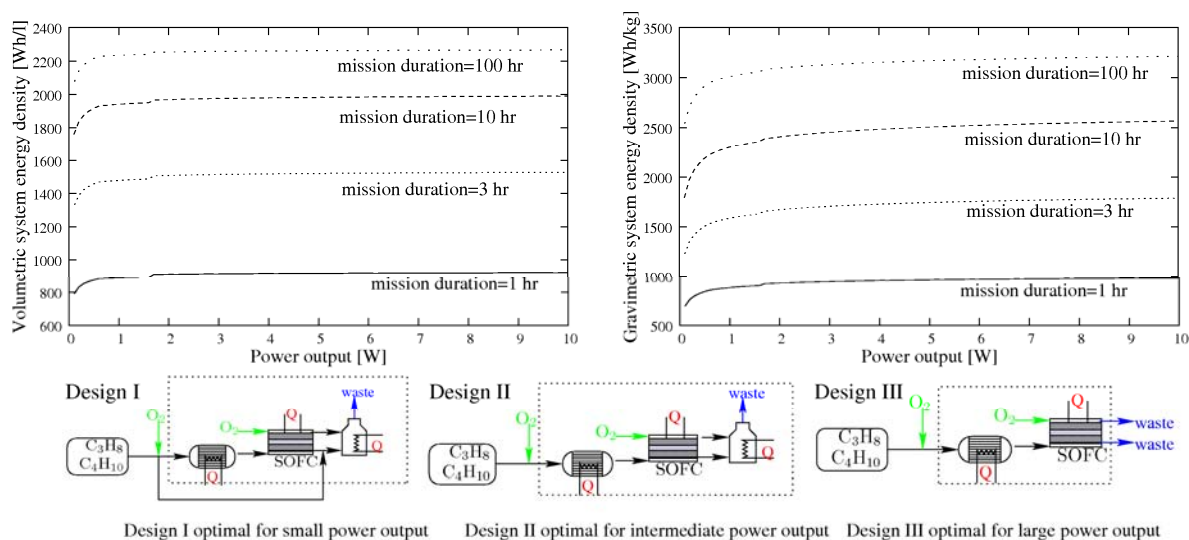
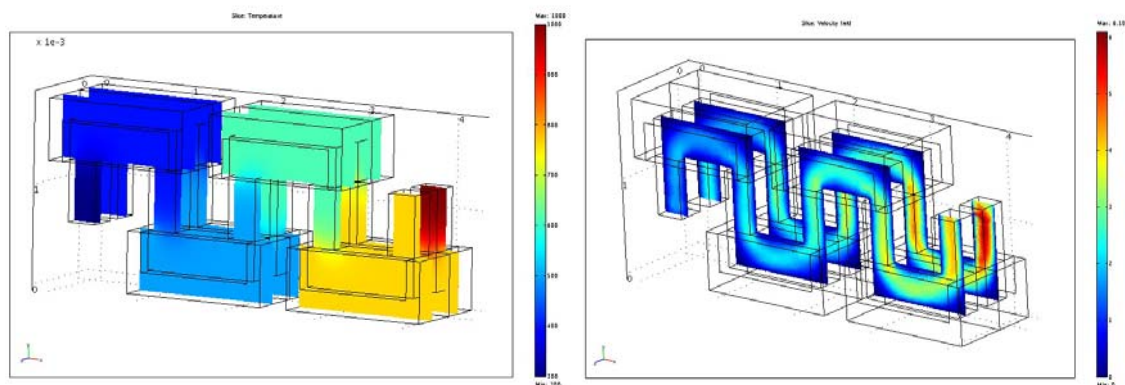


Figure 5: Effect of scale on process performance

## 5.2 Computational Fluid Dynamics Analysis of Fuel Cells

In collaboration with the micro-reaction fabrication effort, two- and three-dimensional computational fluid dynamics models of the suspended micro-tube reactors are created (see also Section 6.5.1). The silicon structures in the reactors allow for a very fast heat transfer. Without these structures a significant temperature difference between the exothermic and endothermic reactions is observed, while with the silicon structures the temperature in the reactor is essentially uniform. Similarly, due to the high thermal conductivity of silicon, the silicon slabs in the third generation suspended micro tube reactor are of essentially uniform temperature. This is shown in Figure 6 and allows the development of an equation-oriented model as well as a simplified analysis of geometrical considerations, e.g., the influence of number of slabs.

Figure 6: Temperature (left) and velocity distribution (right) in the vertical heat exchanger of  $S_{\mu}REIII$  (see Section 6.6.1) reactor

### 5.3 Intermediate Fidelity Models

As a case study for the optimization of a fixed process structures an ammonia cracking based process, using butane catalytic combustion for heat generation was used. The conceptual flowsheet is shown in Figure 7.

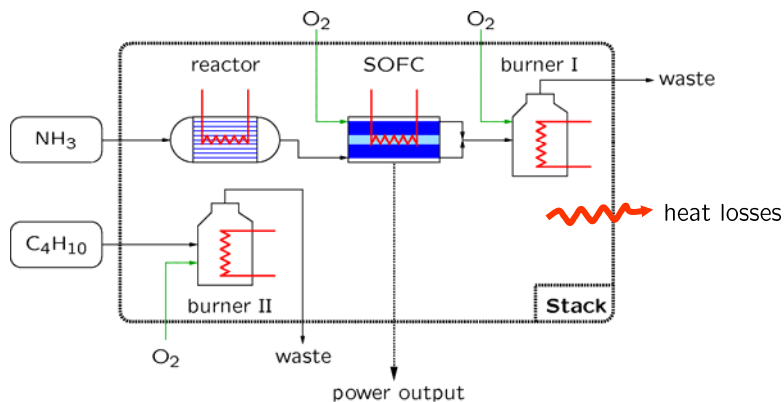


Figure 7: Conceptual process flowsheet for the intermediate fidelity modeling case-study.

For optimal steady-state operation, a counterintuitive result was obtained, which shows that the heat losses decrease with increasing temperature, due to the decreasing volume requirements. Maximal energy densities are obtained for very high temperatures and material constraints need to be considered. This is illustrated in Figure 8 that shows the optimal sizing for the process and the heat losses as a function of the operating temperature.

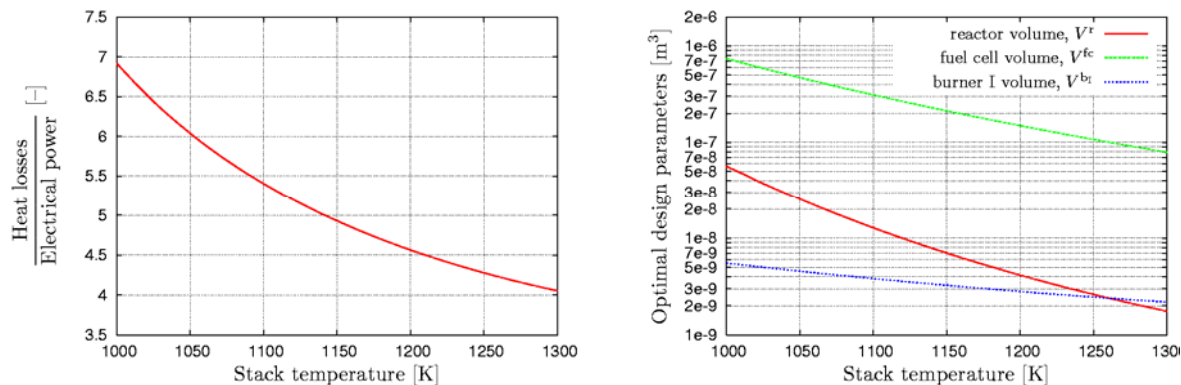


Figure 8: Ratio between heat losses and electrical power (left plot) and optimal design parameters (right plot) vs. operating temperature, for a nominal power output of 1W.

For start-up an auxiliary power source, such as a battery, is needed to provide power until the fuel cell stack is at a sufficiently high temperature. Figure 9 shows the optimal power profile when the auxiliary battery is used also as a heat source to heat the stack. Most portable electric and electronic devices are not operated with a constant load over time, but rather follow a power profile. In many cases this profile can be approximated by a small number of discrete power levels. For instance, dismantled soldiers consume most of the time only 20W, while their peak power is approximately 50W. An optimal design and operation formulation which incorporates the varying power demand was developed based on stochastic programming. It was demonstrated that including the variability is essential even at the design phase.

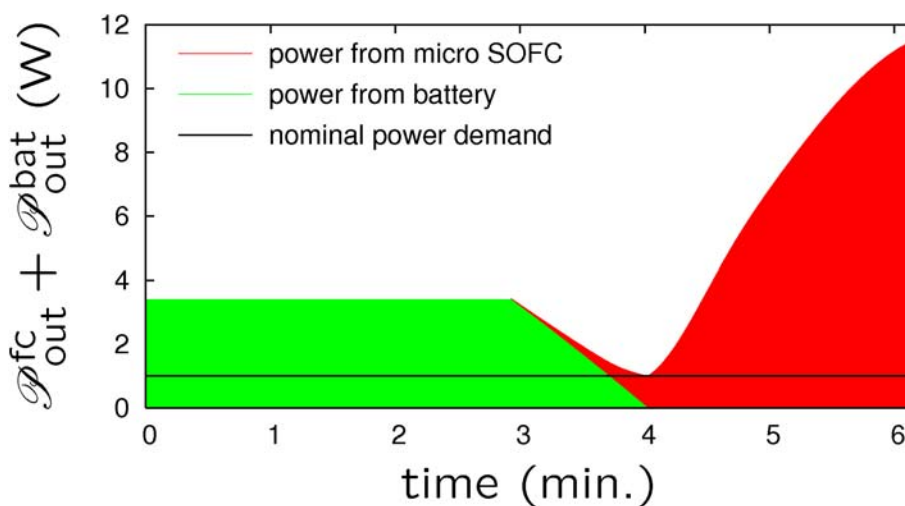


Figure 9: Optimal power profiles at startup for a nominal power output of 1W.

#### 5.4 Fundamental techniques

Many of the formulations employed for the optimal design and operation require advanced mathematical tools. In some cases the algorithms available in the literature cannot be used and therefore new techniques were developed. Significant contributions were made in the fields of parametric mixed-integer optimization, optimization with embedded hybrid dynamic and differential-algebraic systems, as well as bilevel optimization. These tools are used for the methodology developed but can be also applied to different fields.

## 6 Microfabricated Fuel Processors

We have designed and fabricated a MEMS suspended-tube reactor/heat exchanger designed to thermally isolate the chemical reaction zone in a power generation system. It overcomes the thermal management difficulties of small-scale fuel processors through the integration of thermally-insulating and thermally-conductive materials in a carefully defined, microfabricated tube/slab structure.

The suspended-tube reactor (Figure 10) is designed to simultaneously carry out two reactions that exchange heat: a combustion reaction to generate the heat, and an endothermic reaction to produce hydrogen. A variation of this reactor is also designed for thermophotovoltaic power generation (discussed in subsequent section). The main components are four thin-walled (2- $\mu\text{m}$  wall thickness), U-shaped, 3-mm long tubes made of low-stress silicon nitride. The reactions take place in adjacent channels at the suspended end of the silicon nitride tubes, within a thermally-conductive silicon reaction zone. Heat exchange in this zone is facilitated by the intimate thermal contact between the channels, and by the silicon that encases the tubes in this region. The suspended silicon nitride tubes contain slabs of silicon positioned along the length of the tubes to exchange heat between process streams and recover process energy from the exhaust gases. For hydrogen production through endothermic reactions (e.g., ammonia cracking, hydrocarbon steam reforming), combustion of a fuel in one stream provides the energy required

for the endothermic reaction in the adjacent stream (Figure 11), and both streams are kept in intimate thermal contact. For exothermic hydrogen production (e.g., partial oxidation of hydrocarbons), both channels can be used to process the reactant mixture, and the structure serves as a thermally-isolated reactor/preheater. The suspended-tube reactor can also be used as a thermally-efficient combustor/recuperator in other power generation systems, such as in thermoelectric (TE) or thermophotovoltaic (TPV) generators (see Section 6.4).

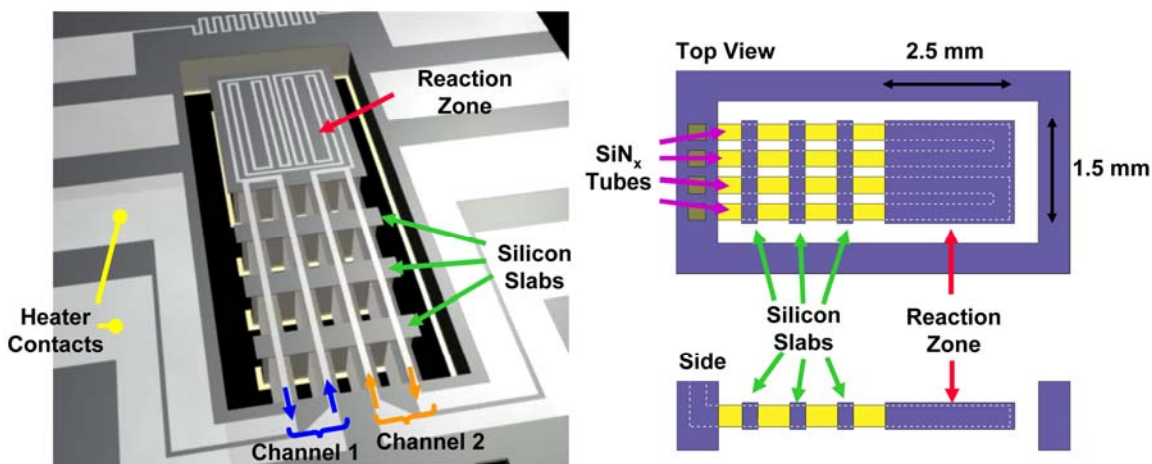


Figure 10: Schematic of the suspended-tube reactor. In the fabricated device, each tube is 200  $\mu\text{m}$  wide by  $\sim 480$   $\mu\text{m}$  high. While a three-slab configuration is shown in this figure, the number of slabs can be varied. The silicon slabs wrap completely around each.

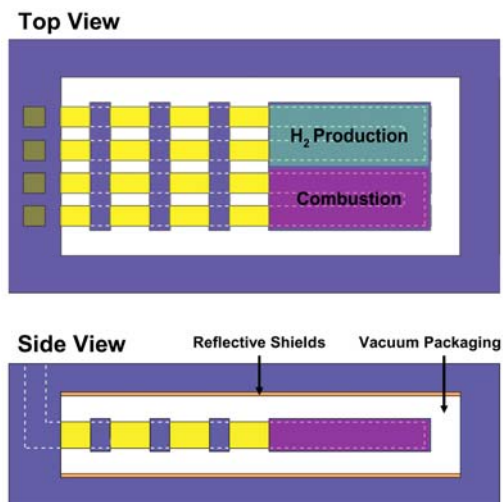


Figure 11: Illustration of how the suspended-tube reactor is used for simultaneous combustion and hydrogen production. The combustion heats up the entire silicon reaction zone at the end of the tubes so that endothermic hydrogen production may take place. Vacuum packaging and reflective shields, required to maximize the thermal isolation of the reaction zone, have been tested independently, but have yet to be integrated into the device.



## 6.1 Overall Heat Loss and Energy Balance

The experimental steady-state heat loss analyses (in the absence of flow) and the numerical heat recuperation analysis provide a thorough description of the overall heat losses in the suspended-tube reactor. This detailed understanding of the heat losses is required in order to make meaningful predictions of reactor performance, whether the reactor is used for hydrogen production or as a combustor (for TE or TPV). The heat losses affect the overall efficiency and influence the steady-state reactor temperature for autothermal (self-sustained) combustion.

The overall heat loss can be used in an energy balance analysis in order to make predictions of reactor performance. With combustion occurring in the silicon reaction zone, the energy generated by the combustion reaction at steady-state will equal the heat loss from the reactor. If an endothermic reaction is occurring in the second channel in the reaction zone, then some of the combustion energy will also be “consumed” by this reaction (as the products are transferred to a higher thermodynamic energy state than the reactants). Two situations will be considered: (1) combustion in one channel (where another reaction would be taking place in an adjacent channel to produce hydrogen) and (2) combustion in both channels (e.g. for TE and TPV generation).

For the heat balance analysis, it will be assumed that the fuel combusts to completion, i.e. (conversion is 100%), and that this combustion is the only source for heat generation in the reactor. The ratio of heat generated to heat lost is maximized when all of the fuel fed to the reactor is converted. Therefore, the results obtained from the heat balance where full conversion is assumed will represent the best possible scenario for thermal management in the reactor. In reality, the fuel conversion may be below 100% for the combustion reactions due to finite reaction rates within the relatively small reactor volume (and small catalyst mass). Accurate predictions for the reaction rates require detailed modeling of the kinetics, heat, and mass transfer within the reactor.

For hydrogen production, combustion in one channel drives an endothermic reaction in the other channel. In this case, all of the energy released by combustion of the fuel is either lost to the environment or consumed by the endothermic reaction. The heat losses from a reactor at 800°C are significant Figure 12a; in fact, for the range of flow rates considered in this analysis, the fuels other than hydrogen cannot be burned autothermally for a reactor packaged in air. This means that reaction zone must be able to completely combust more than  $10^{-6}$  kg of a stoichiometric fuel/air mixture per second (thereby generating well over 2.5 W of thermal power) in order to reach a steady state. Hydrogen, however, can be burned autothermally in a reactor packaged at atmospheric pressure with substantially lower flow rates and heat loss. A reactor packaged in vacuum has substantially lower fuel requirements. The suspended-tube reactor may also potentially be used as a combustor for other forms of portable electric power generation (including TE and TPV). In this case, both channels of the suspended-tube reactor would be used for combustion. Figure 12b shows the predicted heat loss and heat generation for a reactor at 800°C in which combustion proceeds at full conversion in both channels. In this case, the heat balance closes for all of the fuels within the range of flow rates considered. The total flow rate of fuel and air in both channels when combustion occurs in both channels is substantially lower than that required for a reactor at 800°C in which combustion occurs only in one channel.

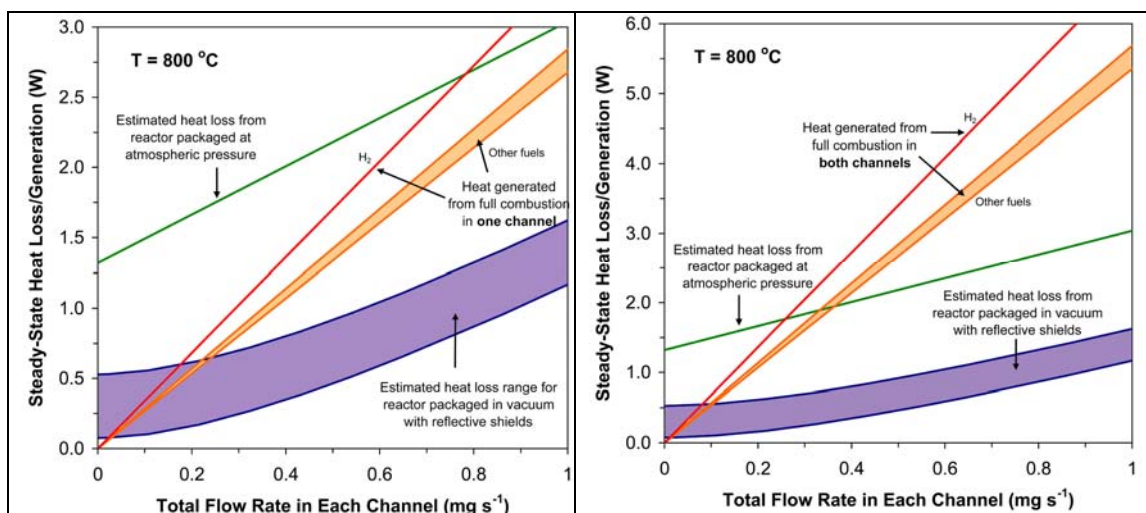


Figure 12: Predicted steady-state heat loss and heat generation for a reactor at 800°C as a function of flow rate within each tube. (a) Combustion in single tube and (b) combustion in both tubes. The generation lines correspond to full conversion of a stoichiometric fuel/air mixture at the given flow rate in one channel. The “other fuels” includes butane, propane, methanol, and ammonia.

## 6.2 Catalyst Preparation and Localization Using Fluidic Stop Valve

Fuel processing for hydrogen production requires elevated temperatures. Some of the processes, including combustion, can in theory be carried out homogeneously, i.e. without a catalyst. However, for all types of reactions, a catalyst can reduce the temperature requirements for the reactions significantly, and thereby reduce the heat losses from the system. For this reason, fuel processing systems, particularly those used for portable power generation, extensively employ heterogeneous catalysts.

Various types of catalysts can be used within microchannels, including particles or pellets, catalysts directly impregnated into the microchannel walls, or washcoats of supported catalysts. Regardless of what type of catalyst is used, localization of the catalyst is an important component of the catalyst preparation. The suspended-tube reactor can not be disassembled in order to load the catalyst directly in a particular region of the reactor. In the suspended-tube reactor, passive fluidic stop valves have been integrated for localization of catalysts prepared by washcoating techniques.

Figure 13 outlines the general procedure for using a stop valve to control the location of the catalyst, and thereby control the location of the catalytic combustion. Prior to loading of the catalyst, the surfaces may need to be treated to modify the wetting properties of the washcoat solution on the surface. The liquid catalyst solution is first allowed to wick in via the outlet tube of the combustion channel. So long as the liquid wets the solid (contact angle below 90°) and no sudden enlargements are present along the way to the stop valve, the liquid will wick into the channel and reaction zone without the need for applied pressure. When the liquid reaches the sudden enlargement at the stop valve, the liquid will no longer continue to flow into the channel. If the stop valve is placed at the reaction zone inlet, it may prevent the washcoat solution from entering the inlet tube. Once the catalyst is dried, catalyst will only be present within the reaction zone and outlet tube, but not in the inlet tube. The catalyst at this point can be calcined and/or reduced *in situ*. To carry out the reactions, the combustion gases (fuel/air mixture) are



then introduced through tube that does not contain catalyst and therefore will not ignite prior to reaching the reaction zone.

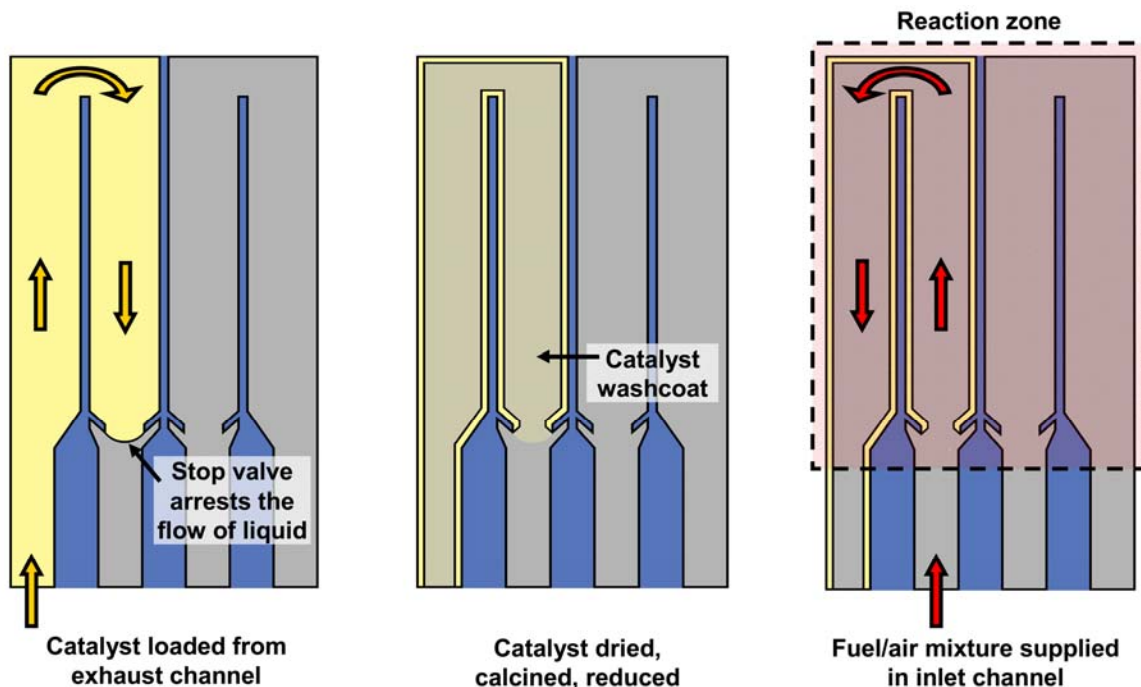


Figure 13: Procedure for introducing catalyst washcoats such that catalyst is not deposited in the inlet tube.

Through an energy minimization analysis, it is possible to estimate the stop pressure (pressure opposing the continued flow of the liquid) that develops at the fluidic stop valve. For a positive stop pressure, the fluid will reach the stop valve and cease to flow. The sign and magnitude of the stop pressure are determined by several factors, including the valve angle, the contact angle, the width of the channel, and the liquid vapor surface tension.

Various silanes have been tested for modifying the surface of the silicon nitride. n-octyltriethoxysilane (OTS, United Chemical Technologies) is effective at increasing the hydrophobicity of the surface just enough to allow the stop valve to work without preventing the catalyst solution from wicking into the tubes. Stop valves with silicon, silicon dioxide, and silicon nitride surfaces modified with OTS can effectively arrest the fluid flow. Figure 14 shows aqueous liquid loaded effectively into the fluidic channels of the reactor and held at the stop valve.

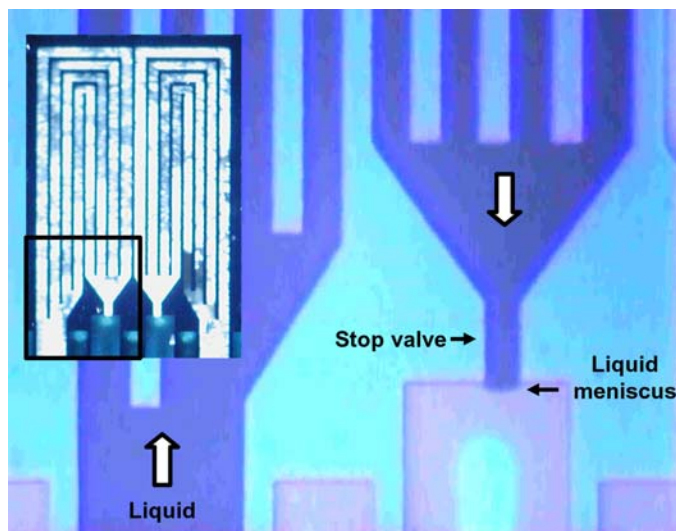


Figure 14: Enhanced contrast micrograph of water loaded into a channel containing a fluidic stop valve. The surfaces have been silanized with OTS to increase their hydrophobicity. The inset shows how this technique can be used to control the catalyst deposition within the suspended-tube reactor (catalyst is white). A glass-capped, oxidized silicon test wafer was used for the visualization.

### 6.3 Autothermal Hydrogen Generation

The suspended-tube MEMS fuel processor is designed to generate hydrogen in a high-temperature reaction zone. Within this zone, two distinct reactions take place. In one channel, a fuel is combusted over a catalyst to generate heat. This heat allows the entire reaction zone to be maintained at an elevated temperature with no electrical power input at steady-state. In addition, this heat is used by an endothermic process occurring in the second channel, in which a fuel (not necessarily the same fuel used for the combustion) reacts over a catalyst to form hydrogen and other side products. Various fuels, such as hydrogen, ammonia, methanol, propane, or butane (or combinations of these) can be used on the combustion side. Similarly, several fuels can be used on the endothermic side. For example, hydrocarbon or alcohols can be processed via steam reforming to produce hydrogen. Alternatively, ammonia or methanol can be decomposed (cracked) catalytically to generate hydrogen. For the evaluation of the fuel processor, two reaction systems were considered: (1) catalytic combustion (various fuels), and (2) catalytic ammonia cracking. Product gas compositions are analyzed online with a time-of-flight mass spectrometer (Inficon H300M Transpector) and a micro gas chromatograph with thermal conductivity detection (Agilent, PPU 6 and MolSieve 5A columns).

All of the present results were performed in 7-slab reactors with the parallel microchannel reactor design with functional stop valves and calibrated Ta/Pt/Ta heaters. These reactors had several practical advantages over the other designs, including facilitated loading of catalyst, lower pressure drop, larger combustor volume, and the 7-slab structure which generally was more robust than the 3-slab structures during routine handling and for vacuum testing.

Simultaneous butane combustion and ammonia cracking were carried out in the suspended-tube reactor over washcoated catalyst particles. The catalysts used in this study were deposited from aqueous slurries containing fine powders of 1 wt.% Pt on La-doped  $\gamma$ -Al<sub>2</sub>O<sub>3</sub> (Alcoa Ga-

200LSF Alumina) reduced *ex-situ* in 100% H<sub>2</sub> at 300°C. During the autothermal portion of this experiment, net hydrogen was achieved from the reactor with no electrical power input.

Hydrogen combustion occurs to full conversion (> 99%) throughout a broad range of flow rates (Figure 15). The hydrogen ignites after slight heating using the integrated heaters (and in some cases from the heating within the testing fixture, which is maintained at ~120°C during combustion experiments). Through hydrogen combustion combined with ammonia cracking, significant production rates of H<sub>2</sub> have been demonstrated from ammonia. Hydrogen combustion and ammonia conversion have been carried out autothermally in a controlled fashion.

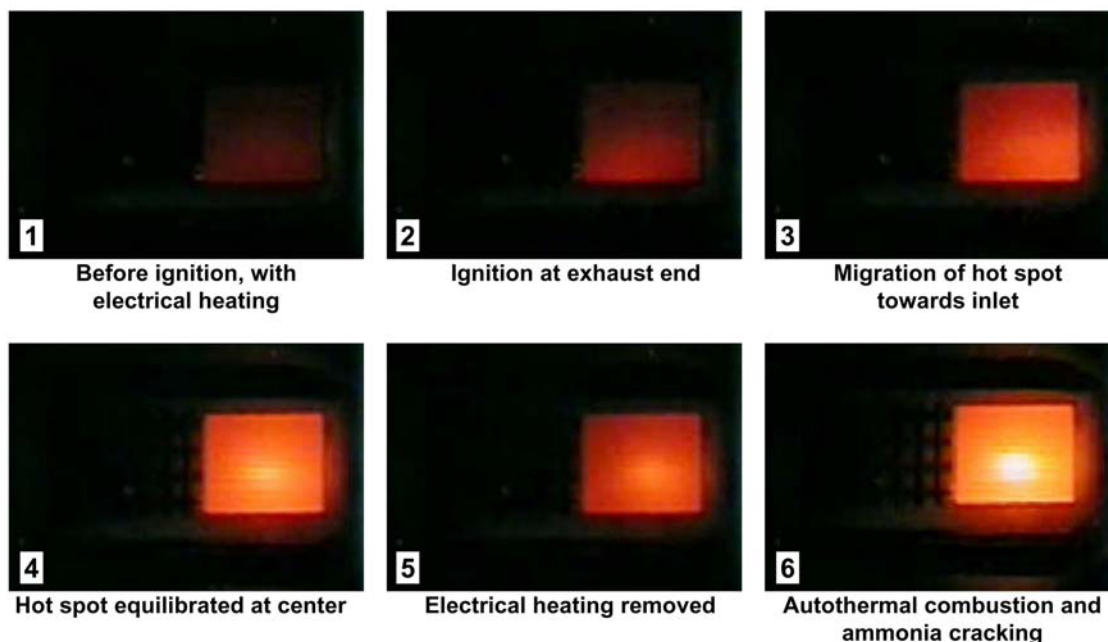


Figure 15: Sequence of images (over the course of ~ 10 s) showing the ignition of hydrogen in the bottom channel of the reactor, with ammonia flowing in the top channel.

Ammonia combustion and ammonia cracking have been carried out under vacuum over Pt on La-doped  $\gamma$ -Al<sub>2</sub>O<sub>3</sub> catalysts. In the first series of experiments, autothermal ammonia cracking was carried out independently at a pressure of ~30 mTorr as the flow rate of ammonia was varied. In the second set of experiments, autothermal ammonia combustion with simultaneous ammonia cracking was carried out at a fixed flow rate of reactants as the ambient pressure was varied. Stable autothermal ammonia combustion with simultaneous ammonia cracking was observed between ambient pressures of 200 and 850 mTorr (Figure 16).

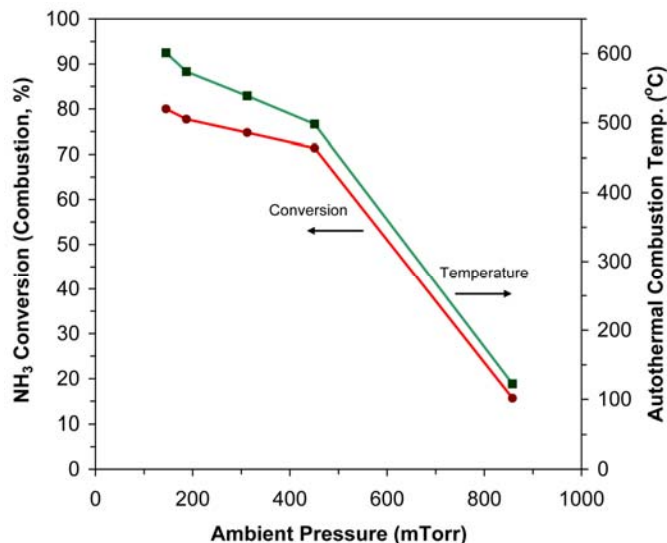


Figure 16: Ammonia conversion (stoichiometric combustion in simulated air) and autothermal reaction temperature as a function of ambient pressure during simultaneous combustion/cracking. Ammonia flow rate to the combustion side is 2 sccm. Ammonia flow to the cracking side is 10 sccm.

### 6.3.1 Summary of Reaction Testing Results

Ammonia cracking has been demonstrated in several different experiments. In addition, homogeneous fuel combustion has been demonstrated using various fuels. Table 1 summarizes the results from the ammonia cracking. Table 2 summarizes the autothermal combustion results.

Table 1: Ammonia Cracking Summary

Run	Heating Method	Catalyst	NH <sub>3</sub> Feed (sccm)	Temp. (°C)	Peak Conv. (%)	Peak H <sub>2</sub> Prod. (μmol·s <sup>-1</sup> )	Peak H <sub>2</sub> Prod. (W <sub>LHV</sub> )
1	Heater, 2.4W	Ir	16	>800 (est.)	26	1.1	0.27
2	Heater, 1.8W	Ir/Al <sub>2</sub> O <sub>3</sub>	6	>800 (est.)	97	6.5	1.6
3	Butane comb.	Pt/La-Al <sub>2</sub> O <sub>3</sub>	12.5	680	3	0.4	0.10
4	H <sub>2</sub> comb.	Pt/La-Al <sub>2</sub> O <sub>3</sub>	12.5	> 936	89	8.2	2.0
5	H <sub>2</sub> comb.	Pt/La-Al <sub>2</sub> O <sub>3</sub>	12	930	1	0.1	0.03
6	NH <sub>3</sub> comb.	Pt/La-Al <sub>2</sub> O <sub>3</sub>	10	600	0.06	0.006	0.002

Table 2: Summary of Autothermal Combustion of Fuel/Air

Fuel	Catalyst	Fuel Flow (sccm)	Conv. (%)	Heat (W)	Temp. (°C)	Comments
Butane	Pt/Al <sub>2</sub> O <sub>3</sub>	0.44	90	0.80	-	Unstable
Butane	Pt/La-Al <sub>2</sub> O <sub>3</sub>	0.63	65	0.83	700	Unstable
Propane	Pt/La-Al <sub>2</sub> O <sub>3</sub>	2.0	46	1.4	770	Stable with combustion in both channels (for TPV)
H <sub>2</sub>	Pt/La-Al <sub>2</sub> O <sub>3</sub>	2-12	>99	2.2	400-930	Stable up to 12 sccm fuel flow
NH <sub>3</sub>	Pt/La-Al <sub>2</sub> O <sub>3</sub>	2-6	92-68	0.3-1.0	590-650	Under vacuum

Results obtained to date for the microfabricated fuel processor have been promising. However, analysis of heat loss during operation, as described above, indicates that the MEMS suspended-tube reactor/heat exchanger should be vacuum packaged in order to maximize energy output.

#### 6.4 Thermophotovoltaic Power Generation

The developed suspended tubes microreactor and heat exchanger was also considered for applications in thermophotovoltaic (TPV) power generation (Figure 17). Energy conversion is achieved using one GaSb diffused junction photocell (purchased from JXCrystals Inc.) mounted on an aluminum heat sink and placed about 1 mm from the emitter. This photocell was the best commercially available for our application at time. Autothermal combustion of propane and air was successfully achieved in the reactor (Figure 19). During autothermal combustion, the maximum output power of the photocell was 1.0 mW, which corresponds to a power density of 32 mW/cm<sup>2</sup>. This constitutes net electrical power generation in a MEMS device using TPV. The system efficiency, defined as the power output of the photocell divided by the thermal power released from the combustion, was 0.08%.

These recorded results are a proof of concept for the TPV micro-generator. Although power outputs and efficiencies are relatively low, they show promise for further improvements to the device operation. Using one photocell on each side of the reactor will double the power and the efficiency. Second, vacuum packaging will eliminate heat losses to the air, increasing the radiative component of heat loss by a factor of three, thereby increasing the efficiency by a factor of three. Third, larger temperatures of reaction will significantly enhance efficiency as radiation scales as T<sup>4</sup>. TPV performance can be further increased by incorporation of better radiation matched photovoltaic cells and radiation filters to increase the yield of the emitted photons and reduce thermal losses. Since this MURI concentrated on the fuel processing applications, i.e., hydrogen generation, the potential TPV improvements were not pursued beyond the proof of principle.

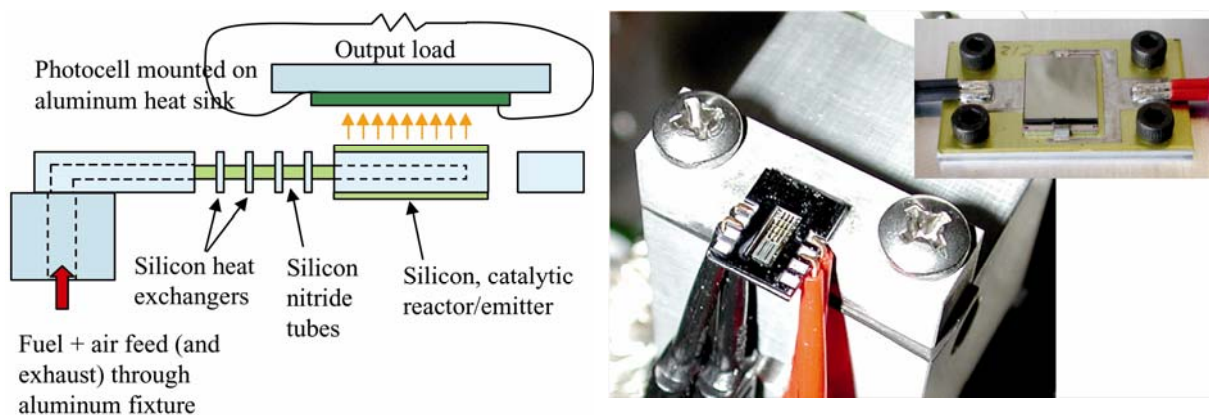


Figure 17: Schematic and photograph of the suspended-tube reactor in a TPV micro-generator configuration.

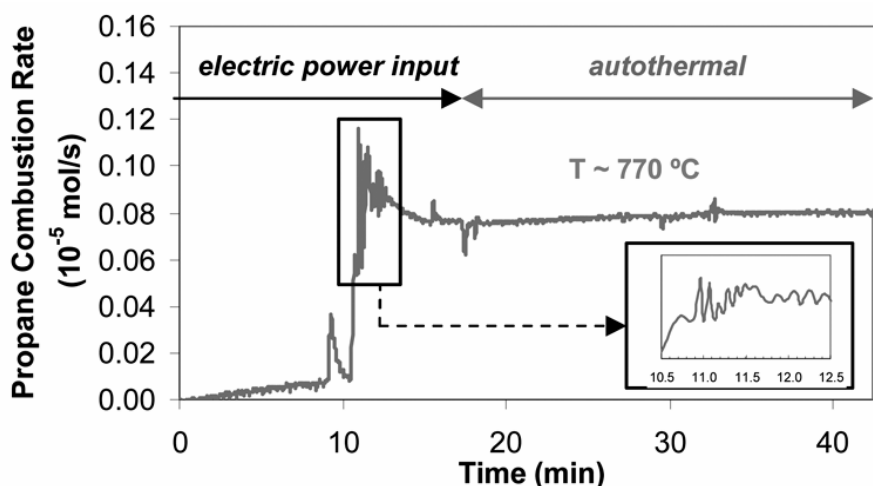


Figure 18: Stable and autothermal propane combustion in the suspended tube reactor.

## 6.5 Next Generation Microfabricated Fuel Processors

In addition to work on combustion, partial oxidation, and reforming thermophotovoltaic power generation (TPV) power generation was successfully carried out with the original suspended micro-reactor (abbreviated as  $S_{\mu}RE$ ). This device, as originally developed, depended on the fabrication of a number of enclosed cavities and long trenches that enabled the formation of the free-standing silicon nitride tubes. These etched features were covered on both sides by a specifically defined thickness of silicon ( $20\ \mu\text{m}$ ), to allow for the timed release of the whole structure. Due to large etch non-uniformities in the deep reactive ion etching (DRIE) system used for defining these features, leaving  $20\ \mu\text{m}$  (or some other specified thickness) all over the wafer proved difficult. For this reason, silicon-on-insulator (SOI) wafers with the desired thickness in device layer were etched from the back side, using the buried oxide layer as an etch stop. Furthermore, to achieve a similar thickness to cap the other side, ultrathin wafers ( $20\ \mu\text{m}$  thick) were bonded to close up the back side. The use of ultrathin wafers was problematic, because they were expensive and hard to handle. Using silicon dioxide as an etch stop led to charging effects and related lateral etching of channels of features. Although manageable for 4-



inch wafer based fabrication, the problems were accentuated when the fabrication facility switched to 6-inch wafer processing. The difficulties were further complicated for new, more efficient devices (S $\mu$ RE II) designed to have larger surface area and were capable of higher temperatures). It was therefore necessary to come up with a new fabrication processes that avoided these problems altogether.

### 6.5.1 Suspended micro-reactor version III (S $\mu$ RE III)

The new, vertical tube process uses three double-side-polished (DSP) wafers bonded together to define the freestanding tubes. The center wafer is etched completely through, thus avoiding having to leave a specific thickness of silicon, and the two capping wafers are etched by an approximate amount. The result is that no etches are sensitive to non-uniformities in depth. Also, no special wafers such as SOI or ultrathins are used. The result is a much more robust fabrication process. The free-standing silicon nitride tubes are also stronger, due to their circular cross section. The new S $\mu$ REs are larger than before, with the reaction zone measuring 5mm x 5mm rather than 1.5 x 2.5 in the old design. Schematics and photographs of the new reactor are shown below in Figure 19 and Figure 20, respectively.

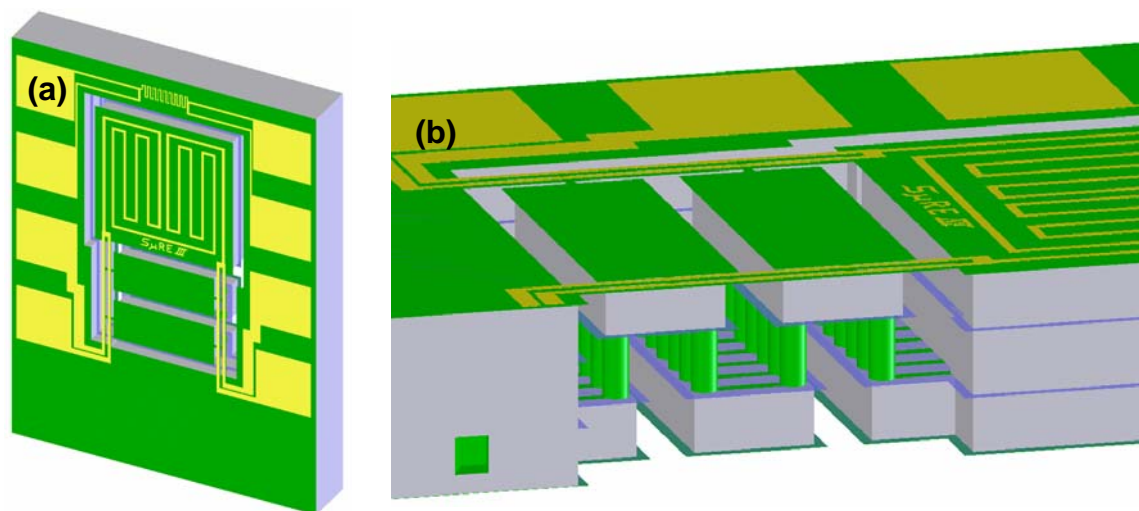


Figure 19: S $\mu$ RE III schematics, (a) top view, (b) cross-section showing suspended silicon nitride tubes, heat exchangers and reaction chamber (grey = silicon, green = silicon nitride, blue = silicon dioxide, yellow = platinum).

Devices were successfully tested with electrical heating in air and vacuum to determine the thermal characteristics of S $\mu$ RE III. The data agreed with the thermal model (Figure 21). The design and fabrication of S $\mu$ RE III pushed the limits of the suspended silicon nitride tube technology, pioneered with S $\mu$ RE I. It also provided an interesting combination of fabrication techniques to achieve the peculiar geometry necessary to build tubes with circular cross-section. The high thermal efficiency of the device, due to both the tubes and the effective heat exchangers, is potentially useful for many high-temperature chemical applications.

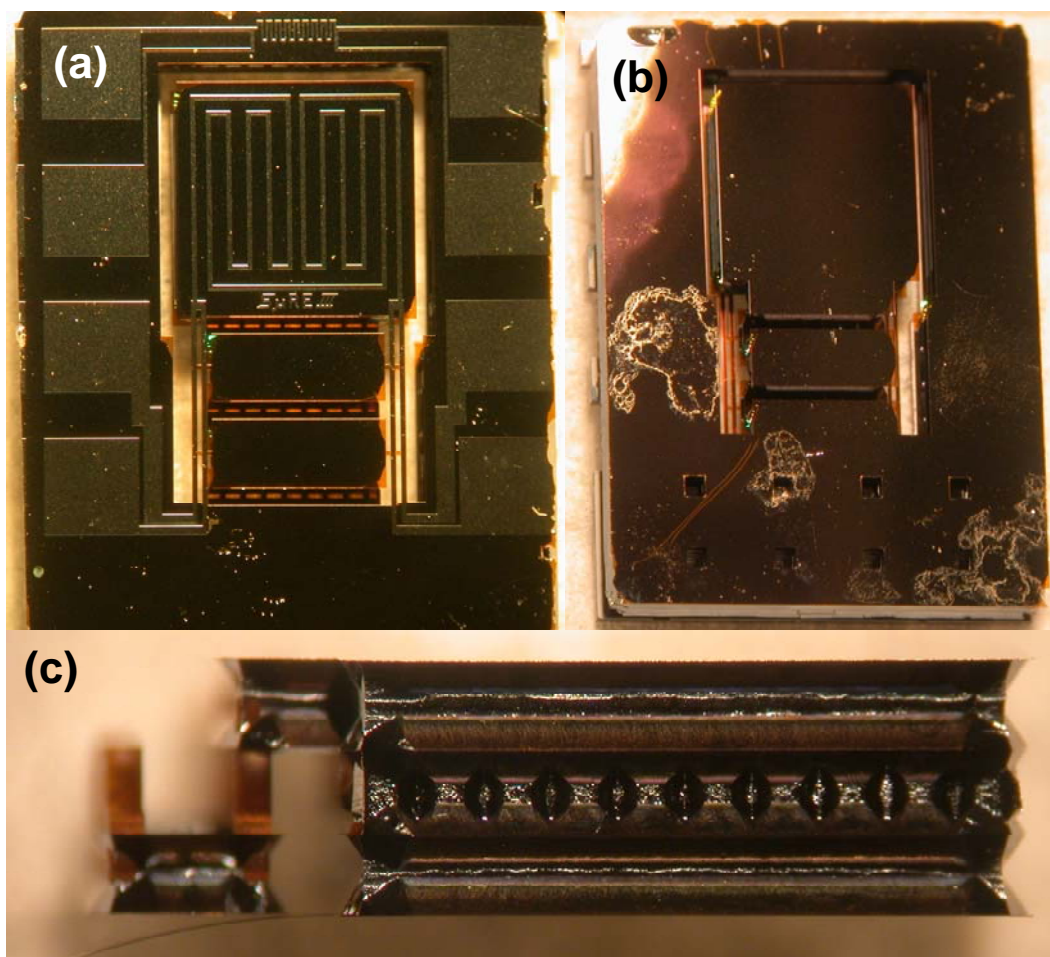


Figure 20: S $\mu$ RE III fabricated device, top (a) and back (b) views. Rounding of corners is an etch artifacts. (c) Fracture S $\mu$ RE III device, showing reaction chamber, 2 sets of 8 tubes, and one heat exchanger.

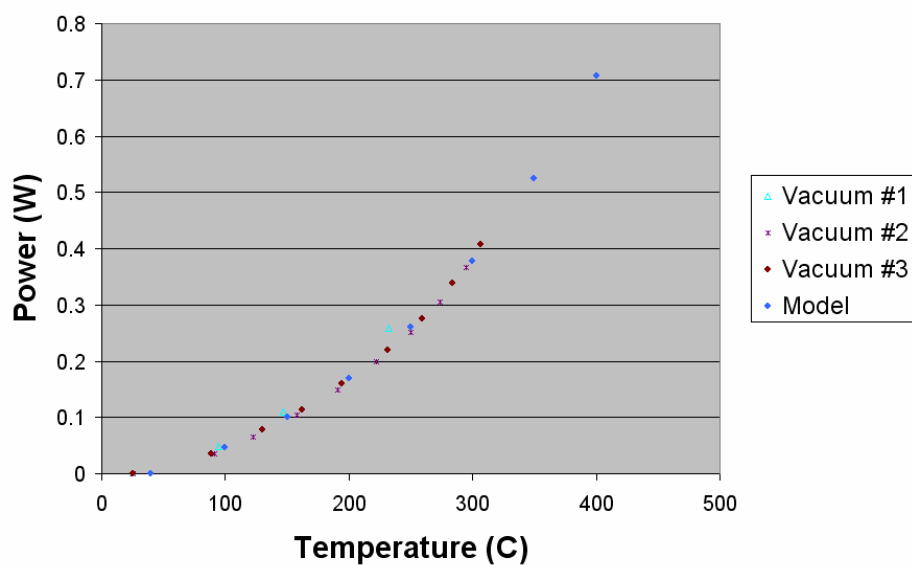


Figure 21: Matching of vacuum data from S $\mu$ RE III with thermal model.



### 6.5.2 Microfabricated Fuel Processors by KOH Etching

An alternative method of fabricating a high-temperature micro fuel processor has been developed. The new method makes use of KOH wet etching rather than deep reactive ion etching (DRIE). Choosing KOH as the process etchant provides several advantages. First, KOH etching is economical; DRIE requires the purchase of expensive machinery that may require frequent and costly maintenance. Furthermore, KOH etching allows for convenient parallel processing as multiple wafers can be etched in a single bath. DRIE requires wafers to be processed one at a time. Finally, etch uniformity is more easily achieved using KOH.

KOH etching also poses disadvantages that must be compensated for in the process design. For example, KOH etching a (100) wafer produces features with a maximum aspect ratio of 0.72:1. Thus narrow, deep trenches are very difficult to fabricate. Additionally, due to the highly anisotropic nature of a KOH wet etch – specifically the preference for etching the {411} planes – smooth curves cannot be etched into the surface of a (100) wafer, and carefully designed corner compensation structures must be used during etching to ensure the integrity of channel corners.

The new micro fuel processor design is modular in nature (Figure 22). Two separate components are fabricated and integrated via glass brazing. The two components include the reaction zone (measuring 1 cm on each side) and a supporting frame that aids in thermally isolating the reaction zone from the ambient. For each of the components, the channel design is etched into two Si wafers. Next, wafer to wafer bonding is used to bond the two wafers together, effectively converting the channels into enclosed conduits. In the case of the supporting frame, a cavity must be etched completely through the wafer. This cavity serves as the housing for the reaction zone. In order to create the cavity, the silicon wafer is etched from both sides, halving the etching time.

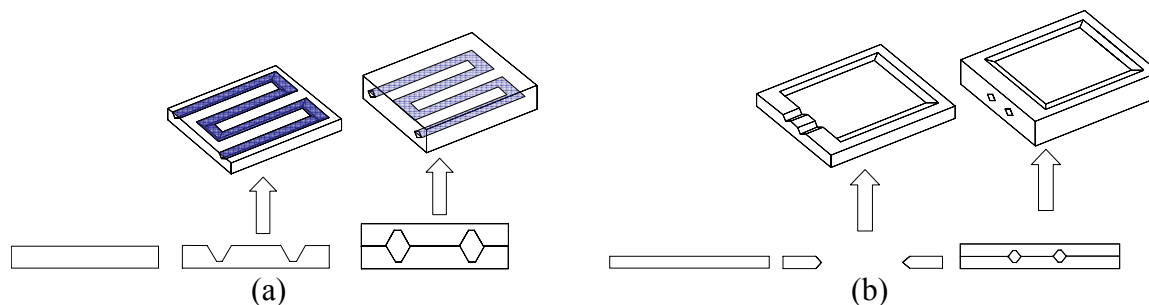


Figure 22: Fabrication outline for the (a) reaction zone and (b) supporting frame

Before assembling the processor, catalyst is loaded directly into the reaction zone. Direct loading prevents buildup of catalyst in the inlet conduit, which can lead to premature combustion of the reactants and, ultimately, reactor failure. 5% Pt on  $\text{Al}_2\text{O}_3$  pellets are reduced *ex-situ* at 350°C in flowing hydrogen. Slurry suspensions are prepared by adding 0.05 mg of finely ground catalyst per 1  $\mu\text{L}$  of water. The slurry is loaded into the reaction zone using a micropipette and dried on one side at 80°C for 1 hour. The process is then repeated, and the catalyst is dried on the other side. This method leads to even deposition of more than 2 mg of catalyst along the reactor walls. After loading the catalyst, the inlet and outlet are packed with acid washed quartz wool. This helps to prevent catalyst leaching and homogenous combustion of the reactants.

Once packed, the reaction zone is connected to the supporting frame via cylindrical borosilicate glass capillary tubing. Glass has been chosen due to its high melting point and low thermal conductivity ( $\sim 1.4 \text{ W/m K}$ ), which will allow the fuel processor to withstand high burn temperatures ( $\sim 700^\circ\text{C}$ ) while minimizing the amount of energy lost to the ambient. The tubing is  $550\mu\text{m}$  in outer diameter with a wall thickness of  $75\mu\text{m}$ .

The glass tubing is bonded to the silicon components via a glass braze. In this method, finely ground glass particles (Sem-Com SCC-7) are suspended in water and applied at the interface of the tubing and the silicon. The tube is aligned using a brazing chuck, and the assembly is heated to  $700^\circ\text{C}$ . For testing in ambient atmosphere, fluidic connections are made directly to the supporting frame. For vacuum testing, epoxy is used to attach the frame to an aluminum bar through which fluidic ports have been bored (Figure 23). The aluminum bar is then compression sealed inside a custom fabricated vacuum chamber (**Error! Reference source not found.**).



Figure 23: Assembled micro fuel processor

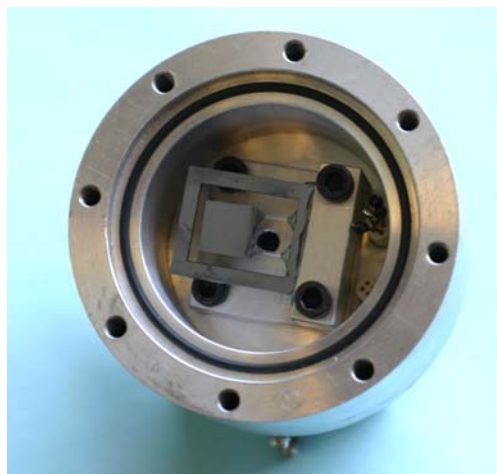


Figure 24: Vacuum chuck assembly

Autothermal, steady combustion of both hydrogen (Figures 25 and 26) and propane (Figure 27) have been demonstrated. Preliminary results indicate that, at full conversion of hydrogen, the reactor is stable at  $\sim 700^\circ\text{C}$  while the frame remains at  $100^\circ\text{C}$ . Additionally, the glass braze is capable of withstanding temperatures up to  $750^\circ\text{C}$ , and the pressure rating of the device is limited by the burst strength of the glass tubes. Currently, work is focused on automated temperature measurement for combustion of various fuels under 50 mTorr vacuum. Additionally, CFD-ACE is being used to simultaneously model fluid flow, heat transfer, and reaction in a functioning device.

Work has begun on developing a reactor design capable of simultaneous combustion and reforming of conventional fuels to  $\text{H}_2$ . The proposed design is outlined in Figure 28. Three reactors are to be bonded, with the middle reactor dedicated to combustion and the outer reactors dedicated to reforming. The heat from the exothermic combustion process will be used to drive the endothermic reforming.

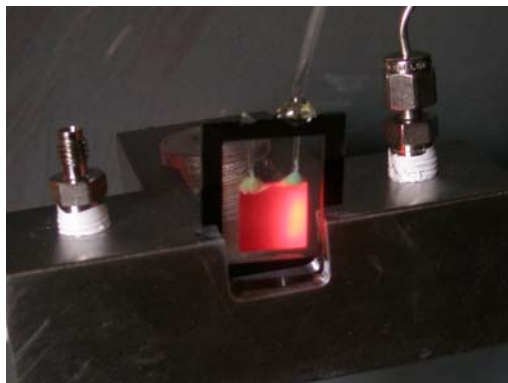
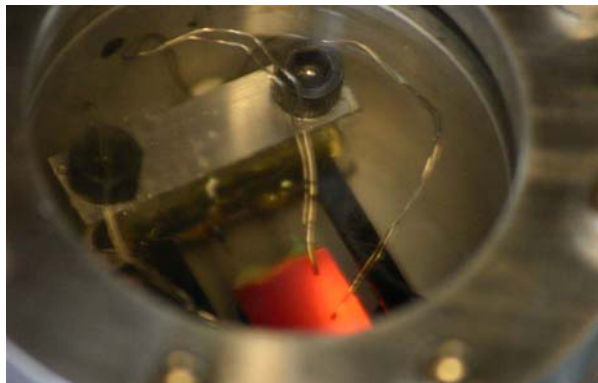
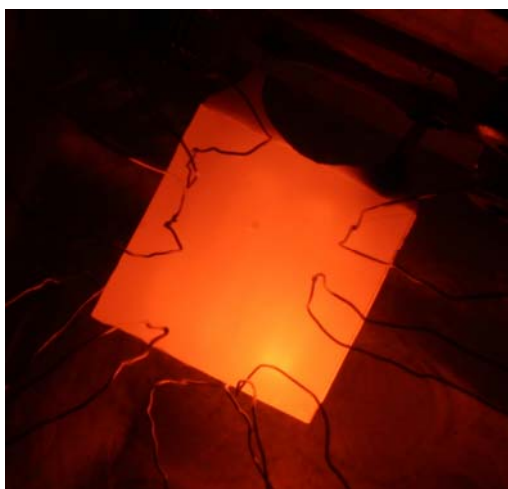
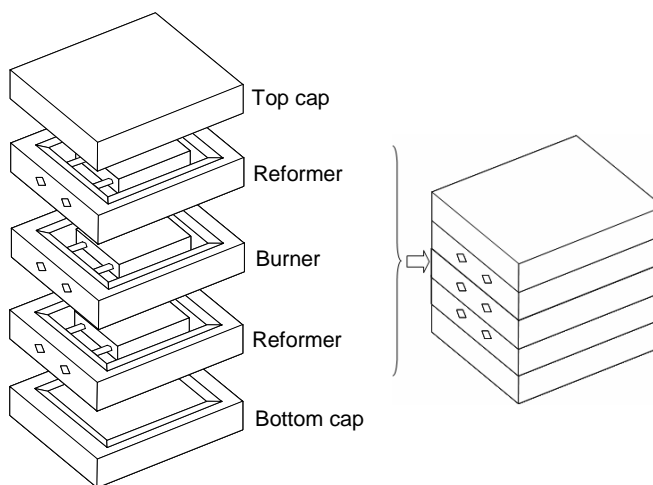
Figure 25: H<sub>2</sub> combustion in atmosphere.Figure 26: H<sub>2</sub> combustion at 50 mTorrFigure 27. Catalytic combustion of propane.  
Wires are thermocouples for temperature measurements.

Figure 28: Reactor configuration for simultaneous combustion and reforming (left expanded view, right compact unit after bonding)

## 6.6 Palladium-Based Micromembranes for Hydrogen Purification

High-purity hydrogen is required for efficient fuel cell operation. While hydrogen storage schemes have been considered by the scientific community (e.g., zeolite sponges, metal-hydrides), on-site hydrogen generation from a more conventional, less hazardous fuel is still preferred for portable-power systems. One avenue for catalytic hydrogen generation is utilization of fuel reforming schemes capable of converting light hydrocarbons to carbon monoxide, carbon dioxide and hydrogen gas via partial oxidation or steam reforming. Subsequent cleanup reactions (e.g. water-gas-shift, partial oxidation) convert carbon monoxide, which has been shown to have a significant, negative impact on PEM fuel cell performance at concentrations  $> 1\text{-}10\text{ ppm}$ ,<sup>1</sup> to carbon dioxide. Recent studies have also demonstrated that even carbon dioxide can have a negative influence on PEM fuel cell performance, as a result of carbon monoxide generation via reverse water-gas-shift reaction involving adsorbed hydrogen at the anode.<sup>2</sup>

An alternate route to hydrogen generation via catalytic cracking of ammonia at high temperatures has been previously demonstrated (see above), employing the suspended-tube

microreactor. While reaction products are only hydrogen fuel and inert nitrogen, thus removing the need for carbon monoxide cleanup, long term exposure to unreacted ammonia may result in permanent damage to fuel cell performance. In light of the inhibiting effects of reaction byproducts present in the hydrogen generator effluent gas, it is desirable to develop a portable hydrogen purification unit that can be placed between the hydrogen generator and fuel cell within an integrated portable-power device. Dense palladium and palladium-alloy films, supported on perforated membranes, have been widely employed in macroscale systems for hydrogen extraction.

We have developed a silicon-based micromembrane architecture, including on-chip heaters and temperature sensors for thin-film studies (see Figure 29). This design utilized a floating  $\text{SiO}_2/\text{Si}_x\text{N}_y$  membrane, which serves as the porous support for the active separation film. Because of the small thermal mass and high thermal isolation associated with the membrane, rapid heating and cooling can be achieved during operation. In addition, the chip temperature remains at ambient even at membrane temperatures in excess of  $500^\circ\text{C}$ , alleviating the need for high-temperature packaging materials or additional thermal isolation of the device. For these reasons, the micromembrane architecture serves as an excellent platform for testing a variety of thin-film applications.

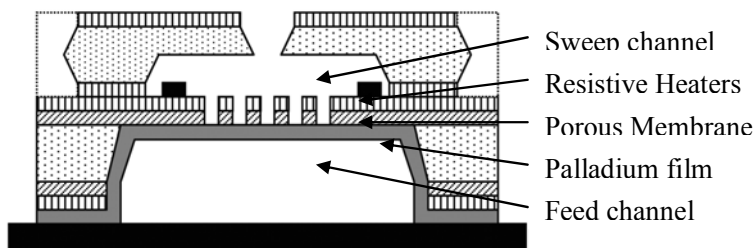


Figure 29. The palladium micromembrane architecture for purification of hydrogen.

The micromembrane device has been shown capable of achieving high hydrogen flux while maintaining competitive selectivity. Experiments were performed at steady-state conditions using fixed sweep and permeate flow rates of 10 sccm each, with a permeate flow composition of 10% hydrogen, and an operating temperature of  $350^\circ\text{C}$ . Hydrogen fluxes of  $3\text{--}4\text{ mol/m}^2/\text{s}$  with average selectivities of  $\sim 1000:1$  are obtained for both pure palladium and 23 wt% silver-palladium alloy films of 0.2 micron thickness. These values are maintained over a prolonged period of time ( $> 10$  hours) with no significant decrease in performance. The hydrogen flux achieved with the 23 wt% silver-palladium film is greater than that for pure palladium, as is consistent with trends reported elsewhere, and is an order-of-magnitude greater than values reported for free-standing 1 micron silver-palladium films employed in similar microdevices.

Exposure tests with ammonia, carbon dioxide and carbon monoxide have also been performed with the MIT micromembrane devices employing palladium and silver-palladium films. Results show that films are minimally influenced by carbon dioxide and ammonia exposure at concentrations of 0.9% and 4%, respectively. While hydrogen flux is reduced upon exposure to carbon monoxide (0.9%), permeation rates are still competitive. These results indicate that the micromembrane architecture is applicable for hydrogen purification, as part of an integrated hydrogen-based portable-power device. Additionally, there is the potential for

incorporating the micromembrane architecture into a fuel reformer for ultra-pure hydrogen generation.

### 6.7 Use of Reforming Catalysts in Palladium-Based Micromembranes for Ultra-Pure Hydrogen Generation

The excellent hydrogen purification of sub-micron silver-palladium films (as compared to conventional silver-palladium film purifiers) led us to use these devices for high-purity hydrogen generation, as part of an integrated portable-power device. The overall strategy was to combine the perm-selective palladium film with a washcoating of a methanol partial-oxidation catalyst, also developed as part of the MURI effort.

Methanol reforming was examined since methanol is an energy-dense liquid fuel that did not present coking problems. While steam reforming reaction gives excellent hydrogen yield, it is quite endothermic and has a lower reaction rate compared to partial oxidation. The latter is exothermic, and can produce enough heat to make autothermal operation a future possibility. Figure 30 illustrates the product selectivity and heat of reaction for methanol partial oxidation based on thermodynamics analysis. In the absence of oxygen, the reaction is classified as endothermic dissociation. At high oxygen/methanol ratios, the reaction proceeds towards complete combustion. Partial oxidation reaction was chosen over steam reforming to avoid water dilution and excessive energy requirements.

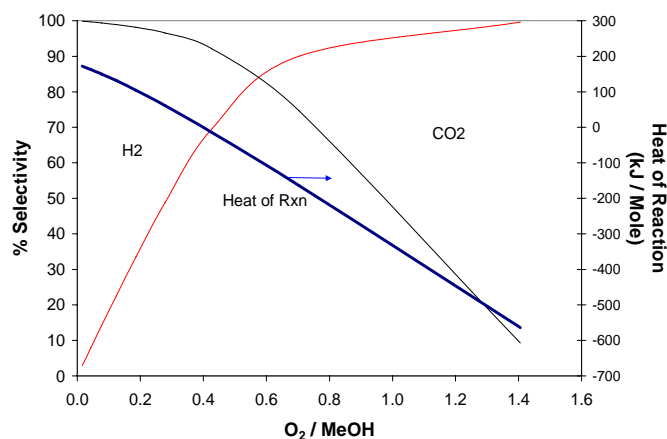


Figure 30: Thermodynamic analysis of methanol partial oxidation.

An initial experiment was performed using an uncoated silver-palladium film to observe the effects of methanol adsorption on the film permselectivity. Introduction of methanol to the feed channel at a partial pressure of 0.05 bar and in the absence of oxygen at a membrane temperature of 400°C resulted in an immediate loss of permselectivity, indicated by the appearance of significant quantities of helium in the sweep effluent. Continued exposure led to a steady increase in helium leakage through the films, suggesting crack formation owing to methanol exposure, as verified by SEM images of the silver-palladium film obtained upon completion of the experiment (Figure 31).

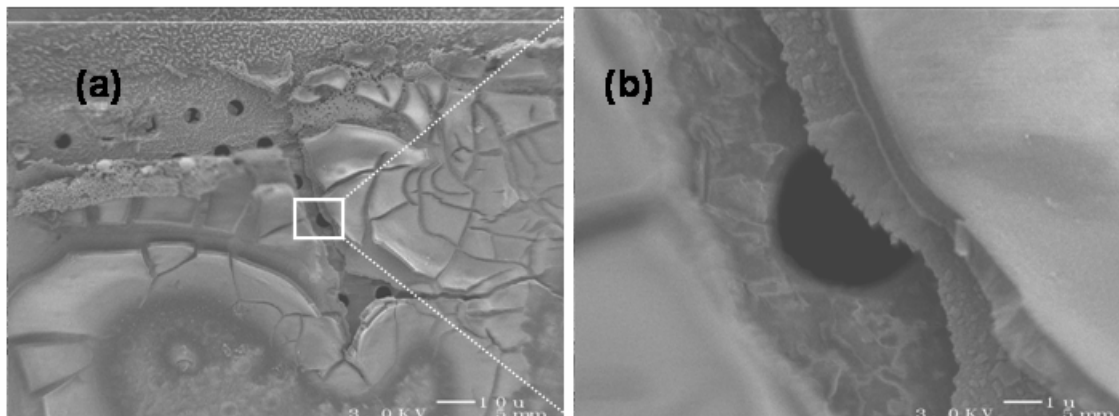


Figure 31: SEM images of 23 weight % silver-palladium film (200 nm) after prolonged (24 hr) exposure to 5% methanol in helium at 400°C.

For the partial oxidation of methanol, a  $\text{La}_{0.95}\text{Co}_{0.05}\text{NiO}_{3-\delta}$  catalyst was developed and synthesized by our group. This nanostructured perovskite catalyst exhibited higher conversions than  $\text{Pd}/\text{Al}_2\text{O}_3$  above 250°C in a packed-bed reactor (Figure 32). It also provided superior hydrogen selectivity compared to the noble metal catalyst. It was noteworthy that for the same weight loading, the catalyst bed for nanostructured  $\text{LaNiO}_3$  took up only 2/5 the bed volume of the noble metal system.

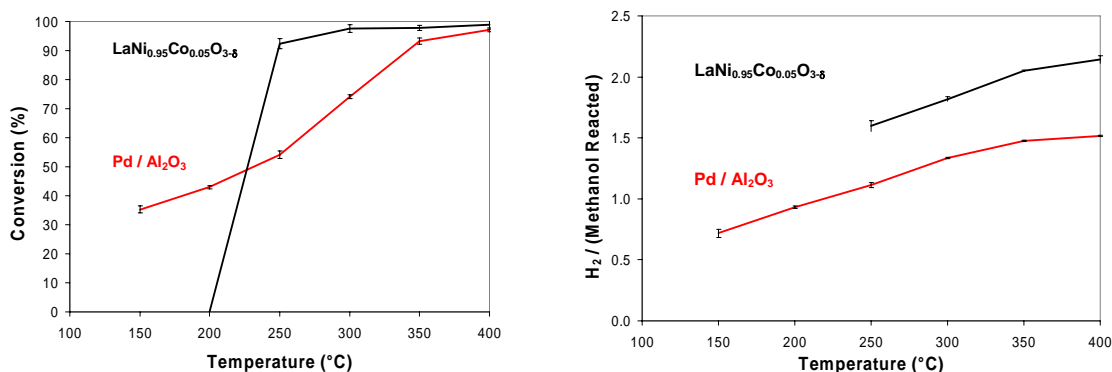


Figure 32: Conversion and selectivity of methanol partial oxidation over  $\text{La}_{0.95}\text{Co}_{0.05}\text{NiO}_{3-\delta}$  and  $\text{Pd}/\text{Al}_2\text{O}_3$ .  $\text{O}_2/\text{methanol}$  feed = 0.5, SV = 4,500 ml/(g cat-min).

The catalyst,  $\text{LaNi}_{0.95}\text{Co}_{0.05}\text{O}_3$ , was synthesized using co-precipitation techniques, milled, and mixed in methanol with  $\text{Al}_2\text{O}_3$  as a coating and binder material. The resulting solution was used to dropwise coat the palladium membrane. Subsequent drying at 350°C produced uniform catalyst coatings that completely covered the underlying metal film and were devoid of cracks (Figure 33).



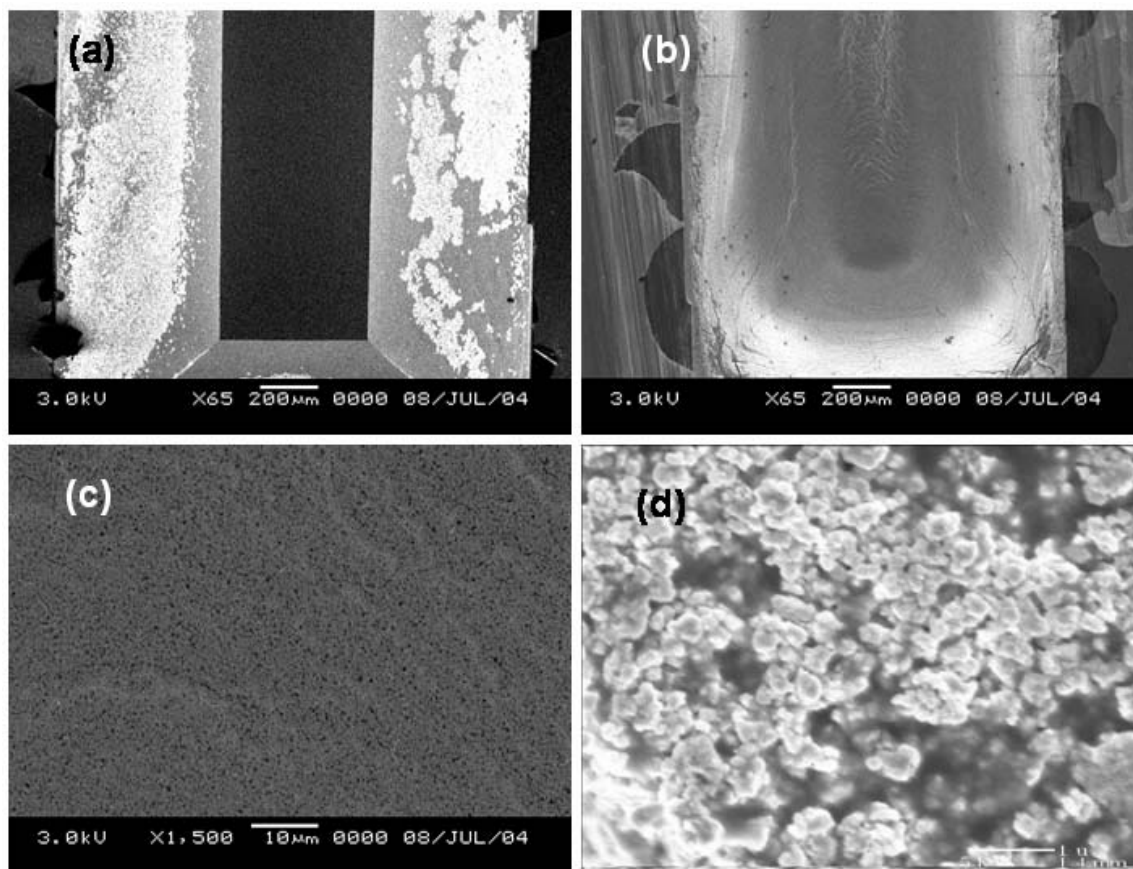


Figure 33: SEM images of the catalyst coating at clockwise increasing magnification: (a) uncoated silver-palladium membrane, (b) catalyst-coated membrane, (c) catalyst coating (2300x magnification), and (d) catalyst coating (13,000x magnification).

A mixture of dilute oxygen and methanol in helium was fed to the washcoated silver-palladium membrane. Methanol was introduced to the reactor via a bubbler filled with methanol, immersed in an ice bath to maintain a methanol vapor pressure of approximately 0.05 bar. Oxygen partial pressure and membrane temperature were both varied to measure performance over a range of operating conditions. Effluent from the feed channel, comprised of unreacted oxygen and methanol, and a mixture of oxidation products, was analyzed using gas chromatography to calculate conversion and selectivity towards carbon dioxide. Nitrogen sweep gas was analyzed via mass spectroscopy to measure both high-purity hydrogen yield and helium leak rates through the film. In all experiments, the gas feed rates prior to the bubbler/chip setup were maintained constant at 10 ml/min. In the present study, the exiting helium composition in the sweep gas was below the reproducible detection limit ( $<0.01\%$ ) during all measurements.

Investigations of device performance over a range of oxygen-to-methanol ratios at a constant membrane temperature of  $400^{\circ}\text{C}$  led to a highest extracted hydrogen yield of 32.4%, at an oxygen-to-fuel ratio of 0.43:1 (Figure 34 left). The membrane temperature was then increased while maintaining constant oxygen feed rates to the bubbler, and reactor performance was measured at each increment. The actual oxygen-to-fuel ratio varied slightly over the course of these four experiments, owing to fluctuations in the methanol bubbler temperature. Methanol conversion, total hydrogen yield and extracted hydrogen yields increased with temperature,

reaching maximum values of 63.4%, 92.1% and 47.0%, respectively, at a membrane temperature of 475°C and a corresponding oxygen-to-fuel ratio of 0.35:1 (Figure 34 right).

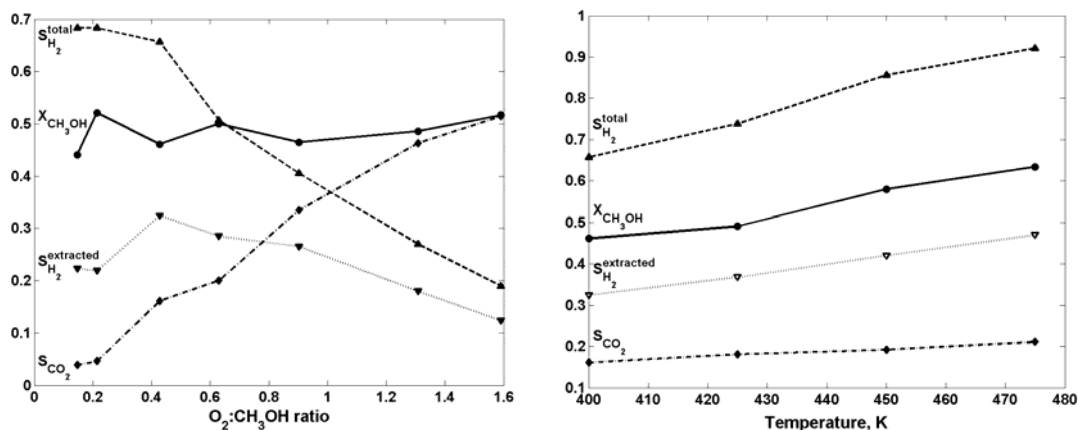


Figure 34: Results obtained for 23 weight % silver-palladium film washcoated with 1.69 gm of 8:1 LaNi 0.95Co0.05O<sub>3</sub> / Al<sub>2</sub>O<sub>3</sub> catalyst, (a) at constant membrane temperature of 400°C and varying O<sub>2</sub>:CH<sub>3</sub>OH ratio, and (b) for varying membrane temperature.

Our findings demonstrate that the catalyst washcoat serves the crucial role of preventing methanol from attacking the silver-palladium surface, thus preventing cracking of the permselective film and allowing successful high-purity hydrogen generation. In addition to serving as a catalytically protective coating, the catalyst layer allows high conversion of methanol to hydrogen. Experimental results demonstrate that the current proof-of-concept system is capable of achieving overall hydrogen yields in excess of 90%, with an extracted hydrogen yield of 47.0% at 475°C and an oxygen-to-fuel ratio of 0.35:1. Even greater extraction yields can be expected by pressurization of the methanol/oxygen feedstream, thus increasing the driving force across the permselective membrane. The overall methanol conversion remained well below 100%, ranging from 44.2 – 63.4% over the parameter space studied, owing to the significant amount of bypass in the open reforming channel. Significant improvements in methanol conversion and available throughputs, and therefore overall hydrogen production, can be achieved by packing the membrane channel with additional catalyst.

### 6.7.1 Autothermal Reforming of Methanol for Solid Oxide Fuel Cells

We have previously demonstrated hydrogen purification using Pd-Ag membranes and the integration of these membranes with LaNiCoO<sub>3</sub> methanol partial reforming catalysts for production of hydrogen.



However, some CO is also produced during the reaction. So under non-ideal conditions the partial oxidation reaction can be represented as:





At 475°C, the maximum extracted hydrogen yield was 47%, but electrical heating had to be used to heat the palladium hydrogen separation membrane and maintain the reaction temperature. Microreactors possess high surface to volume ratio leading to high heat transfer rates to the environment. These losses have to be compensated by thermal management, specifically isolation and energy input from the fuel. The palladium membrane separation process implies an equilibrium amount of hydrogen remains in the exhaust gas. This hydrogen, along with unconverted methanol and carbon monoxide, can be burned by catalytic combustion to provide the necessary energy to make the overall hydrogen generation from methanol autothermal as proposed in (Figure 35).

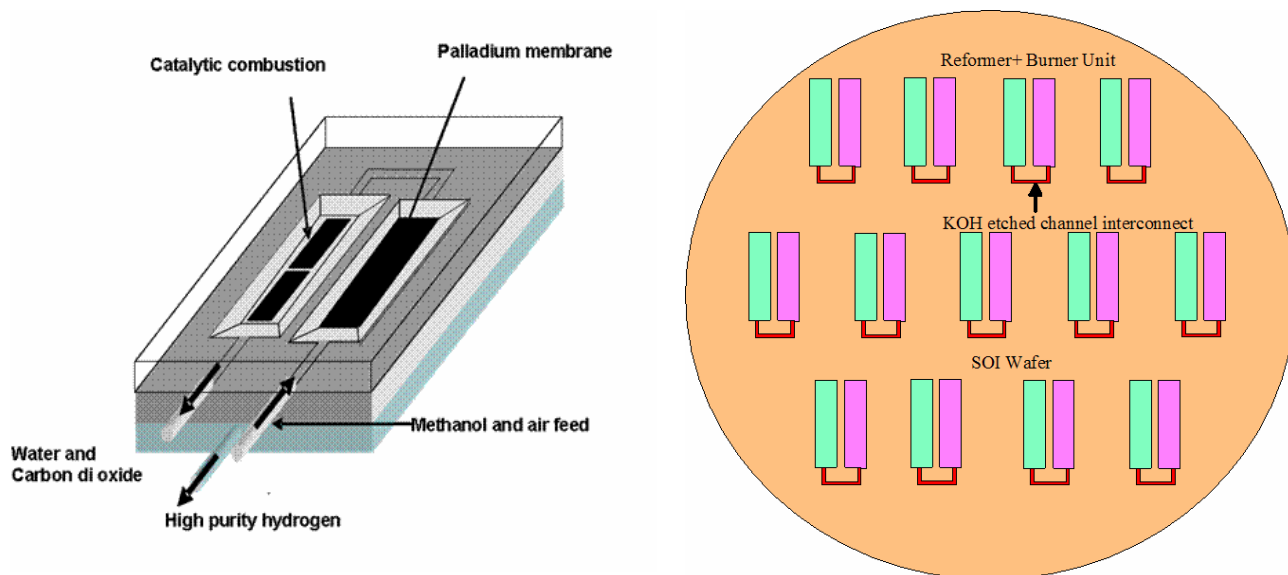
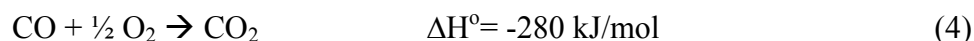
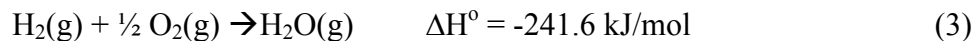


Figure 35: Integrated reformer-burner unit for autothermal reforming of methanol. Left: Schematic of assembled unit. Right: Layout for silicon microfabrication.

In the first step basic calculations including energy balance, pressure drop in the channels and number of burners required per reformer unit based on the current Pd-Ag hydrogen purification design were carried out. Figure 36 compares the energy released by unreformed methanol in the burner with the total energy losses incurred by the device. For example, if 50% methanol is reformed, the remaining 50% can be completely oxidized in the burner to overcome convective losses within 0-0.5W. In the previous design, membranes were fabricated on 650  $\mu\text{m}$  silicon wafers. This restricted the maximum allowable feed gas pressure and thus the hydrogen yields due to membrane stability. Hence in the current design the reactors were fabricated on silicon on oxide (SOI) wafer leading to extra membrane stability and thus allowing higher feed gas pressure for higher conversions and extracted hydrogen fluxes.

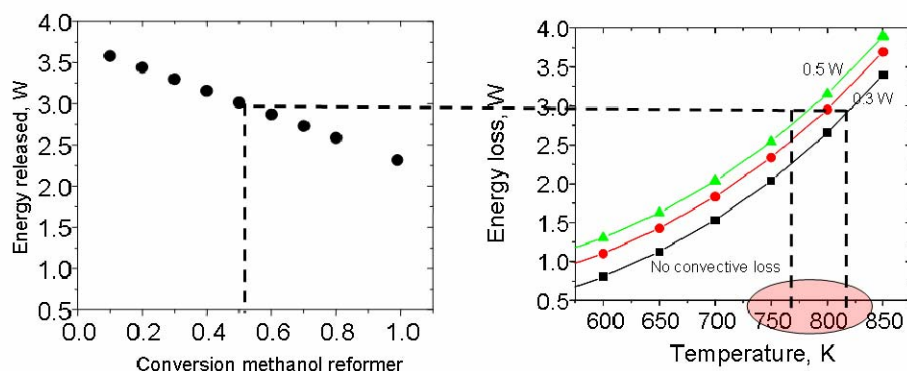


Figure 36: Energy balance for reformer-burner unit

Using standard bulk micromachining techniques, the reactors were successfully fabricated as shown in Figure 37. Dense palladium films were deposited in the reformer for hydrogen purification while the burner was packed with supported platinum catalyst. Upon making fluidic connections, the device was first tested for hydrogen permeation.

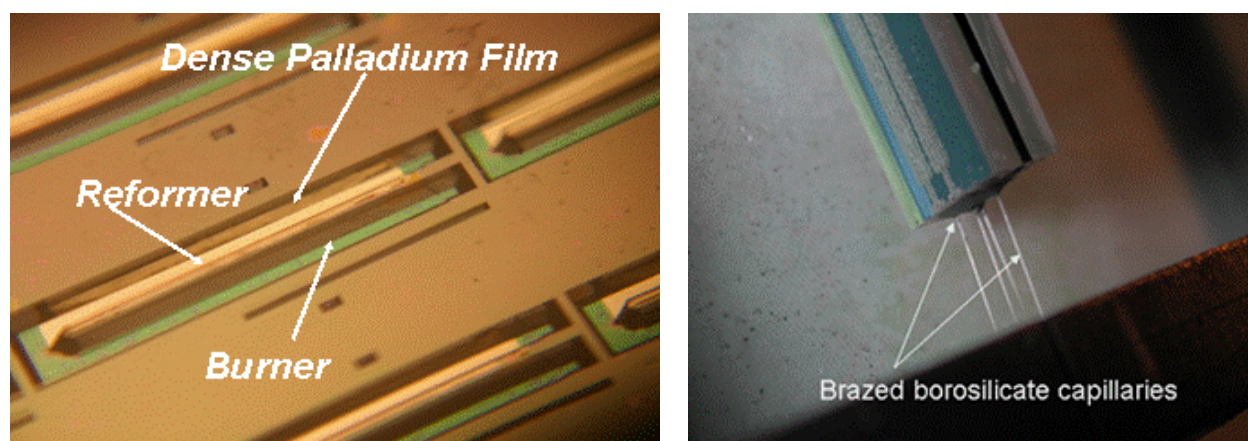


Figure 37: Fabricated reformer-burner units. Left: burner and reformer units on wafer. Right: packaged device with fluidic connections.

As seen in Figure 38, increase in inlet hydrogen stream (90% nitrogen, 10% hydrogen) results in a jump in hydrogen peak on the sweep side and steady nitrogen peak. This indicates that the palladium film is pore free with no pinholes. Finally, results with hydrogen and methanol combustions indicate that excellent heating properties can be achieved by packing supported platinum in the burner unit.

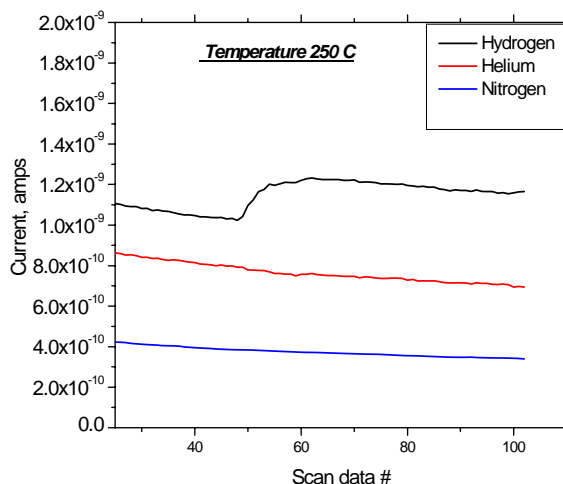


Figure 38: Hydrogen permeation results

## 6.8 Vacuum Packaging

Vacuum packaging is a simple solution to the need for thermal isolation in the micro-fuel processor. Glass frit vacuum packaging was chosen as the ideal method due to the properties of the bonding material. Electrically insulating and excellent reflow characteristics allow for packaging that is compatible with the designs for the suspended tube microreactor.

Work has been done to optimize the presintering parameters and the parameters for bonding in a vacuum environment with GPR-10, a glass frit tape that melts at 485°C. The optimization attempted to minimize the formation of voids that were found in the frit after bonding. A bond that had pores on the order of 10 microns was achieved after being optimized. Unfortunately, this work did not lead to a vacuum package.

Inspired from work on plasma displays, a two-step bond method was developed in attempts to achieve glass frit vacuum packaging. The basic schematic for the process is shown in Figure 39. The capping dies are bonded to the device within a box furnace at atmosphere. The capped device is then placed in a vacuum environment where the pump-out holes are sealed off with a solder or glass frit.

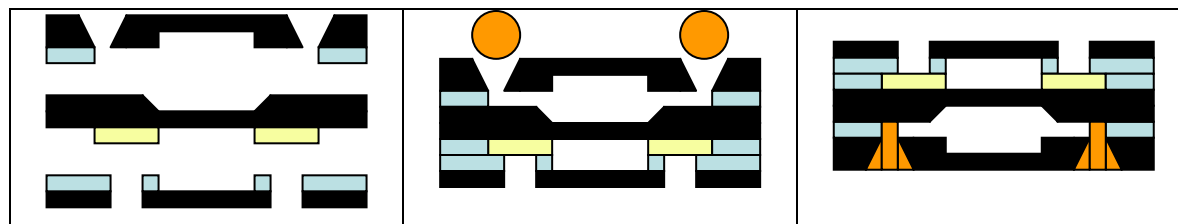


Figure 39: Two-Step Bonding Process (black = silicon, blue = frit, yellow = metallization, orange = solder/glass)

After optimizing the first step of this process, bonding in a box furnace with glass frit tape, it was found that a hermetic seal can be achieved. Heating the sealed sample at 450°C in at 20mTorr for a day did not jeopardize the hermeticity, indicating that a subsequent seal-off at 450°C or lower will produce a vacuum package.

Lead-borosilicate glass preforms that melted at 350°C were chosen for the final seal-off. It was determined after experimentation that boron-oxide, a key component of low melting glasses, outgases when heated in a vacuum environment. This produced bubbling at the melting point of the preforms, leaving a seal with many pores and a failed package. This result provides insight into the void formation and failed packaging attempts with glass frit tape when bonding in a vacuum environment. Good alternative choices for solder were gold-indium that melts at 520°C and gold-tin that melts at 280°C. Gold-indium is better for getter activation but the melting point is a little high. Nevertheless, work with gold-indium produced promising results despite the cost of material.

## **7 Catalysts for Reforming and Solid Oxide Fuels Cells**

### **7.1 Oxidative Steam Reforming of Methanol**

We have developed  $\text{LaNiO}_3$  catalysts for the partial oxidation of methanol. These novel perovskite catalysts showed compact activity with 40% higher hydrogen selectivity than supported palladium catalysts under dilute fuel conditions at full conversion (400°C). Their performance under full-fuel conditions and their integration into a microreformer were examined (see Section 6.8)

Full-fuel conditions were explored at high space velocities in a packed-bed reactor. A 3:1 mixture of water and methanol was preheated with simulated air to 140°C and fed to the reaction zone.  $\text{LaNiO}_3$  and 5 wt%  $\text{Pd}/\text{Al}_2\text{O}_3$  both sustained autothermally once ignited, and data were collected by increasing the oxygen/methanol ratio over time.  $\text{LaNiO}_3$  out-performed 5 wt%  $\text{Pd}/\text{Al}_2\text{O}_3$  at an oxygen/methanol ratio of  $\sim 0.5$  (see Figure 40). The hydrogen yields for  $\text{LaNiO}_3$  and  $\text{Pd}/\text{Al}_2\text{O}_3$  were 84% and 71%, respectively.  $\text{LaNiO}_3$  also demonstrated a much higher  $\text{CO}_2$  selectivity and a higher post-bed temperature. However, the post-bed temperature did not continue to increase at high  $\text{O}_2$ /methanol ratios over  $\text{LaNiO}_3$ ;  $\text{LaNiO}_3$  offered similar hydrogen selectivities as  $\text{Pd}/\text{Al}_2\text{O}_3$  under these conditions.

A thin film of  $\text{LaNiO}_3$  catalyst (Figure 41) was deposited in the channel of a Pd membrane microreactor using an alumina sol. This technique produced a porous catalyst coating that did not significantly lower the membrane permeability. One-step generation of pure hydrogen from methanol was successfully demonstrated. The presence of the palladium film and a fuel bypass in the microreactor presented a very different set-up from the packed bed reactor. However, good (though lower) hydrogen selectivity was still obtained in the microreactor (see Figure 42). The  $\text{CO}_2$  selectivity was shown to be highly dependent on the  $\text{O}_2$ /methanol ratio in the microreactor system. Future studies will involve the optimization of the microreactor design and catalyst loading to obtain a controlled autothermal operation.

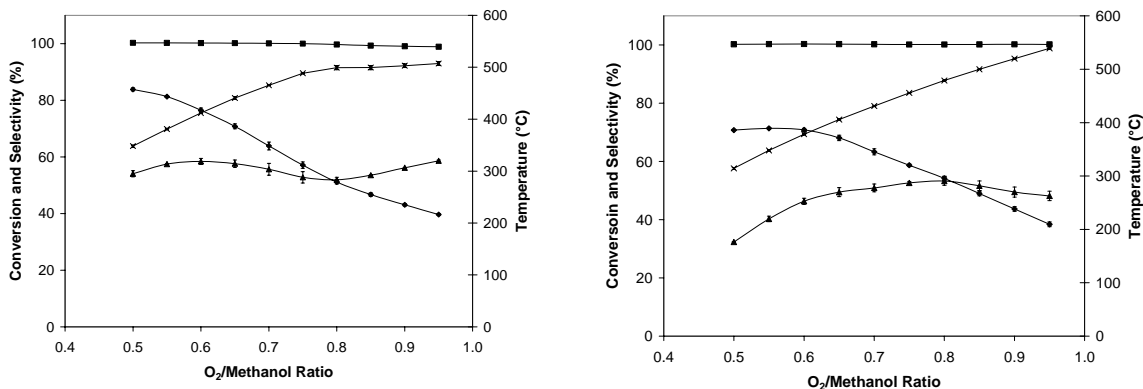


Figure 40: (■) Conversion, (◆) hydrogen and (▲) carbon dioxide selectivities, and (×) post-bed temperature for oxidative steam reforming of methanol over LaNiO<sub>3</sub> (left) and 5 wt% Pd/Al<sub>2</sub>O<sub>3</sub> (right) under full-fuel conditions. The reaction was conducted at a space velocity of 550,000 hr<sup>-1</sup> with a water/methanol ratio of 3 using simulated air as the oxygen source.

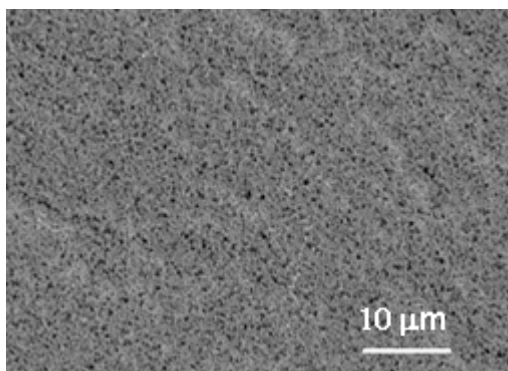


Figure 41: LaNiO<sub>3</sub> film was deposited with fine porosity to catalyze the reaction without significantly lowering the permeability of the underlying Pd membrane.

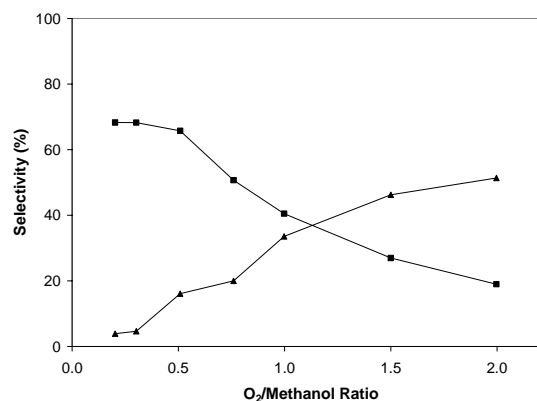


Figure 42: (■) Hydrogen and (▲) carbon dioxide selectivities obtained on the reformate side of the Pd membrane microreactor at 400°C. The reaction was conducted at a space velocity of 350 L/(g<sub>cat</sub>·hr) using a dilute 4% methanol feed without steam addition.

## 7.2 Steam Reforming of Propane

Steam reforming of light hydrocarbons is one of the most important industrial processes for hydrogen production. Our objective was to develop novel steam reforming catalysts that would provide high catalytic activity, excellent hydrothermal stability, good hydrogen selectivity, and high resistance to coking. Propane reforming was examined since propane was an attractive fuel for portable hydrogen production.

Barium hexaaluminate (BaAl<sub>12</sub>O<sub>19</sub> or BHA) and nickel aluminate (NiAl<sub>2</sub>O<sub>4</sub>) were developed as catalysts for this reaction. These complex oxides offered high thermal stability and possessed excellent coke resistance. Ni-coated BHA nanoparticles were synthesized by reverse

microemulsion-mediated sol-gel processing to achieve ultrahigh surface areas. Nanocrystalline nickel aluminates were prepared by chemical co-precipitation. The catalysts were pretreated in 50 sccm flow of 5% H<sub>2</sub> in He for 12 h. The reaction was performed for 12 h in 50 sccm flow of 10% propane in N<sub>2</sub>, with water introduced by a syringe pump.

In the catalyst screening experiments, 700°C-calcined catalysts were examined at 600°C with a H<sub>2</sub>O/C molar ratio of 2. For BHA catalysts coated with 8, 15 and 20 mol% Ni, full propane conversions and stable hydrogen yields were achieved over 12 h. The highest hydrogen yield was attained by the BHA catalyst with 15 mol% Ni, which possessed the highest surface area. This catalyst also provided a relatively high CO selectivity, and relatively low CO<sub>2</sub> and CH<sub>4</sub> selectivities. For nickel aluminate catalysts with Ni/Al molar ratios of 0.25, 0.50 and 0.75, full propane conversions and stable hydrogen yields were achieved over 12 h. The Ni-rich catalyst (Ni/Al molar ratio = 0.75) possessed a lower surface area, but provided a higher hydrogen yield, a lower CH<sub>4</sub> selectivity, and relatively higher CO and CO<sub>2</sub> selectivity.

The optimized BHA catalyst (with 15 mol% Ni) and nickel aluminate catalyst (with a Ni/Al molar ratio of 0.75) were calcined at 700°C, 800°C and 900°C, and run with a H<sub>2</sub>O/C ratio of 2 at 600°C, 700°C and 800°C, respectively. Figure 43 shows that these two catalysts provided similar activities and selectivity. As reaction temperatures increased, their H<sub>2</sub> yield and CO selectivity increased, and their CH<sub>4</sub> and CO<sub>2</sub> selectivities decreased.

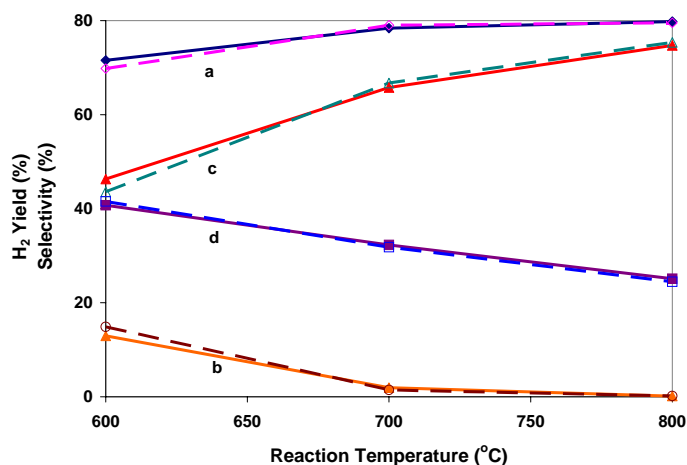


Figure 43: (a) H<sub>2</sub> yield, and (b) CH<sub>4</sub>, (c) CO and (d) CO<sub>2</sub> selectivities as a function of reaction temperature for (—) 15 mol% Ni-coated BHA and (---) nickel aluminate with Ni/Al = 0.75.

### 7.3 Alternative Anode Materials for Direct Hydrocarbon Conversion

Direct oxidation SOFC employs hydrocarbons (typically methane) without steam addition. This nomenclature is complicated in that a dry hydrocarbon feed can still rely on steam to mitigate coking problems. Under normal fuel cell operation, high current flows introduce oxygen into the anode layer to produce sufficient carbon dioxide and water *in situ* to prevent coking. This concept has been shown to be effective on fuel cells with Ni/yttria-stabilized zirconia (YSZ) anodes operating on humidified methane at 800°C<sup>3</sup>. The otherwise stable fuel cell would break in 10 min in the absence of the current flow. At lower temperatures, the fuel cell would survive slightly longer exposures as coking would be less severe.

Other efforts on direct oxidation SOFC are focused on replacing the nickel metal in the anode, for example with a copper-ceria cermet<sup>2</sup>. Higher hydrocarbons such as decane have been used as fuels successfully at 700°C<sup>4</sup>. Since copper and its oxide would melt below typical SOFC fabrication temperatures, the dense YSZ electrolyte in this system is fabricated on a porous YSZ host. The host is then impregnated with the copper and cerium nitrates and calcined; numerous cycles of impregnation and calcination are needed to achieve the desired structure.

This study was focused on the development of novel anode materials for the direct oxidation SOFC. The goal was to modify existing Ni/YSZ anode formulations to dramatically reduce the rate of coking, while employing well-established fabrication techniques. As coking over nickel has been well studied for steam reforming applications, traditional catalyst additives (see Table 3) were investigated for application to solid oxide fuel cells. Beyond reducing the rate of coking, these additives must also be stable at the SOFC fabrication temperature without showing reactivity towards YSZ.

Table 3: Material properties of potential anode additives to improve coke tolerance of Ni/YSZ cermets<sup>5</sup>.

Dopant	Pt	Ir	Cu	Ag	Zn	Ge	Sn	Pb	As	Sb	Bi
Coke Mitigation <sup>5</sup>				+	+		+	+	+	+	+
Oxide Melting Point (°C)			1235		1975	937	1630	886	312	656	860
Metal Melting Point (°C)	1772	2410	1083	962	420	1086	232	328	613s	631	271

Tin was selected as the additive due to the high melting point of its oxide, making it compatible with traditional processing methodologies. Zinc oxide was not selected as it has a high vapor pressure and may lead to desintering during processing. One concern of using tin in the anode structure is that its metallic form has a very low melting point. However, established phase diagrams indicated that for nickel alloys containing less than 40 mol% tin, the metal phase in the cermet anode would be a solid at operating temperatures<sup>6</sup>. Initial studies illustrated that the best performing Ni-Sn anode formulations with regard to carbon mitigation contained ~ 40 mol% Sn in the Ni-Sn alloy, and ~ 40 vol% alloy in the Ni-Sn/YSZ cermet. Figure 44(a) shows that the desired Ni-Sn alloy was successfully obtained by reducing a nickel-tin-zirconium oxide composite, even though the latter has been subjected to significant grain growth and sintering at 1400°C. Only the X-ray diffraction (XRD) peaks for the alloy was detected; no separate Ni or Sn diffraction peaks were noted. Unlike the Ni/YSZ cermet (Figure 44(c)), no graphitic crystalline carbon peak was observed at  $2\theta = 26^\circ$  when the Ni-Sn/YSZ cermet was exposed to dry methane at 800°C for 1.5 h (Figure 44(b)). As amorphous carbon was more readily gasified than crystalline carbon, the lack of graphitic carbon was a promising result.

The dimensional stabilities of Ni-Sn/YSZ (with 40 mol% Sn) and Ni/YSZ anodes were compared at various metal loadings (Figure 45). Increasing dimensional changes and weight gains were observed in the Ni/YSZ system with increasing vol% metal loading. Although some coking took place over Ni-Sn/YSZ (as revealed by the weight gain), this system only experienced minor dimensional expansion above 40 vol% metal loading. It appeared that the strength of the YSZ matrix was also an important variable in stabilizing the system against coking problems. Interestingly, the optimized direct hydrocarbon copper-ceria cermet contains only 14.4 vol% metal. Metal loadings below 30 vol% led to poor percolation in the cermet and low conductivity<sup>7</sup>. The power output of the copper-ceria system tripled after intentional coking, which improved the metal connectivity in the cermet<sup>8</sup>. The stability of our Ni-Sn/YSZ cermet

against structural damage in methane exposure at 800°C was remarkable. No damage to a fabricated fuel cell resulted even with a high metal loading of 40 vol% after exposure to dry methane at 800°C for 1.5 h.

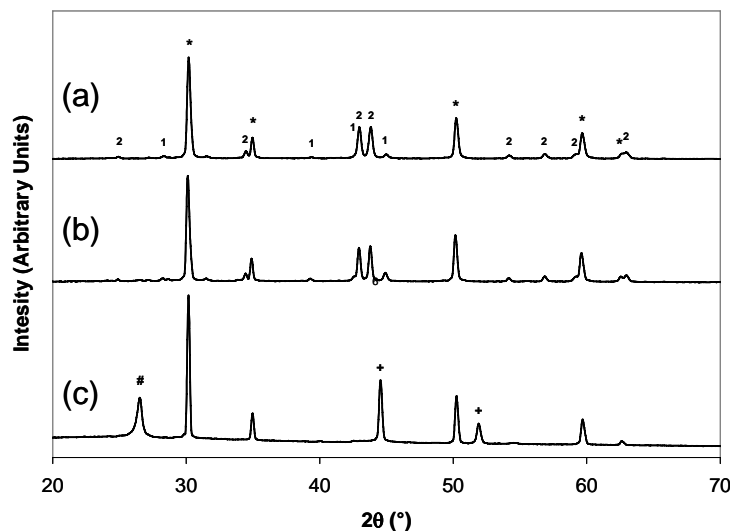


Figure 44: XRD patterns for (a) Ni-Sn/YSZ cermet prepared by reduction of the oxide composite, and (b) Ni-Sn/YSZ cermet and (c) Ni/YSZ cermet after exposure to dry methane at 800°C.  $\text{Ni}_3\text{Sn}_1$  (1),  $\text{Ni}_3\text{Sn}_2$  (2), Ni (+), YSZ (\*), and carbon (#) peaks are denoted.

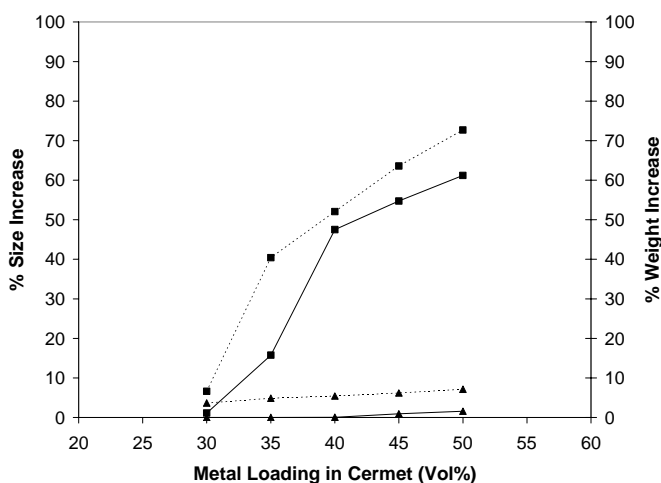


Figure 45: % size increase (solid lines) and % weight increase (dashed lines) in (■) Ni/YSZ and (▲) Ni-Sn/YSZ cermet anodes after exposure to dry methane at 800°C for 1.5 h.

The performance of the optimized Ni-Sn/YSZ anode was characterized in humidified hydrogen and methane. These results were then compared to an identically fabricated Ni/YSZ fuel cell. The highest power density achieved by the Ni-Sn/YSZ anode at 800°C in humidified hydrogen was 210 mW/cm<sup>2</sup> (Figure 46 (left)), which was similar to that obtained with the optimized copper-ceria cermet<sup>9</sup>. In comparison, a Ni/YSZ anode was able to produce a maximum power density of 520 mW/cm<sup>2</sup> (Figure 46 (right)) with similar processing techniques.



With methane, power densities of  $135 \text{ mW/cm}^2$  were observed over the Ni-Sn/YSZ anode material (see Figure 47).

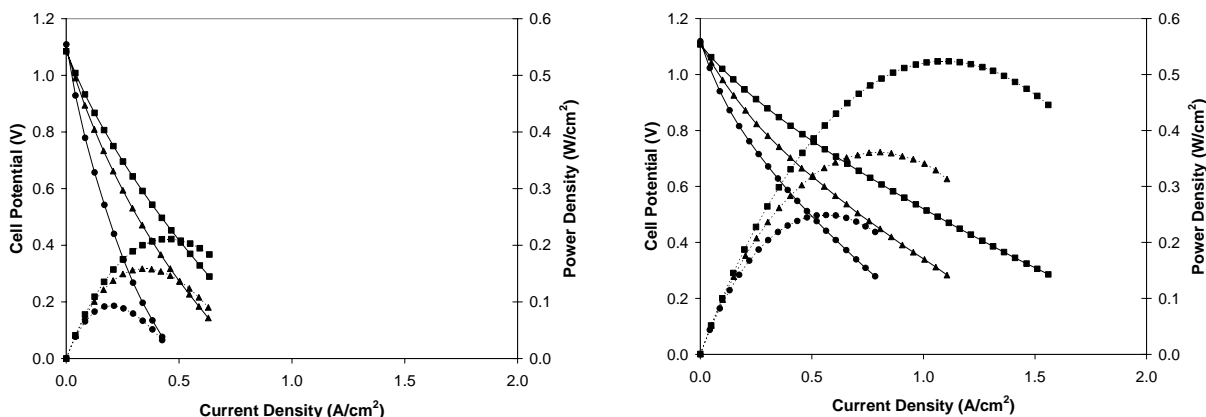


Figure 46: Cell potential (solid lines) and power density (dashed lines) for (left) Ni-Sn/YSZ and (right) Ni/YSZ anodes in humidified hydrogen at (●) 700°C, (▲) 750°C and (■) 800°C.

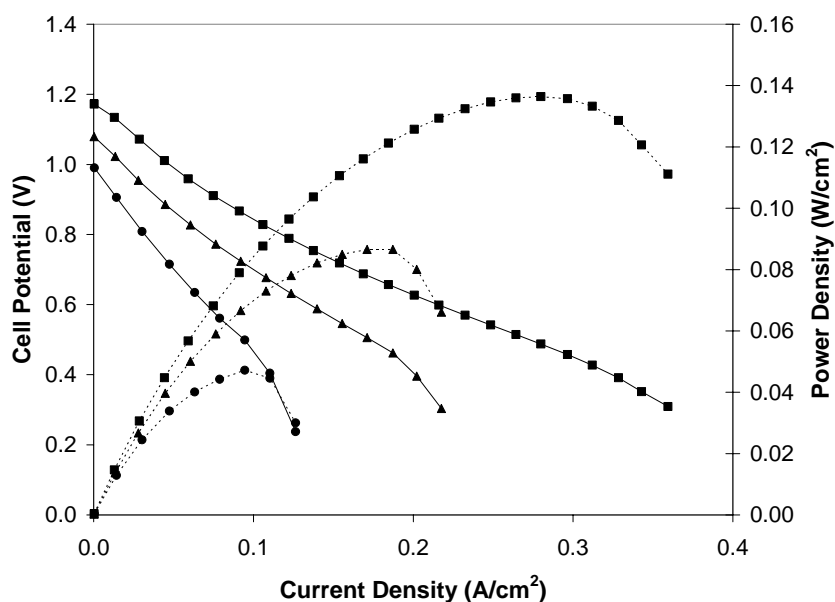


Figure 47: Cell potential (solid lines) and power density (dashed lines) for Ni-Sn/YSZ anode-supported cell in humidified methane at (●) 700°C, (▲) 750°C and (■) 800°C.

#### 7.4 Exploring Materials for Proton Conducting Solid Oxide Fuel Cells

Ionic conducting fuel cell requires operating temperatures of 700°C or higher due to its limited conductivity at intermediate temperatures. These operating temperatures in turn lead to issues of materials compatibility (see Section 9) and low tolerance with respect to variations in operating conditions. Alternatively, proton conductors, typically alkaline earth metal substituted perovskites (e.g.  $\text{BaCeO}_3$ ,  $\text{SrCeO}_3$  and  $\text{BaZrO}_3$ ) exhibit high protonic conductivity even at 400°C<sup>10</sup> they can effectively reduce the operating temperature to the intermediate range.

Therefore, as a parallel effort to building a MEMS ionic solid oxide fuel cell, a proton fuel cell was also considered.

As described above in Section 6.8, partial methanol reforming using  $\text{LaNi}_{0.95}\text{Co}_{0.05}\text{O}_3$  catalyst and subsequent hydrogen clean-up using a palladium film was successfully demonstrated. Using this approach, methanol conversions of up to 93% and extracted hydrogen yield of up to 47% were realized at 475°C. The use of palladium film also assisted in hydrogen purification from the unwanted CO generated during reforming, thus making it attractive for fuel cell application. Hence, we chose to explore the design further to prepare a solid oxide fuel cell (see Figure 48) in which the electrolyte and electrode solutions were spin coated on the Pd membrane device substrate to obtain a hydrogen operated fuel cell.

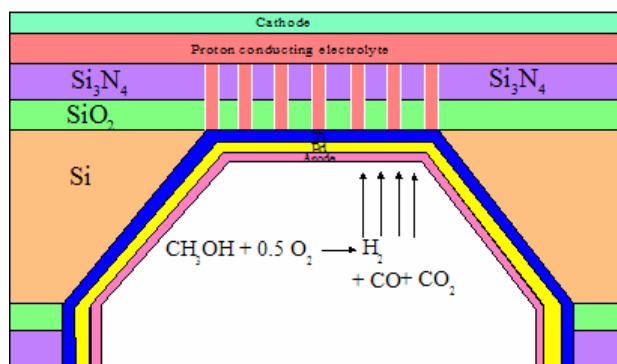
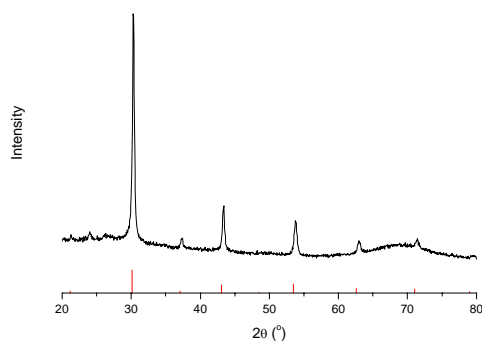
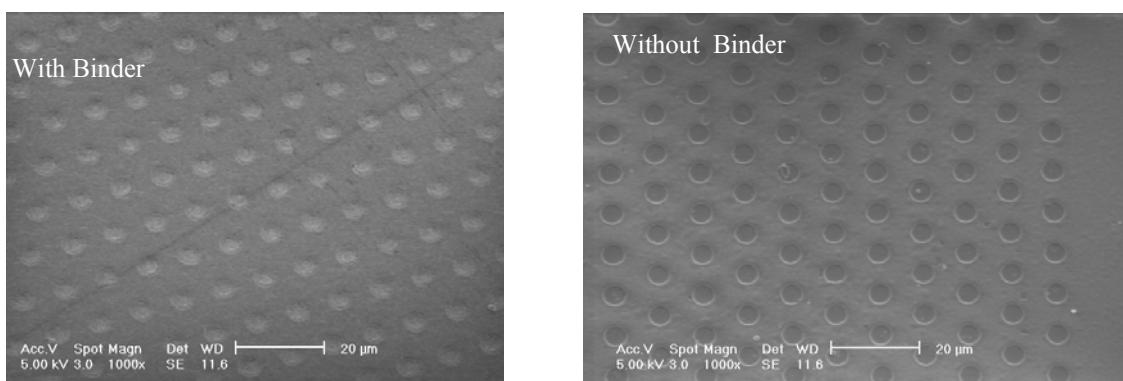
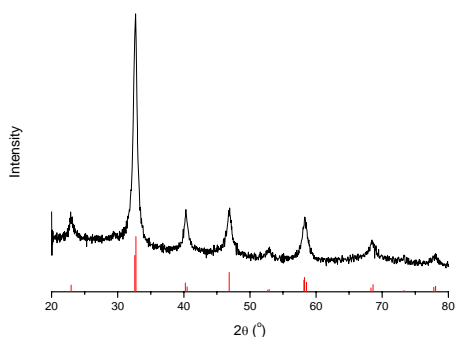
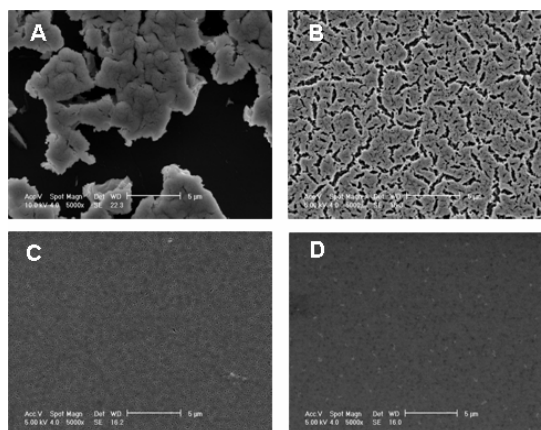


Figure 48: Schematic of microfabricated proton conducting fuel cell.

Standard bulk micromachining techniques were used to fabricate the substrate. Of the perovskite proton conductors, although barium cerate shows a higher conductivity than barium zirconate, its chemical stability is still under study. Thus, yttrium-doped barium zirconate was chosen as the electrolyte in this work. Different recipes were examined to synthesis phase-pure 5–10 mol% yttrium-doped barium zirconate. Water-free acetate-based sol-gel synthesis<sup>11</sup> was selected due to its solution stability and ability to form a perovskite phase. A thin film of  $\text{BaZr}_x\text{Y}_{1-x}\text{O}_3$  (Figure 49) was deposited on the surface of as-prepared silicon wafer through spin coating. To improve the wettability of the top silicon nitride layer, the wafer was plasma treated to build an oxygen bounding layer. Using this approach, a fully covered film was obtained. For electrolyte it is important that a continuous, dense film with uniform composition be deposited on the substrate to lower fuel cross-over and thus increase cell efficiency. To enhance the film thickness and coverage, polyvinyl alcohol, a conventional binder for ceramics processing, was added to increase the viscosity of the solution prior to film deposition. This allowed us to achieve a dense continuous film successfully (Figure 50).

Figure 49: XRD pattern of  $\text{BaY}_{0.05}\text{Zr}_{0.95}\text{O}_3$  thin film on silicon wafer.Figure 50: Scanning electron micrographs of  $\text{BaY}_{0.05}\text{Zr}_{0.95}\text{O}_3$  thin film on silicon wafer, with patterned features.

Lanthanum strontium manganite electrode solution was synthesized through citric gel method with nitrate precursors. The solution was deposited on top of the barium zirconate electrolyte layer (Figure 51). The film porosity could be controlled by adjusting the solution viscosity through adding ethylene glycol (see Figure 52). These results indicate that the final electrode porosity can be optimized by varying this parameter leading to better fuel cell performance.

Figure 51: XRD pattern of  $\text{La}_{0.67}\text{Sr}_{0.33}\text{MnO}_3$  thin film on silicon wafer.Figure 52: Control of film porosity by adjusting the viscosity of  $\text{La}_x\text{Sr}_{1-x}\text{MnO}_3$  solution through ethylene glycol addition.  $\text{La}_x\text{Sr}_{1-x}\text{MnO}_3$ /ethylene glycol weight ratios of (A) 1:0, (B) 1:1, (C) 1:2, and (D) 1:3 were used in the film preparation.

## 8 Microfabricated Solid Oxide Fuel Cells

Microfabrication of solid oxide fuel cells holds many challenges, but also many potential advantages, including the production of very thin—yet pore free—electrolyte films at reduced temperature. By microfabricating the fuel cell stack, dense electrolyte films can be produced at sub-micron thicknesses; thereby enabling the use of SOFC at much reduced temperatures. Thin film anodes and cathodes will likewise enhance ionic conductance in mixed ionic-electronic conducting electrodes. In addition, gas phase diffusion through electrode pores will be rapid, assuming sufficiently high porosity can be realized. The process by which dense thin film electrolytes can be fabricated between highly porous thin anode and cathode films is a unique challenge to be met in this work. Finally, it is well known that surface exchange kinetics can control fuel cell performance which makes the effects of electrode porosity doubly important as the porosity also controls the triple phase boundary [TPB] length. All things being equal, electrode performance is often found to increase with electrode thickness, up to some value where the increased TPB length is no longer useable because the ionic conduction path is too long. This clearly presents a challenge to thin film electrodes, and other methods to increase the TPB length must be examined.

Another challenge and opportunity for micro fuel cells regards the unique microstructures available when microprocessing. Reduced temperature thin film processing commonly leads to nano-scale microstructures. These are reported to exhibit improved or distinctive catalytic activity and transport properties important for reduced temperature operation, though the exact process by which the properties are affected is not well understood at this time. Nano-scale grains have been found to alter the transference number, *i.e.* the ratio of ionic to total (ionic + electronic) conductivity. This presents a unique opportunity to use the same material as an electrolyte, and as an electrode, if different microstructures yield different transference numbers. The specific effects of nano-scale grain sizes and grain-boundary engineering are not well known to the scientific community and so their study imparts opportunities to not only improve performance characteristics, but also to obtain a more fundamental understanding of ionic conductivity in oxide materials.

There is additional utility—and challenge—in using a MEMS-based structure for a SOFC. The power necessary to maintain the membranes at temperature is much reduced compared to conventional SOFC devices and the low thermal mass leads to rapid start-up times—a critical feature for portable applications. Lower processing and operating temperatures may enable the use of advantageous materials or structures that would be unstable at normal SOFC operating conditions. Despite the reduced temperatures, there are questions to be answered regarding heat loss from a suspended film stack to the substrate and out to the environment. Furthermore, freestanding membranes must remain intact and crack-free during thermal cycling to prevent mixing of fuel and oxidizer. Alternatively, one can consider the utility of the single chamber SOFC in which both electrodes are placed on the same side of the electrolyte film. Photolithography processing methods are capable of defining electrodes with very small feature sizes, allowing high TPB length and short diffusion paths between the electrodes. It is uncertain what most limits power production and efficiency in single chamber fuel cells, so this gives significant opportunity for research. Miniaturized solid oxide fuel cells [ $\mu$ SOFC] are also being considered from a theoretical point of view given their distinctive electrode and electrolyte

geometries. The electrode geometries and film thicknesses necessary to achieve sufficiently low polarization resistances are being evaluated for both single and double chamber micro-SOFC.

Key SOFC design challenges under this program are to identify materials which simultaneously satisfy requirements for electrochemical and electrical functionality, chemical and thermo-mechanical compatibility, as well as compatibility with microelectronic/MEMS fabrication. Work has been done to build structures for the testing and characterization of stresses induced in the electrolyte/electrode supported structures during processing as well as during heating-cooling cycles. In the design and fabrication of the MEMS structures, alternate designs are being evaluated based on single and double chamber cells as well as process compatibility. Interactions with catalyst studies are important in helping to identify catalytic materials capable of enhancing electrode performance at the reduced operating temperatures of micro SOFCs.

In support of our objectives to fabricate micro-SOFC structures capable of operation at reduced temperatures and to provide nano- and micro-structures offering the opportunity to investigate transport and electrode processes under idealized conditions, thin film electrolytes and electrodes have been grown by physical vapor methods and structured with the aid of photolithographic techniques. The use of microelectrodes, with well defined areas and triple phase boundary lengths, has allowed for a clear distinction to be made between electrodes for which all reactions are localized to the triple phase boundary and for those for which the full electrode area is active. Materials being investigated are YSZ and CGO solid electrolytes and Pt and LSCO electrodes. A particularly unexpected and exciting result has been the critical role played by the YSZ film processing temperature on the YSZ/Pt electrode interface impedance. Low temperature processing of YSZ appears to lead to orders of magnitude reduction in electrode impedance. Further improvements have been achieved by fabricating Pt-YSZ nanocomposites, which clearly exhibit mixed ionic-electronic conduction character. Additional progress is being made in introducing porosity in a highly controlled manner into such electrodes. Finally, a novel microprobe station has come on board, which allows us to study the performance of the microstructured electrodes under controlled temperature and atmosphere.

### 8.1 Greatly Enhanced Platinum Electrode Performance on Thin Film YSZ

The first microfabrication approach used dense platinum thin film electrodes with well controlled geometries on the surface of bulk YSZ standards and thin films. Sputter deposition was used to produce the dense YSZ thin films. These samples were electrically characterized using impedance spectroscopy to determine not only the electrolyte conductivity but also the triple phase boundary length-specific electrode activation polarization resistance (see Figure 53).

YSZ films of composition  $Y_{0.09}Zr_{0.91}O_{2-x}$  were found to have an enhanced ionic conductivity by as much as a factor of 20-30. These results, illustrated in Figure 54, are believed to be due to nanometric grain sizes creating metastable cubic morphology and leading to reduced defect interactions. All of the films were found to have significantly reduced grain boundary resistance compared to the bulk polycrystalline sample. This was believed to be due to very low impurity content of the film grain boundaries. In all cases, the electrolytic resistance of a thin film electrolyte is expected to be insignificant compared to the electrode polarization resistances in a SOFC.

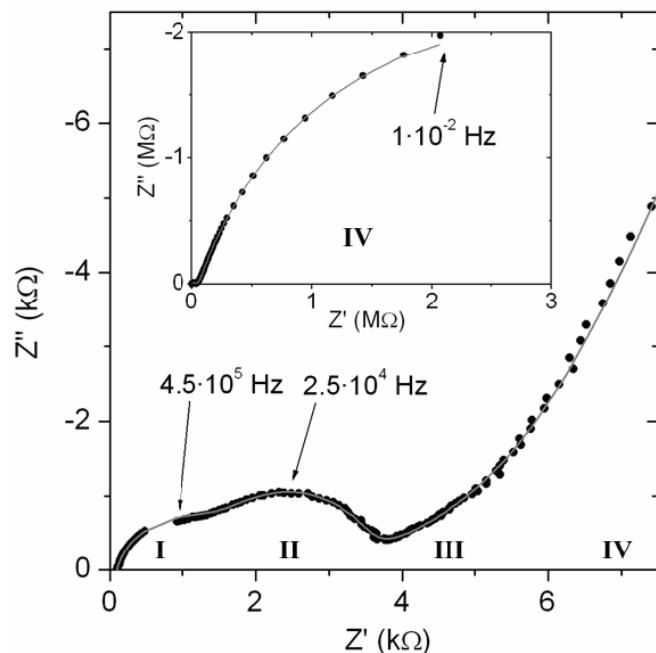


Figure 53: A typical impedance spectrum for a thin film YSZ deposited on a silica substrate. Points are raw data, line is the fit from the equivalent circuit. The main portion of the graph displays the high frequency portion of the spectrum while the inset shows the complete spectrum (note the change in units). The frequency at selected point is given. (Key: I bulk electrolyte; II electrolyte grain boundary; III constriction resistance; IV electrode)

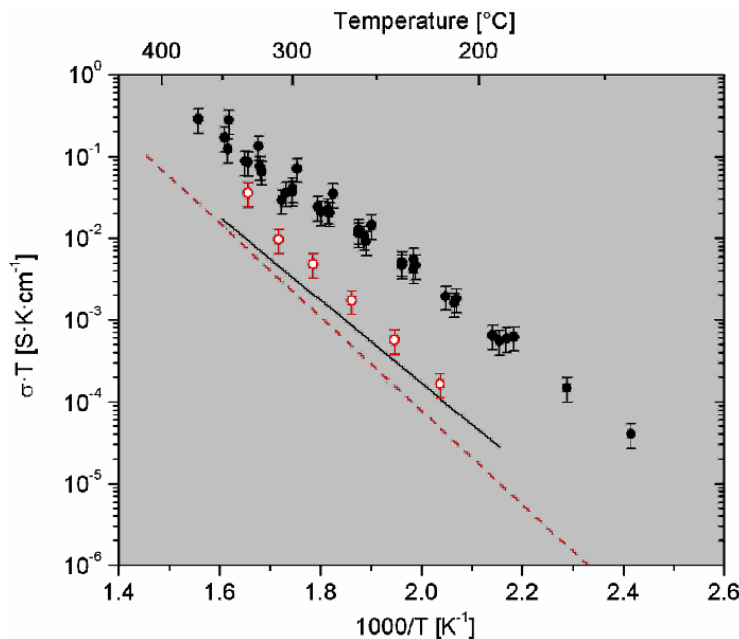


Figure 54: Arrhenius plot of YSZ grain conductivity, comparing compositions of roughly  $\text{Y}_{0.09}\text{Zr}_{0.91}\text{O}_{2-x}$  ( $\blacksquare$ , solid line) and  $\text{Y}_{0.16}\text{Zr}_{0.84}\text{O}_{2-x}$  ( $\color{red}\square$ , dashed line). Points are the values measured for films in this study deposited at  $600^\circ\text{C}$ ; lines are linear fits to data from literature.

A constriction resistance was found for all of the samples at low frequencies. This resistance was due to the very large electrode contacts compared to the triple phase boundary width. The dependence of the constriction resistance could be qualitatively understood from finite element

modeling. The amount of constriction was consistently larger than theoretically calculated, however. This is believed to indicate a 3-dimensional constriction, with only certain sites along the triple phase boundary being active for the exchange reaction.

Concerning the electrode polarization resistance, it was found that the electrodes placed on bulk standards and films deposited at high temperatures matched the best values from the literature. The resistance decreased further by a factor of up to 300 when the electrolyte surface was a film deposited at reduced temperature (see Figure 55). X-ray photoelectron spectroscopy revealed the cause of this to be silicon contamination on the surface of the electrolyte. In this study, the source of the silicon was a chemical used in the photolithographic processing of the platinum electrodes, but silicon contamination on the surface of YSZ electrolytes is a known and common phenomenon after high temperature sintering of the ceramic. These measurements are possibly the first electrochemical characterization of nearly silicon-free YSZ surfaces.

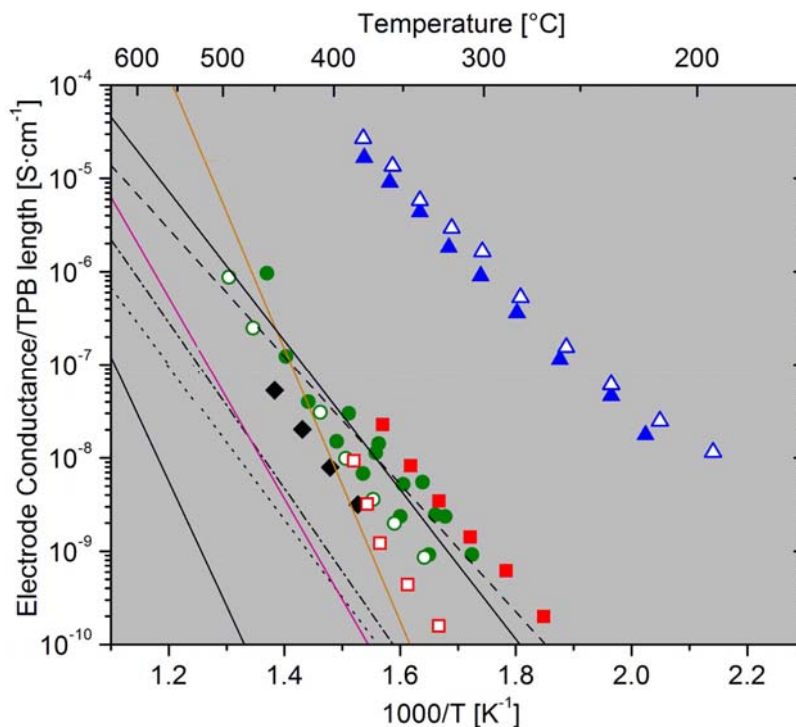


Figure 55: The low frequency (electrode polarization) conductance normalized by the TPB length for the tape-cast YSZ (◆), untreated single crystal (●,○), single crystal with 100 nm of a 600°C-deposited YSZ film (■,□), and single crystal with 100 nm of an unheated deposited YSZ film (▲,△). Closed symbols represent (100)-oriented YSZ single crystal substrates while open symbols represent (111)-oriented single crystal substrates. The lines are extrapolations from literature.

The rate limiting step in the electrode reaction is believed to be the exchange of adsorbed oxygen on the platinum surface with an oxygen vacancy on the YSZ surface. This determination was based upon the activation energy and  $pO_2$  dependence of the electrode polarization resistance and the shape of the impedance curve. Diffusion of adsorbed oxygen on the Pt surface is another possibility for the rate limiting step. Electrochemically active sites are believed to be non-uniformly present on the YSZ surface. Rather, they are believed to occur at surface defects

such as ledges, kinks, etc. This explains the larger than expected constriction resistance and the decrease in electrode polarization resistance following the etching-induced roughening of a single crystal surface.

Given the critical role played by the YSZ thin film electrolyte in the YSZ/Pt interface, special efforts were made to characterize the YSZ films in as detailed manner as possible. YSZ films, 100-1000 nm thick, were produced by sputter deposition of metal alloy targets in an oxygen-rich environment. The substrates were fused silica, and were held at 20, 300 or 600°C during deposition. XPS analysis indicated that the Zr – Y ratios in the films match those of the target material for films made from both 9% and 16% Y targets. X-ray diffraction patterns of the films show considerable peak broadening, likely due to both strain and reduced grain size. After accounting for the strain, the peak broadening gives grain size estimates of ~13 nm in films deposited at room temperature and ~50 nm in films deposited at 600°C. Atomic force microscopy of the film surfaces indicates similar grain sizes. Only cubic X-ray diffraction peaks were observed, however the presence of tetragonal phase could not be entirely dismissed, since peak broadening may conceal tetragonal phase peak splitting.

The second microfabrication method used was reactive co-sputtering to produce composite Pt-YSZ thin films with a bi-continuous network morphology and grain sizes on the order of 30 nm. Such intimate mixing of the electronic and ionic conducting phases created an effective mixed ionic-electronic conductor with the entire surface of the film electrochemically active to the electrode reaction. The composition of the films, in terms of Pt to YSZ ratio, was successfully controlled by adjusting the sputtering powers used on the targets. The best processing conditions resulted in electrodes with an area specific polarization resistance less than  $500 \Omega \cdot \text{cm}^2$  at 400°C and, by extrapolation,  $10 \Omega \cdot \text{cm}^2$  at 511°C and  $1 \Omega \cdot \text{cm}^2$  at 608°C. The figure below, Figure 56, compares the conductance of such films against other mixed conductors and non-mixed conductors, limited in their performance by triple phase boundary length.

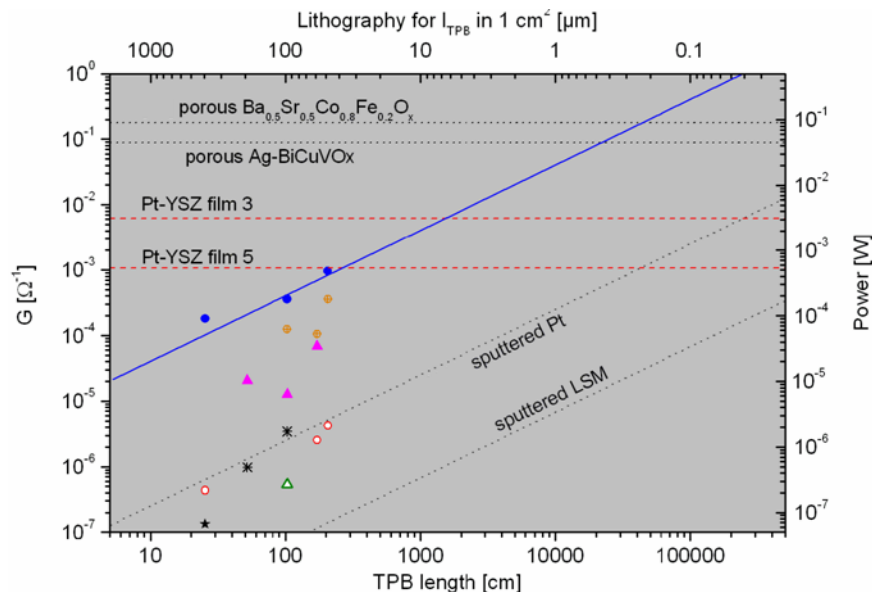


Figure 56: The electrode activation polarization conductance at 400°C, including the Pt-YSZ composite films. Note, the Pt-YSZ films, being composite mixed ionic conductors, are active across their full area rather than being limited to the triple phase boundary (TPB) length like Pt or LSM.



The combination of Pt-YSZ electrode films and YSZ electrolyte films are particularly attractive for the fabrication of thin film stacks and given their relatively high conductance may enable operation of a micro-solid oxide fuel cell at intermediate temperatures (400-500°C). An example of perhaps the thinnest SOFC stack so far fabricated is shown below in Figure 57.

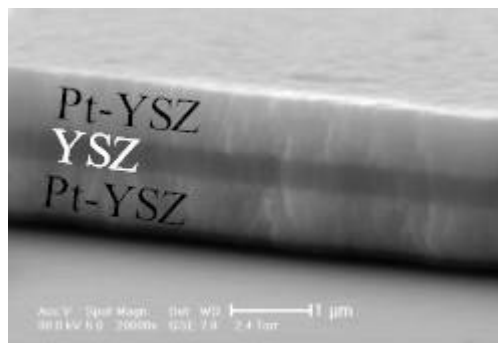


Figure 57: Symmetric thin-film stack of Pt-YSZ, YSZ and Pt-YSZ deposited as a prototype  $\mu$ -SOFC device

## 8.2 Materials and Structural Analysis for Micro SOFC

The core of the micro-solid oxide fuel cell is a multilayered freestanding membrane structure consisting of electrolyte, electrodes and likely some supporting structure. Reliability of the freestanding membrane can be assured by avoiding mechanical instability and/or fracture due to very high intrinsic and thermal stresses during both processing and operation. The intrinsic/residual stress state is controlled by specific deposition conditions. Resulting residual stresses are large and directly affect structural integrity. As the electrical power output from the fuel cell is dependent on the elevated thermal state of the electrolyte and electrode materials, these thermal stresses also play a key role in defining the mechanical integrity of the structure. In order to guide material and process development and provide input to the overall system design, a modeling framework is required to analyze the trades between geometrical, material, and functional parameters. In addition, detailed characterization must be performed on micro-fabricated SOFC materials to provide input to the device design and system modeling. Thus, efforts described in this section have been conducted in close collaboration with the materials development, micro-fabrication process development, and system design and modeling efforts described elsewhere in the report.

## 8.3 Residual Stress and Microstructural Characterization of YSZ Material

Previous work on the development of free-standing membranes has established the need for detailed knowledge of the residual stress present in  $\mu$ SOFC materials. Focusing on the YSZ electrolyte material deposited via RF reactive sputtering, the residual stress state of films deposited at room temperature varies significantly with film thickness, working pressure and substrate temperature. Recent work has focused on identifying and verifying stress generation mechanisms, considering films deposited at high temperature, as well as capturing the origins of observed changes in stress state with post-deposition thermal cycles.

The as-deposited total residual stress present in YSZ films ranging from 5nm – 1 $\mu$ m thickness for both room temperature and high temperature depositions are presented in Figure 58. Two series of room temperature depositions done at different periods of time separated by

several months indicate an overall decrease in compressive stress that is likely due to changes in bombardment energetics that can be attributed to target wear. Overall, stress levels are very high and range over 1.5 GPa. Variations of stress with thickness are generally correlated to grain formation and growth (see Figure 58). Such grain evolution typically generates tensile film stress.

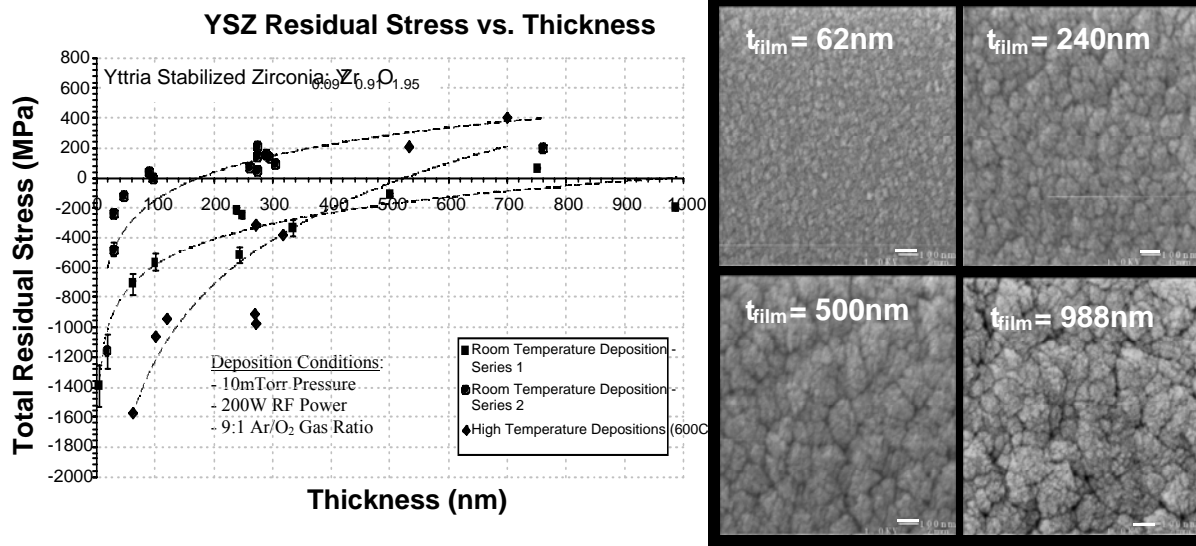


Figure 58: (left) YSZ residual stress vs. thickness - trend lines have been shown to clearly distinguish datasets, and (right) planar high-resolution SEM images of sputtered YSZ films of varying thickness. Scale bars are 100nm in length. Images indicate grain growth typically correlated with development of tensile stress in films.

In addition to thickness variations, deposition pressure and substrate temperature can be used to “tune” (by over 1 GPa) the stress present in sputtered YSZ films. Experiments have recently more fully determined these trends empirically and identified fundamental mechanisms (*e.g.*, atomic peening/forward sputtering, whereby high bombardment energy at low sputtering pressure causes a combination of sputtering gas atoms and film surface atoms to be driven into the film and occupy interstitial sites causing compressive stress).

#### 8.4 Evolution of Residual Stress with Thermal Cycling of YSZ and Trilayer Stack

In addition to the as deposited residual stress state, it is important to know how the residual stress of  $\mu$ SOFC materials evolves with post-deposition thermal cycles. Such evolution has important implications for device fabrication routes where subsequent high temperature processes may be needed, and ultimately for device performance where the startup and cool down cycles of a  $\mu$ SOFC will impact structural integrity. Total residual stress as a function of post-deposition temperature for room and high-temperature deposited films are shown in Figure 59. Both films initially exhibit increased compressive stress due to CTE mismatch. However, room temperature deposited films exhibit a severe shift in stress state at approximately 200C that ultimately results in a tensile stress state in the film when brought back to room temperature. A less pronounced shift is seen in high temperature deposited films. In both films, subsequent cycles exhibit the linear stress variation due to CTE mismatch, following the slope of the cooling portion of the

first cycle. It is currently believed that the observed hysteresis is due to reduction of the lattice distortion caused by the aforementioned atomic peening process, rather than by release of implanted Ar gas as originally hypothesized. That is, interstitial film atoms, rather than implanted gasses, diffuse and align to standard sites in the crystal lattice with post-deposition annealing, eliminating the overall compressive stress in the film. Similar characterization has been completed for representative fuel cell structures. Typical results of a characteristic first thermal cycle after deposition are shown in Figure 59. These results indicate a likelihood of plastic deformation/yielding in combination with the tensile stress generation mechanisms observed for YSZ films.

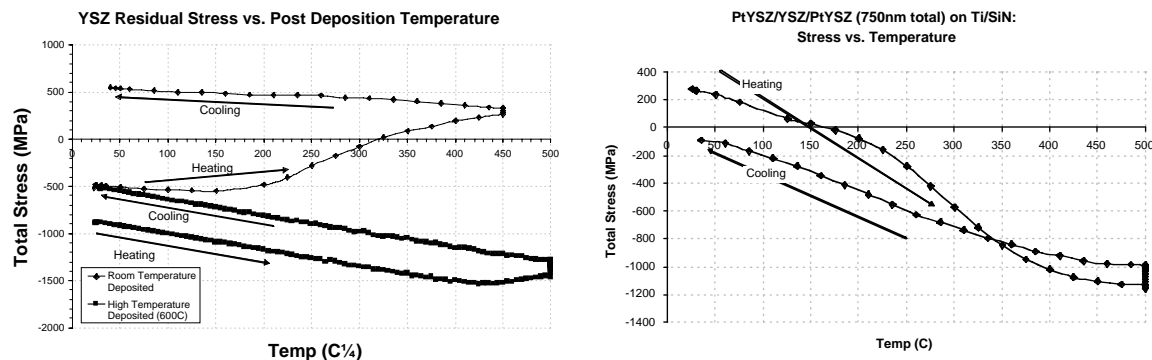


Figure 59: Residual stress evolutions with post-deposition thermal cycling: (left) behavior for room- and high-temperature deposited YSZ films, and (right) behavior of fuel cell stack of Pt-YSZ/YSZ/Pt-YSZ deposited on Si with Ti/SiN adhesion/mask layers.

## 8.5 Elastic Property Characterization of Thin Film YSZ

Young's modulus and coefficient of thermal expansion (CTE) were experimentally obtained with several mechanical tests for thin-film nanostructured YSZ. These two material properties are critical in designing thermomechanically stable fuel cells. Young's moduli of YSZ were acquired in two different directions. The out-of-plane stiffness was measured by nanoindentation using three-sided pyramid tips indented square samples (~1-2  $\mu\text{m}$  thick YSZ layers deposited on silicon substrates). The indentation depth and the load were recorded to extract Young's modulus assuming Poisson's ratio of 0.31. The in-plane stiffness was measured by center height measurement of buckled square membranes. Thin YSZ films with thickness of ~350-650nm were released into squares (~100-200  $\mu\text{m}$  sidelength). When these membranes with small compressive stresses buckle in the first mode, Young's moduli can be extracted from their center heights, using stiffness-height curve fitted from a nonlinear energy minimization analysis. CTEs were calculated by wafer curvature measurement of unreleased films deposited on silicon substrates during post-deposition thermal cycling.

The out-of-plane stiffness of YSZ measured by nanoindentation varied from ~220 to ~280GPa as shown in Figure 60 left, which is equal or above bulk values. On the other hand, the in-plane stiffness depended strongly on films' fabrication conditions (~24-105GPa, as shown in Figure 60 right), since the deposition conditions, such as temperature and substrate, influence on the films' crystalline orientation as confirmed by XRD. The in-plane stiffness values are significantly lower than the bulk, and the difference is attributed to the film's mixed microstructure that consists of amorphous regions threading through the textured crystal grains.

The obtained CTEs were relatively constant as  $9.8$  to  $11.4 \times 10^{-6} / ^\circ\text{C}$  regardless of deposition conditions, very near the bulk values. The important findings from these experiments are that the mechanical properties of thin films significantly vary from the bulk, and thus that characterization specific to structure and fabrication method is necessary.

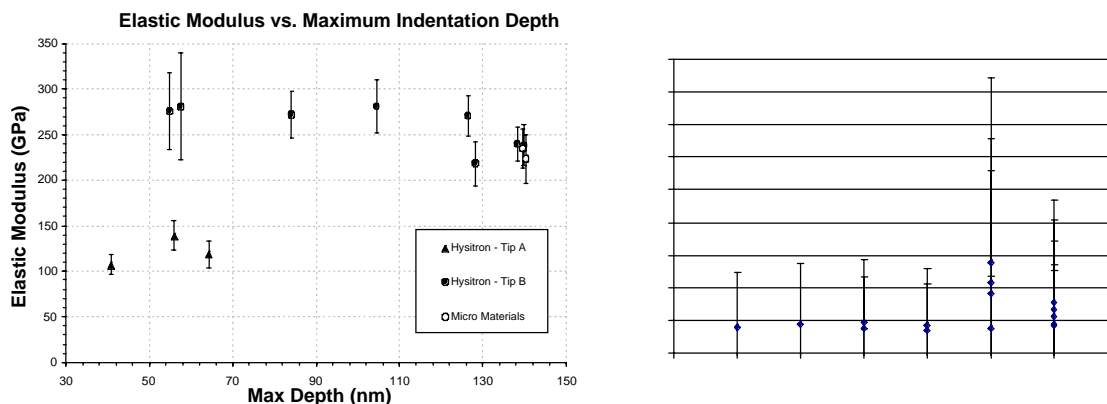


Figure 60: Measured Young's modulus of thin-film YSZ: (*left*) out-of-plane modulus from nanoindentation, and (*right*) in-plane modulus from center height measurement of buckled square membranes. Films are deposited at room temperature.

## 8.6 Structural and Electrochemical Characterization of Two Proton Conducting Oxide Thin Films

In the bulk form, barium and strontium cerate (perovskites) are known to be electrolytically conductive at lower temperatures (perhaps  $200^\circ\text{C}$  lower) than YSZ. The use of proton conducting oxide materials as an electrolyte offers the potential to reduce the operating temperature of the solid oxide fuel cell (SOFC), leading to improved thermal management and material compatibility. However, many proton conducting materials have not yet been investigated for residual stress and electrochemical properties in thin film form. Here, the thermomechanical and electrochemical properties of two promising materials: Yttria doped Barium Cerate ( $\text{BaCe}_{0.9}\text{Y}_{0.1}\text{O}$ ) and Terbium doped Strontium Cerate ( $\text{SrCe}_{0.95}\text{TbY}_{0.05}\text{O}$ ), for use in a microfabricated SOFC ( $\mu\text{SOFC}$ ).

Due to the lower dopant composition in the films, e-beam deposition did not prove to be a viable processing route. As a result, sputtering has been undertaken for both barium and strontium cerate. Uniform, crack-free thin films of both compositions were produced by sputter deposition. Films with thickness ranging from  $150$  nm to  $600$  nm were deposited on a fused silica substrate. The desired composition was achieved for both films at a deposition temperature of  $575^\circ\text{C}$ , though minor secondary phases were also present. Residual stress for different film thicknesses was measured as a function of temperature using the wafer curvature technique. All films exhibited an initial compressive residual stress (from  $-200$  to  $-600$  MPa) and a significant tensile stress hysteresis upon thermal cycling, leaving a final residual stress at room temperature that ranged from  $-200$  to  $+200$  MPa (e.g., see Figure 616161 left). The average modulus-CTE product for films of each material was found to be  $\sim -0.65$  MPa/ $^\circ\text{C}$ , which is 3-4 times smaller than that of the bulk materials.

Electrochemical performance was assessed using impedance spectroscopy. Measurements were taken in three gas atmospheres (ambient air, dry air, and 5%  $\text{H}_2 + 95\% \text{Ar}$ ) from 200 to 500°C. Bulk conductivity in air was found to be  $6.57 \times 10^{-4} \text{ S/cm}$  at 473°C for BaCeYO and  $2.64 \times 10^{-4} \text{ S/cm}$  at 424°C for SrCeTbO. Though somewhat lower, these values compare well with the conductivity for bulk YSZ (see Figure 61 right), the most common SOFC electrolyte:  $\sim 1 \times 10^{-3} \text{ S/cm}$  at 500°C. Prior research indicates that conductivity and activation energy are a strong function of the quantity of water vapor in the test atmosphere. The lack of water vapor in this work most likely explains the lower conductivity and higher activation energy. The activation energy in ambient air was 0.7 eV for BaCeYO and 1.0 eV for SrCeTbO, suggesting that these materials should have comparable or better conductivity at lower temperatures than bulk YSZ which has a value of 0.8 eV. These proton conducting oxides are viable and promising materials for lowering the temperature of a  $\mu\text{SOFC}$ . Future work on these films should include electrochemical tests in a controlled, humidified atmosphere and performance tests of these materials in a  $\mu\text{SOFC}$ .

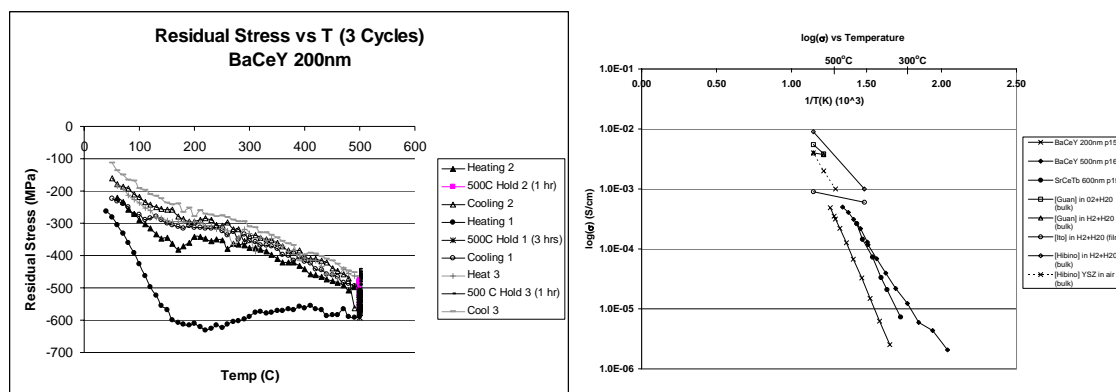


Figure 61: Proton conducting thin film residual stress and electrochemical characterization results: (*left*) residual stress vs. temperature for a 200nm thick BaCeYO film, and (*right*) conductivity vs. temperature for BaCeYO and SrCeTbO shown with results from prior work. Prior work is for BaCeYO unless otherwise noted.

## 8.7 Development of Large Free-Standing Electrolyte-supported Micro Fuel Cell Membranes

Expansion of the original design space has been undertaken by analyzing a low-stress postbuckled operating regime. 500 nanometer thickness YSZ films deposited on released SiN membranes at 600°C were able to survive thermal cycles from room temperature to 600°C without cracking (100% survival - all 56 membranes survived, with side lengths of  $\sim 200$  microns). One of these membranes is shown in Figure 62 left. More recent studies on Pt-YSZ/YSZ/Pt-YSZ fuel cell membranes demonstrated survival of 25 (out of 25) membranes up to 130 micron side length (see Figure 62 right). In both studies, the out-of-plane deflections of the buckled membranes were large (multiple membrane thicknesses), well into a geometrically nonlinear post-buckling regime, the analysis of which is presented next.

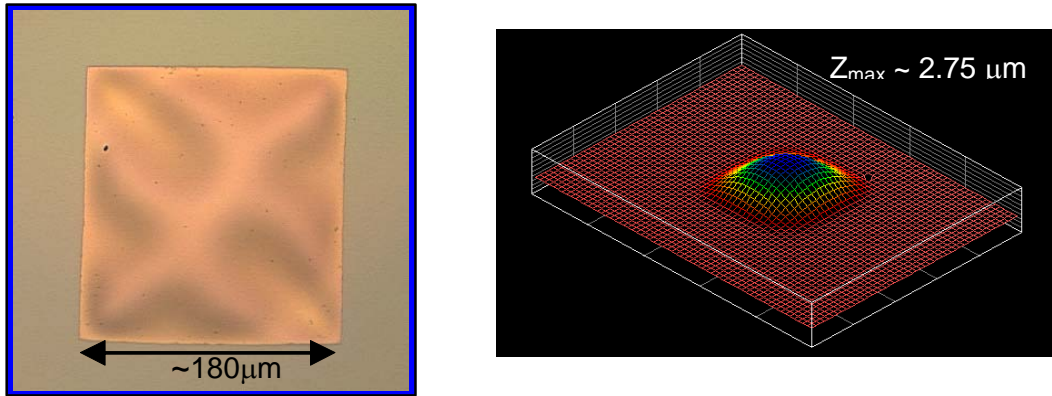


Figure 62: (left) Optical microscope image of buckled YSZ/SiN membrane, and (right) interferometric image of buckled Pt-YSZ/YSZ/Pt-YSZ fuel cell membrane ( $\sim 130\mu\text{m}$  side length).

YSZ membrane fabrication suggests expanding the existing design space by allowing for post-buckled membranes. Large out-of-plane post-buckled deflections of such membranes ( $\sim 9\times$  membrane thickness) indicate significant geometrically nonlinear deformation. An analytical and numerical modeling framework has been developed to model the buckling/bending behavior of membranes under compression (due to residual and thermal stresses). The framework and models will be used both to understand stresses during failure and in mechanical property testing. Preliminary modeling results (the full Pt-YSZ/YSZ/Pt-YSZ trilayer fuel cell stack is modeled) suggest three regions of structural behavior at elevated temperature, corresponding to small, medium, and large square membranes (see Figure 63). Small membranes do not buckle, and are in a state of equibiaxial compressive stress. Medium membranes buckle and bend, resulting in high compressive and tensile stresses. Large membranes also buckle and bend, but the resulting compressive and tensile stresses are lower. Fabrication/testing of membranes has been completed (see Figure 64) to correlate with the analysis results using experimentally determined properties for the tin film materials (discussed earlier) when available.

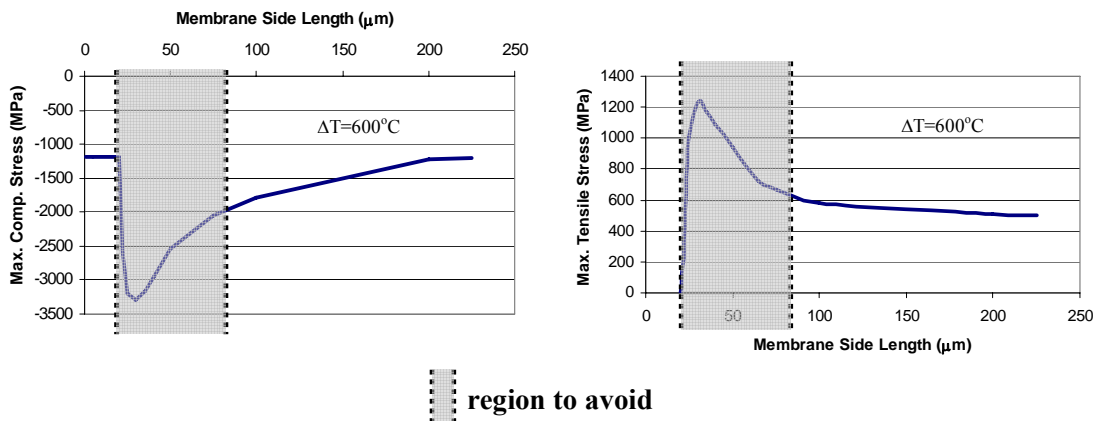


Figure 63: Maximum stresses in a Pt-YSZ/YSZ/Pt-YSZ buckled trilayer stack as a function of square membrane sidelength for  $\Delta T=600^\circ\text{C}$ : (left) compressive and (right) tensile stress regions. The current analysis does not yet include residual stress.

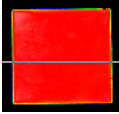
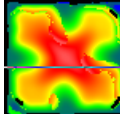
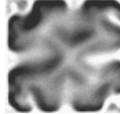
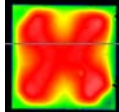
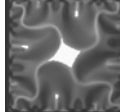
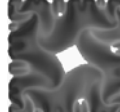
Size	Before annealing	After 1 <sup>st</sup> anneal to 625°C	After 2 <sup>nd</sup> anneal to 625°C
Trilayer (80μm)	Flat 	1st buckling 	1st buckling 
Trilayer (180μm)	1st buckling 	2 <sup>nd</sup> buckling 	2 <sup>nd</sup> buckling 

Figure 64: Observed postbuckled and uncracked Pt-YSZ/YSZ/Pt-YSZ samples for nonlinear analysis validation. Unfailed membranes demonstrates fabrication of viable large, ultra-thin fuel cell membranes.

## 8.8 Fabrication and Testing of Electrolyte-supported Ultra-thin Film Fuel Cells

Fuel cell tri-layer stacks of YSZ electrolyte sandwiched between a Pt-YSZ cathode and anode were designed to be thermally stable at high operation temperature ( $\sim 600^\circ\text{C}$ ). The configuration is shown in Figure 65. With material properties of films deposited under appropriate conditions, in-plane stresses were estimated with nonlinear plate theory as mentioned above. Avoiding the high stress region, fuel cell stacks were designed for operation in the post-buckling regime, with a total thickness of  $\sim 450$  or  $\sim 750$  nm and sidelength of  $\sim 100$  or  $\sim 200$   $\mu\text{m}$ . Fabrication of the tri-layer included additional layers (adhesion layers, electrode layers) and appropriate patterning to avoid shortage between cathode and anode. The tri-layers with total thickness of 450nm successfully survived two thermal cycles up to  $625^\circ\text{C}$ , while the tri-layers with total thickness of 750nm cracked after the first annealing cycle to  $625^\circ\text{C}$ . This result validated the post-buckling design regime, and the stress relieving trend with decreased thickness.

The basic power test design was based on the traditional button cell-type design, with the exception that both electrical contacts were made on the top-side to avoid possible sealing problems with the introduction of wires on the bottom-side of the  $\mu\text{-SOFC}$  specimen. The complete reactor consisted of a furnace, custom-made quartz and mullite reactor tubes to ensure better thermal match with silicon test dies, mass flow controllers, piping, a GC with TCD detector and a Solartron® electrochemical interface (see Figure 66). Three layers of tubes on the bottom were utilized to accurately control the atmosphere for the anode. The gas control on the cathode side was achieved through two layers of tubes with an outer quartz tube. GC was used to analyze the outlet gas from the anode side to monitor the seal and oxygen permeation through the membranes. A Macor® was precisely machined to slip onto the top of the  $\mu\text{-SOFC}$  die. With the alignment achieved through the outer quartz tube, gold contact meshes attached to Macor® with gold paint could be aligned with the appropriate positive and negative current collector pads on the testing die (see Figure 66). The gold contact wires were drawn out of the top of the furnace using 4-hole ceramic rod and connected to the Macor® through additional wires attached to the gold meshes. Good contact was ensured by the weight of the Macor® and the force from the top fittings. Two wires for each electrode were used to further demonstrate the test reliability. In the center of the Macor®, a bored hole was used to ensure gas access to the cathode side of the  $\mu\text{-SOFC}$  (see Figure 66). The membrane-based silicon SOFC device was sealed on top of the mullite tube by silica-based cement. The seal could survive thermal cycles up to  $650^\circ\text{C}$  with no or negligible leaking.



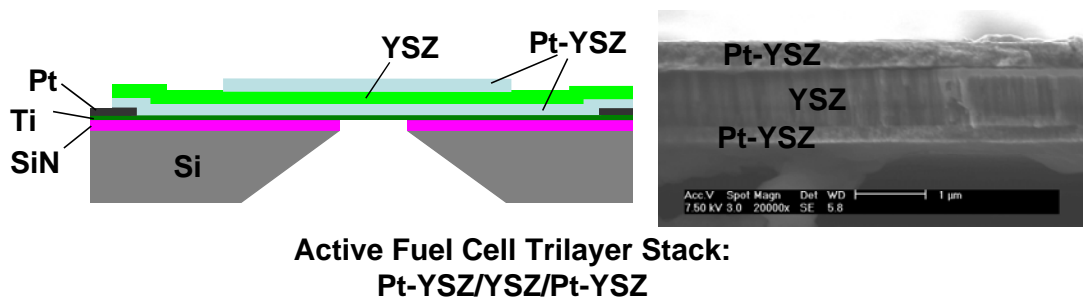


Figure 65: Fuel cell device structure: (left) illustration of electrolyte-supported 2-sided fuel cell, and (right) cross-sectional SEM of a tri-layer fuel cell stack.

The 450 nm thick device was tested between 350°C and 500°C with a flow of 30 ml/min of 5% H<sub>2</sub> in He on the anode side; the cathode side was open to air. Data were collected only after the signal stabilized at the pre-set temperature. Voltage and power output for a preliminary device test are shown in Figure 67. Power output of  $\sim 0.1 \text{ mW/cm}^2$  was significantly lower than the estimated values ( $\sim 0.25 \text{ W/cm}^2$ ) based on electrochemical results. This low power output was possibly due to known setup issues including gas/electric leakage, shortage of gases, or other set-up and sample issues. The power curves clearly demonstrate operation of the fuel cell. Further improvements on the test fixture such as electrical connection and gas sealing/flow are needed.

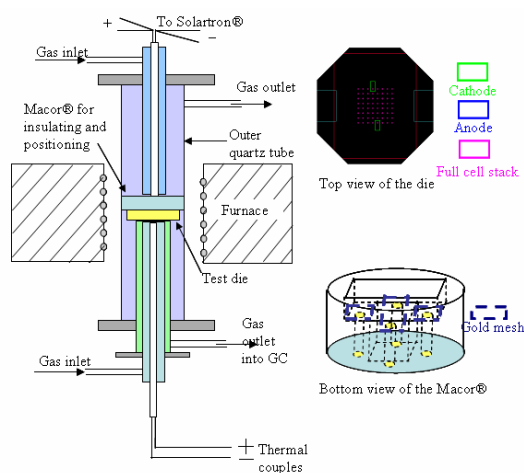


Figure 66: Test reactor for  $\mu$ SOFC testing

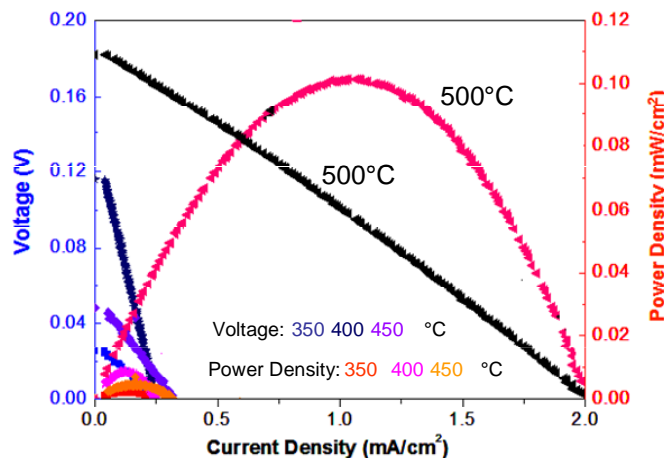


Figure 67: Preliminary power test results: 450nm thick Pt-YSZ/YSZ/Pt-YSZ electrolyte-supported fuel cell power curves.

## 8.9 Girder-Grid Support Structure Design and Fabrication

Early mechanical analysis of thin film stability analysis suggested that membranes comprised of the free-standing fuel cell stack must be no larger than  $\sim 1 - 10$  micron to avoid buckling and



fracture during temperature cycling and/or high temperature operation. Therefore, we also explored an alternative architecture employing a girder-reinforced membrane capable of providing mechanical support without deformation under the stresses resulting from an operating temperature range of more than 600°C while still maximizing the exposed surface area of the fuel cell stack for electrochemical reaction.

The free-standing membrane was comprised of a system of 2 x 10 micron silicon nitride girders, reinforced with single-crystal silicon. The girders were spaced such that they enclose an array of 1 – 5 micron square free-standing membranes, as illustrated in Figure 68. Silicon sidewall coverage results from anisotropic KOH etching; overetching in KOH can be employed to remove silicon entirely for reduced thermal mass at the expense of reduced mechanical strength. The fabrication process is detailed in Figure 69.

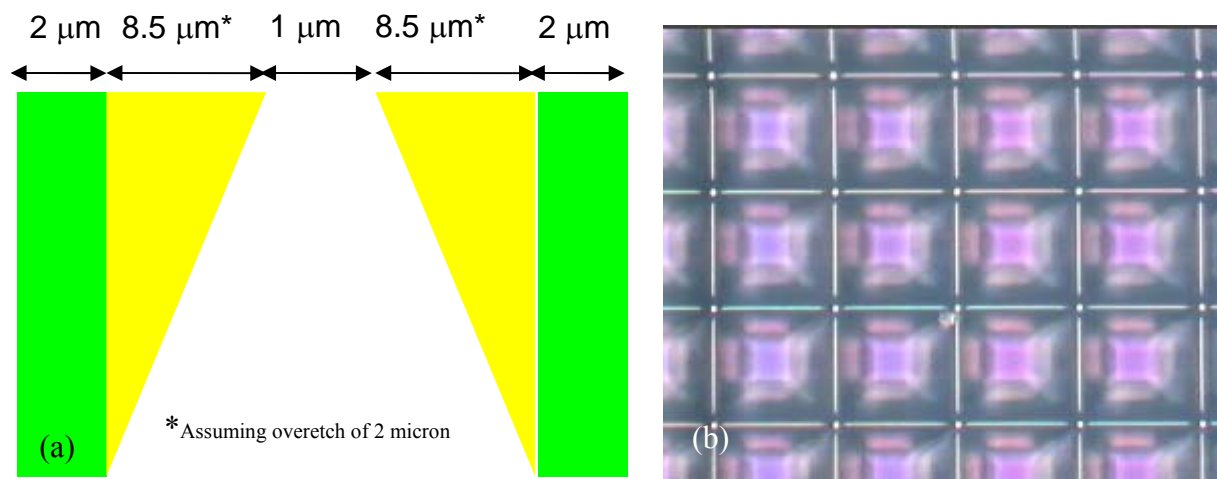


Figure 68: Girder-reinforced membranes; (a) schematic of one free-standing membrane unit, and (b) optical microscopy image of girder-reinforced system of free-standing membranes.

The first challenge of fabrication was ensuring that the silicon nitride completely filled the girder molds. In order to achieve a uniform, unbroken oxide film via sputtering, the surface for deposition had to be free of cracks or gaps. Incomplete filling of the girder molds thus prevented the deposition of a uniform circuit over the support network, as illustrated in Figure 70. The incompletely filled girders were a result of feature blow-out incurred during photolithography, producing molds that were roughly twice the target width. Subsequent devices were fabricated taking additional steps to ensure girder mold dimensions were maintained during mask patterning and image transfer during photolithography. The resulting completely filled silicon nitride girders are shown in Figure 70b.

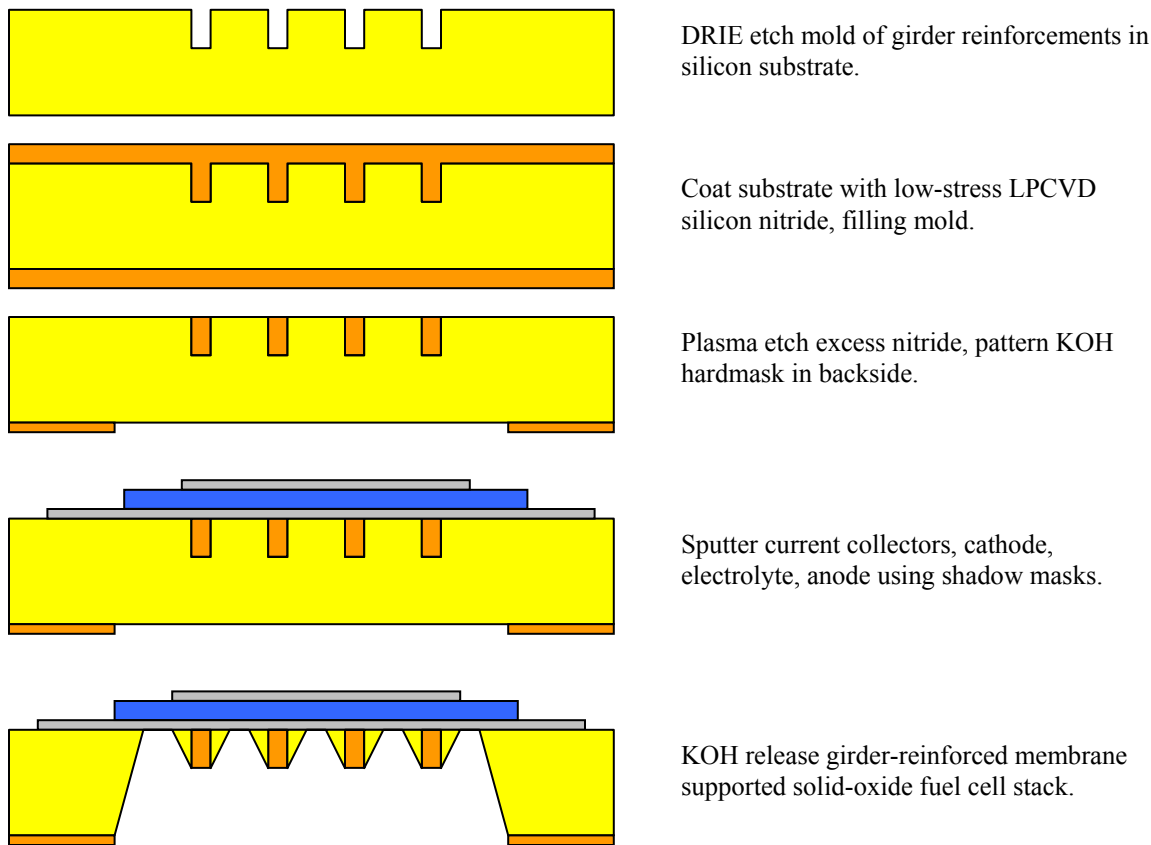


Figure 69: Illustration of Fabrication Process for Girder-Reinforced Membrane Supported-Fuel Cell.

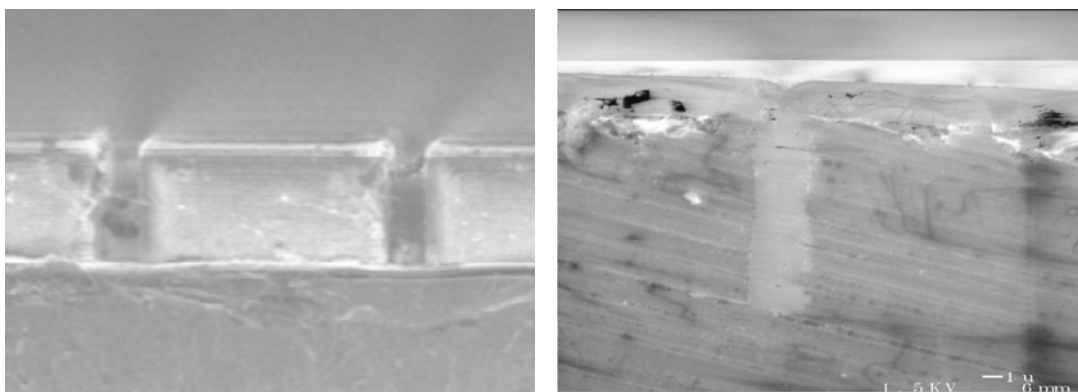


Figure 70: SEM cross-section images of (a) incompletely-filled girder mold, and (b) fully-formed silicon nitride girder in silicon mold. Note the large (3-4 micron, 10 micron deep) gaps resulting from incompletely filled girders.

In addition to fabricating the girder-support system, progress was made in the deposition of the fuel cell stack onto the support network. The design employed a YSZ electrolyte, and co-sputtered platinum and YSZ electrodes. All three layers were deposited via sputtering. While the surface of the girders have a characteristic ‘divot’, approximately 200 – 500 nm in depth, cross-section SEM imaging of a complete fuel cell stack deposited over the surface of the girders

(Figure 71) indicate that these fluctuations are not large enough to crack or split the fuel cell stack.

A series of shadow masks are employed to deposit first the fuel cell stack (employing a 20nm thick titanium adhesion layer), followed by platinum contact pads for ease of making external electrical connections. A top-down schematic of the thin-film fuel cell layout is shown in Figure 72, below. The resulting prototype device is pictured in Figure 73. Further work is planned for releasing the fuel cell stack, thermal cycling and mechanical testing of the supported stack, and electrochemical testing of the prototype device.

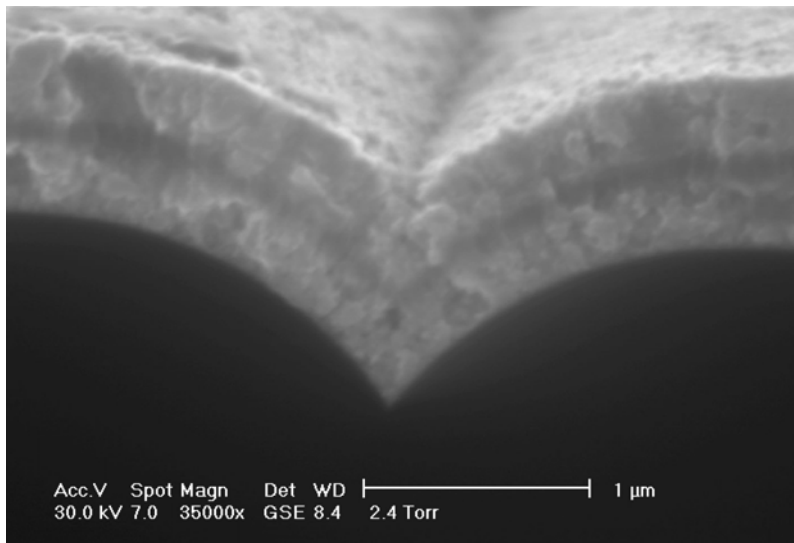


Figure 71: Cross-section ESEM image of fuel cell stack deposited upon girder support structure.

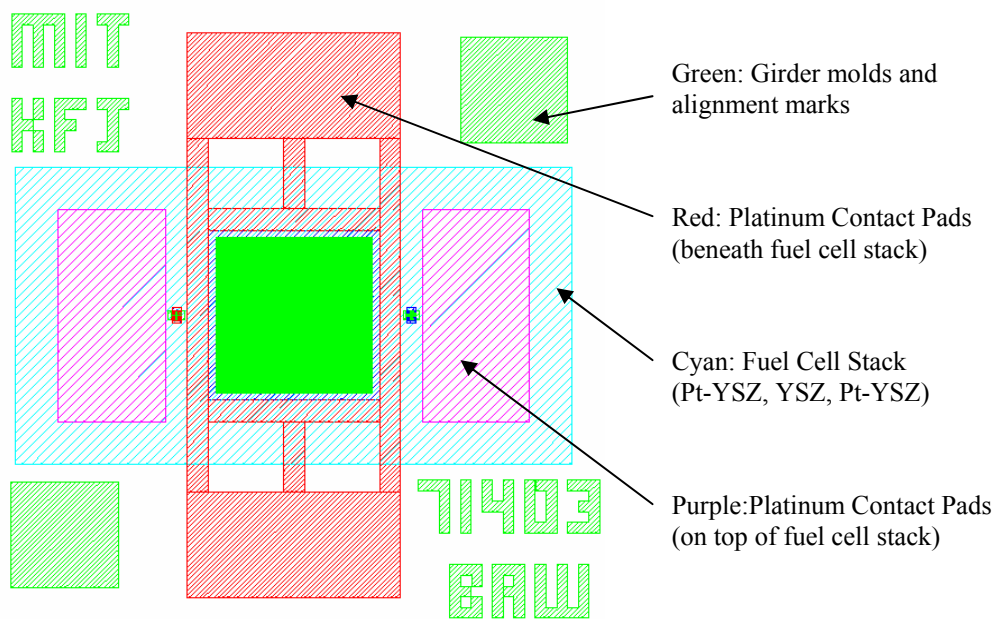


Figure 72: Top-Down view of four mask layers comprising the girder-grid supported solid-oxide fuel cell design.

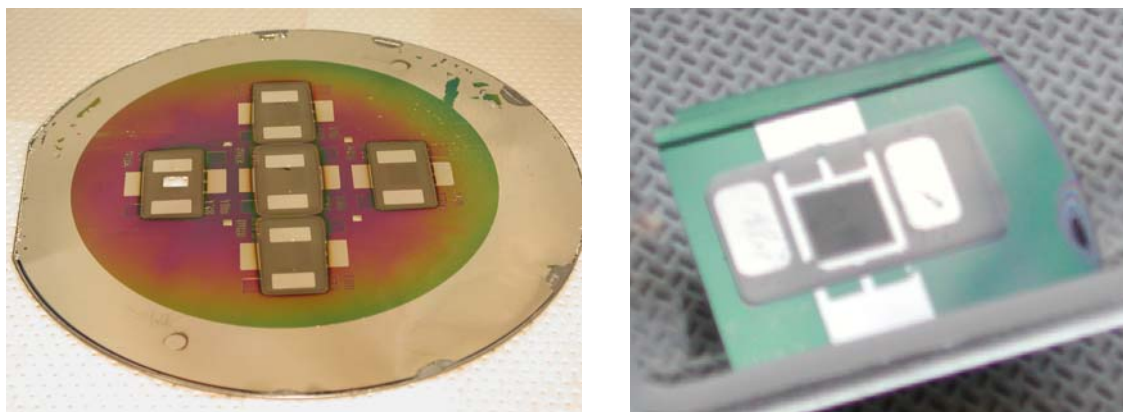


Figure 73: Pictures of completed prototype girder-grid fuel cell wafer and individual chip.

## 9 Recommendations

Realization of microreactor based portable energy conversion system has to involve thermally efficient, integrated reformer and fuel cell systems. SOFC technology will have better energy efficiency than PEM systems, but also require significant advances in materials and sealing technology. In general, realization of high energy efficient (>30%) reforming based systems will demand significant new understanding of thermal management solutions, thermophysical properties of mixed materials systems, and integration techniques for power systems. These results would represent significant scientific and engineering contributions and would have broad technological impact.

Specific areas of research needs are:

- New understanding, systems engineering, and materials expertise to create integrated, high efficiency fuel reformer – fuel cell systems.
- Understanding of design rules and materials properties allowing the design of highly integrated and thermally efficient systems.
- Advances in fundamental electrocatalysis resulting in moderate temperature direct conversion hydrocarbon based fuel cells.
- Fundamental advances in catalysis and interfacial science enabling the realization of new chemical to electric energy schemes

## 10 References

- <sup>1</sup> Holladay, J.D, E.O. Jones, R.A. Dagle, G.G. Xia, C. Cao and Y. Wang. High Efficiency and Low Carbon Monoxide Micro-Scale Methanol Processors. *J. Power Sources*, **2004**, 131, 69.

- <sup>2</sup> Qi, Z., C. He and A. Kaufman. Effect of CO in the Anode Fuel on the Performance of PEM Fuel Cell Cathode. *J. Power Sources*, **2002**, 111, 239.
- <sup>3</sup> Liu, J., Barnett, S.A., *Solid State Ionics* **158**, 11 (2003).
- <sup>4</sup> Gorte, R.J., Vohs, J.M., *J. Catal.* **216**, 477 (2003).
- <sup>5</sup> Trimm, D.L., *Catal. Today* **49**, 3 (1999).
- <sup>6</sup> Ghosh, G., *Metall. Mater. Trans. A* **30A**, 1481 (1999).
- <sup>7</sup> Koide, H., Someya, Y., Yoshida, T., *Solid State Ionics* **132**, 253 (2000).
- <sup>8</sup> McIntosh, S., Vohs, J.M., Gorte, R.J., *J. Electrochem. Soc.* **150**, A470 (2003).
- <sup>9</sup> Wang, C., Worrell, W.L., Park, S., Vohs, J.M., Gorte, R.J., *J. Electrochem. Soc.* **148**, A864 (2001).

## 11 MURI Program Statistics

### 11.1 Publications

#### 11.1.1 Papers published in peer-reviewed journals

1. T. Stefanik and H.L. Tuller, "Ceria-Based Gaseous Sensors", *J. Euro. Ceram. Soc.*, **21**, 1967-1970 (2001).
2. P. Knauth and H.L. Tuller, "Solid State Ionics: Roots, Status and Future Prospects", *J. Am. Ceram. Soc.*, **85**, 1654-80 (2002). Invited
3. H. L. Tuller, "Defect Engineering: Design Tools for Solid State Electrochemical Devices", *Electrochimica Acta*, **48**, 2879-2887 (2003).
4. P. I. Barton and C. K. Lee, "Global Dynamic Optimization of Linear Time Varying Hybrid Systems", *Dynamics of Continuous Discrete and Impulsive Systems- Series B-Applications and Algorithms*, S: 153-158, (2003).
5. L.R. Arana, S.B. Schaevitz, A.J. Franz, Martin A. Schmidt, K. F. Jensen, "A microfabricated suspended-tube chemical reactor for thermally-efficient fuel processing," *J. MicroElectromechanical Systems* **12** 600-612 (2003)
6. H. L. Tuller, Integration of Solid State Ionics and Electronics: Sensors and Power Sources, *J. Ceramic Society Japan, Suppl.* 112-1, **112**, S1093-S1098 (2004). Invited review.
7. J. Lappalainen, D. Kek and H. L. Tuller, "High Carrier Density CeO<sub>2</sub> Dielectrics-Implications for MOS Devices", *J. Euro. Ceram. Soc.*, **24**, 1459-1462 (2004).
8. J. Fleig, H. L. Tuller, and J. Maier, "Electrodes and Electrolytes in Micro-SOFCs: A Discussion of Geometrical Constraints," *Solid State Ionics* **174**, 261-270 (2004).
9. C. D. Baertsch, K. F. Jensen, J. L. Hertz, H. L. Tuller, S. T. Vengallatore, S. M. Spearing, and M. A. Schmidt, "Fabrication and Structural Characterization of Self-Supporting Electrolyte Membranes for a Micro Solid-Oxide Fuel Cell," *J. Mat. Res.*, **19**, 2604-2615 (2004)
10. T. Stefanik and H. L. Tuller, "Nonstoichiometry and Defect Chemistry in Praseodymium-Cerium Oxide," *J. Electroceramics*, **13**, 775-778 (2004)
11. J. Lappalainen, H. L. Tuller and V. Lantto, "Electronic Conductivity and Dielectric Properties of Nanocrystalline CeO<sub>2</sub> Films," *J. Electroceramics*, **13**, 129-133 (2004).
12. J. L. Hertz and H. L. Tuller, "Electrochemical Characterization of Thin Films for a Micro-Solid Oxide Fuel Cell," *J. Electroceramics*, **13**, 663-668 (2004).
13. G. J. La O, J. Hertz, H. Tuller, Y. Shao-Horn, "Microstructural Features of RF-sputtered SOFC Anode and Electrolyte Materials", *J. Electroceramics*, **13**, 691-695 (2004).
14. H. L. Tuller, "Ionic Conductors and Applications" in Handbook of Electronic and Optoelectronic Materials, Safa Kasap Ed., Springer, in press. Invited chapter.

15. H. L. Tuller, "Highly Conducting Ceramics," in *Ceramic Materials for Electronics*, 3<sup>rd</sup> edition, Ed. R. Buchanan, Marcel Dekker, New York, Basel, 2004, pp. 87-140. Invited chapter
16. A. Mitsos., I. Palou-Rivera and P.I Barton. "Alternatives for Micro Power Generation Processes", *Industrial & Engineering Chemistry Research*, **43**(1):74-84 (2004).
17. C. K. Lee, A. B. Singer and P. I. Barton, "Global Optimization of Linear Hybrid Systems with Explicit Transitions", *Systems & Control Letters*, **51**, 363-375 (2004).
18. P. I. Barton and Lee C. K., "Design of Process Operations Using Hybrid Dynamic Optimization", *Computers and Chemical Engineering*, **28** (6-7), 955-969 (2004).
19. V. T. Srikar, K. Turner, T.Y.A. Ie, and S. M. Spearing, "Structural Design Considerations for Micromachined Solid Oxide Fuel Cells," *Journal of Power Sources*, **125**(1), 62-69 (2004).
20. V. T. Srikar, Y. Peles, L. R. Arana, and S. M. Spearing "Self-Assembly of Micro- and Nanoparticles on Internal Micromachined Silicon Surfaces" *Sensors and Actuators A* **113**, 124-131 (2004)
21. T. Kraus, A. Günther, N. de Mas, M. A. Schmidt, K. F. Jensen, "An integrated multiphase flow sensor for microchannels," *Experiments in Fluids* **36**, 819-832 (2004)
22. A. Günther, S.A. Khan, M. Thalmann, F. Trachsel, and K.F. Jensen," Transport and Reaction in Microscale Segmented Gas-Liquid Flow, *RSC Lab on a Chip* **4** 278-286 (2004).
23. B. A. Wilhite, M.A. Schmidt and K.F. Jensen, "Palladium-Based Micromembranes for Hydrogen Separation: Device Performance and Chemical Stability," *Ind. Eng. Chem. Res.* **43**, 7083-7091 (2004).
24. C. D. Baertsch, M.A. Schmidt and K.F. Jensen, "Catalyst Surface Characterization in Microfabricated Reactors Using Pulse Chemisorption," *Chem. Comm.*, **22**, 2610 (2004).
25. T. S. Stefanik and H. L Tuller, "Praseodymium-Cerium Oxide as a Surface-Effect Gas Sensor, *J. Electroceramics*, **13**, 771-774 (2004).
26. A. Mitsos, M. M. Hencke and Barton P. I. "Product Engineering for Man-portable Power Generation Based on Fuel Cells", *AIChE Journal* , **51**, 2199-2219 (2005).
27. B. Chachuat, A.B. Singer and P.I. Barton "Global Mixed-Integer Dynamic Optimization", *AIChE Journal*, **51**, 2235-2253 (2005).
28. A. Günther, M. Jhunjhunwala, M. Thalmann, M. A. Schmidt, and K. F. Jensen, "Micromixing of Miscible Liquids in Segmented Gas-Liquid Flow," *Langmuir*, **21**, 1547-1555 (2005).
29. B. Chachuat, A. Mitsos and P.I. Barton "Optimal Design and Steady-state Operation of Micro Power Generation Employing Fuel Cells", *Chem. Engin. Sci.e*, **60**, 4535-4556 (2005).
30. F. Trachsel, A. Günther, and S. Khan, and K.F. Jensen, "Measurement of residence time distribution in microfluidic systems," *Chem. Eng. Sci.* **60** 5729 – 5737 (2005).

31. A. F. Lopeandia, L. I. Cerdó, M. T. Clavaguera-Mora, A. R. Arana, K. F. Jensen, F. J. Muñoz, and J. Rodríguez-Viejo, "Sensitive power compensated scanning calorimeter for analysis of phase transformations in small samples," *Rev. Sci. Instruments*, **76**, 065104-1-065104-5 (2005).
32. N. de Mas, A. Günther, T. Kraus, M.A. Schmidt, K. F. Jensen, "A Microfabricated Scaled-Out Multilayer Gas-Liquid Microreactor with Integrated Velocimetry Sensors," *Ind. Eng. Chem. Res.* **44**, 8997-9013 (2005).
33. K. F. Jensen, "Silicon Based Microreactors," in *Microreactor Technology and Process Intensification*, Y. Wang and J. Holladay (Eds.), *ACS Symp. Ser.* **914**, 2-22 (2005).
34. A. Bieberle-Hütter, H. L. Tuller, "Fabrication and Structural Characterization of Interdigitated Thin Film  $\text{La}_{1-x}\text{Sr}_x\text{CoO}_3$  (LSCO) Electrodes", *J. Electroceramics* **16**, 151-157 (2006).
35. K.F. Jensen, "Silicon based microchemical systems –Characteristics and applications," *Materials Research Society Bulletin* **31**, 101-107 (2006).
36. B.A. Wilhite, S.E. Weiss, J.Y. Ying, M.A. Schmidt, and K. F. Jensen, "High-purity hydrogen generation in a microfabricated 23 wt % Ag-Pd membrane device integrated with 8:1  $\text{LaNi}_{0.95}\text{Co}_{0.05}\text{O}_3$  / $\text{Al}_2\text{O}_3$  Catalyst," *Adv. Mater.* **18**, 1701–1704 (2006). (Highlighted in News and Views perspective in *Nature*, R.I. Masel, "Hydrogen quick and clean," *Nature*, 442, 521-2, 2006)
37. T. Hyodo, A. Bieberle-Hütter, J. L. Hertz and H. L. Tuller, "Three Dimensional Arrays of Hollow Gadolinia-doped Ceria Microspheres Prepared by R.F. Magnetron Sputtering Employing PMMA Microsphere Templates", *J. Electroceramics*, **17** (2-4): 695-699 (2006)
38. Anja Bieberle-Hütter, Martin Søgaaard and H. L. Tuller, "Electrical and Electrochemical Characterization of Microstructured Thin Film  $\text{La}_{1-x}\text{Sr}_x\text{CoO}_3$  Electrodes", *Solid State Ionics*, **177** (19-25): 1969-1975 (2006)
39. J. L. Hertz and H. L. Tuller, "Enhanced Pt Electrode Performance on YSZ Films with nm-Sized Grains," *Solid State Ionics* in press
40. L. R. Arana, N. de Mas, R. Schmidt, A. J. Franz, M. A. Schmidt and K. F. Jensen, "Isotropic etching of silicon in fluorine gas for MEMS micromachining," *J. Micromach. Micromec* in press

#### 11.1.2 Papers published in non-peer-reviewed journals or in conference proceedings

1. Joshua L. Hertz, Jyrki Lappalainen, Darja Kek, Todd Stefanik and Harry L. Tuller, Progress Towards an all Thin Film Fuel Cell for Portable Power Generation in Micropower and Microdevices (Proc.Vol.-25-2002), eds., E. J. Brandon, A. Ryan, J. Harb, and R. Ulrich, The Electrochemical Society, Pennington, NJ, (2002), pp. 137-145.
2. L. R. Arana, S. B. Schaevitz, A. J. Franz, K. F. Jensen, and M. A. Schmidt, "A Microfabricated Suspended-Tube Chemical Reactor for Fuel Processing," *Proceedings of*



- the Fifteenth IEEE International Conference on Microelectromechanical Systems*, New York (2002).
3. T. S. Stefanik and H. L. Tuller, "Electrical Conductivity in Praseodymium-Cerium Oxide", *Solid State Ionics-2002, MRS Symposium Proceedings, Vol. 756*, eds, P. Knauth, J.-M. Tarascon, E. Traversa and H.L. Tuller, Warrendale, PA, (2003), p163-168.
  4. L. R. Arana, S.B. Schaevitz, A. J. Franz, K. F. Jensen, and M.A. Schmidt, "A Suspended-Tube Microreactor for Thermally-Efficient Fuel Processing," International Conference on MicroReaction Technology MRET 6, New Orleans, LA (2002).
  5. K. F. Jensen, "Towards integrated microsystems for chemical synthesis" in *Micro Total Analysis Systems ( $\mu$ -TAS) 2002*, Y. Baba, S. Shoji, and A. van den Berg (Eds.). Kluwer, Dordrecht, The Netherlands, (2002), pp. 642-5
  6. R. Bouchet, P. Knauth, T. Stefanik, H. L. Tuller, "Impedance and Mott-Schottky Analysis of a  $\text{Pr}_{0.15}\text{Ce}_{0.85}\text{O}_{2-x}$  Solid Solution", *Solid State Ionics-2002, MRS Symposium Proceedings, Vol. 756*, eds, P. Knauth, J.-M. Tarascon, E. Traversa and H.L. Tuller, Warrendale, PA, (2003), p169-174.
  7. L. R. Arana, C. D. Baertsch, R. C. Schmidt, M. A. Schmidt, K. F. Jensen, "Combustion-Assisted Hydrogen Production in a High-Temperature Chemical Reactor/Heat Exchanger for Portable Fuel Cell Applications," 12th International Conference on Solid-State Sensors, Actuators, and Microsystems (Transducers '03), Boston, MA (2003).
  8. O. M Nielsen, L. R. Arana, C. . Baertsch, M. A. Schmidt, and K. F. Jensen, "A Thermophotovoltaic Micro-Generator for Portable Power Applications," TRANSDUCERS, Solid-State Sensors, Actuators and Microsystems, 12th International Conference on, 2003, Volume: 2 , 8-12 June (2003), pp.714-17.
  9. C. K. Lee and P. I. Barton, "Global Dynamic Optimization of Linear Hybrid Systems", in C.A. Floudas, editor "Frontiers in Global Optimization", Kluwer, pp. 289-312, (2003).
  10. N de Mas, A Gunther, M. A. Schmidt, K. F. Jensen, "Scalable microfabricated multiphase reactors for direct fluorination reactions," TRANSDUCERS, Solid-State Sensors, Actuators and Microsystems, 12th International Conference on, 2003 ,Volume: 1 , 8-12 June (2003) Pages 655 – 658
  11. T. Kraus, N. de Mas, A. Günther, M. A. Schmidt, and K. F. Jensen, "Integration of A Flow Regime Sensor into a Three-Dimensional Multichannel Microreactor," Proceedings of uTAS 2003 – Seventh International Conference on Miniaturized Chemical and Biochemical Analysis Systems, M.A. Northrup, K.F.Jensen, and D.J. Harrison (Eds.) Squaw Valley, CA, Transducers Research Foundation, (2003) pp. 809-812.
  12. A. Günther, M. Jhunjhunwala, M. A. Schmidt, and K. F. Jensen, "Liquid Mixing Using Inert Gas and an Integrated Gas-Liquid Separator," Proceedings of uTAS 2003 – Seventh International Conference on Miniaturized Chemical and Biochemical Analysis Systems, M.A. Northrup, K.F.Jensen, and D.J. Harrison (Eds.) Squaw Valley, CA, Transducers Research Foundation, (2003) pp. 465-468.
  13. C. K. Lee and P. I. Barton, "Determining the Optimal Mode Sequence", in S. Engell, H. Guéguen and J. Zaytoon, editors, "*Analysis and Design of hybrid Systems (2003)*", Elsevier pp. 123-128.

14. V. T. Srikar, Y. Peles, L. R. Arana, and S. M. Spearing, "Controlled Modification of Micromachined Silicon Surfaces Using Colloidal Micro- and Nanoparticles," 12th International Conference on Solid-State Sensors, Actuators, and Microsystems (Transducers'03), Boston, MA (2003).
15. T. Hyodo, J. Hertz and H.L. Tuller, "Preparation of Macroporous Noble Metal Films by RF Magnetron Sputtering for Electrochemical Device Applications", in Chemical Sensors VI: Chemical and Biological Sensors and Analytical Methods (Proceedings, Vol. 2004-08), The Electrochemical Society, Pennington, N.J., (2004), pp. 10-16.
16. A. Bieberle-Hütter, H. L. Tuller,  $\text{Ce}_{0.9}\text{Gd}_{0.1}\text{O}_2$  and  $\text{La}_{1-x}\text{Sr}_x\text{CoO}_3$  "Thin Films for Micro-SOFC", Proc. MIT-Tohoku "21COE" Joint Workshop on Nano Science in Energy Technology, Sept.27-28, (2004), MIT, Cambridge, MA. pp. O-12-1 to O-12-7
17. J. L. Hertz, A. Bieberle and H. L. Tuller, "Characterization of the Electrochemical Performance of YSZ Thin Films with Nanometer-Sized Grain Structure", Proc. MIT-Tohoku "21COE" Joint Workshop on Nano-Science in Energy Technology, Sept.27-28, (2004), MIT, Cambridge, MA. pp. O-11-1 to O-11-6
18. P. I. Barton, M. M. Hencke and A. Mitsos "Comparison of Man-Portable Power Generation Alternatives Based on Fuel-Cell Systems", Army Science Conference, Orlando Florida, Nov 29-Dec 2, (2004).
19. A. Mitsos and P.I. Barton "Optimal design and operation of fuel cell systems for micro-power generation", *FOCAPD 2004*, Princeton, New Jersey, 11-16 June, (2004).
20. P. I. Barton, A. Mitsos and B. Chachuat, "Optimal Start-up of Micro Power Generation Processes". In: C. Puigjaner and A. Espuña, editors, *Computer Aided Chemical Engineering*, 20B:1093-1098, Elsevier (2005).

### 11.1.3 Papers presented at meetings, but not published in conference proceedings

#### Invited:

1. P. I. Barton, C. K. Lee and A. B. Singer, "Mixed-integer Dynamic Optimization," Seventh SIAM Conference on Optimization, Toronto, Canada (May 2002)
2. H. L. Tuller, "Mixed Ionic-Electronic Conductors—A Review," Symposium on Mixed Ionic/Electronic Conductors, The 104th Meeting of the American Ceramic Society, St. Louis, MO (April 2002).
3. H. L. Tuller, "Electrical Conduction in Nano-structured Ceramics," Electroceramics VIII, Rome, Italy (Aug. 2002).
4. H. L. Tuller, "Defect Engineering: Design Tools for Solid State Electrochemical Devices," International Society of Electrochemistry 53rd Annual Meeting, Düsseldorf, Germany (Sept. 2002).
5. H. L. Tuller, "Thin Film Electrolytes: Application to Solid Oxide Fuel Cells," The Electrochemical Society Fall Meeting, Salt Lake City, UT (Oct. 2002).
6. L. R. Arana, C. D. Baertsch, R.C. Schmidt, M. A. Schmidt, K. F. Jensen, "Microchemical Reactors for Thermally Efficient Fuel Processing," Materials Research Society, Fall

Meeting, Boston, MA (Nov. 2002).

7. C. K. Lee and P. I. Barton, "Towards Global Optimization of Hybrid Dynamic Systems," SciCADE'03: International Conference on Scientific Computation And Differential Equations, Trondheim, Norway (30 June - 4 July 2003)
8. K. F. Jensen, "Microchemical Systems for Organic Synthesis and Separation" 4th International Forum on Chemistry of Functional Organic Chemicals (IFOC-4), November 2003, Tokyo, Japan.
9. K. F. Jensen, "Multiphase Phase Flows in Chemical and Biological Microsystems" International Symposium on Microchemistry and Microsystem 2003, November 2003, Tokyo, Japan.
10. J. Y. Ying, "Nanostructure Processing of Advanced Materials," Workshop on Nanoparticles Structural Design and Dispersion, Hsinchu, Taiwan, Oct. 2003. .
11. J. Y. Ying, "Nanostructure Processing of Advanced Catalysts and Biomaterials," Workshop on Molecular Functional Materials, Hong Kong, Oct. 2003.
12. J. Y. Ying, "Nanostructure Processing of Advanced Catalytic Materials," Symposium on 'New Materials and Concepts in Catalysis,' International Conference on Materials for Advanced Technologies, Singapore, Dec. 2003.
13. H. L. Tuller, "Electroceramics-Materials, Processing and Characterization: Application to Solid Oxide Fuel Cells" Internet Webcast, National Energy Technology Laboratory NETL, Morgantown, WV (June, 2003)
14. J. Y. Ying, "Nanostructure Processing of Advanced Catalysts and Biomaterials," Nanyang Technological University Convention on Nanotechnology, Singapore, March 2003.
15. J. Y. Ying, "Nanostructured Materials for Catalytic and Biomedical Applications," Symposium on 'Synthesis of Nanoparticles and Nanostructured Materials,' American Chemical Society National Meeting, New Orleans, Louisiana, March 2003.
16. J. Y. Ying, "Nanostructure Processing of Advanced Biomaterials and Catalysts," 10th International Conference on Composites/Nano Engineering, New Orleans, Louisiana, July 2003.
17. K. F. Jensen, "Characterization and Applications of Multiphase Microfluidics," Gordon Conference on Chemistry and Physics of Microfluidic Systems, Bozeman, MT (Aug. 2003).
18. H. L. Tuller, Todd Stefanik, "Novel Ceria Solid Solutions – Unusual Behavior Under Oxidizing Conditions" MRS Fall Meeting, Boston, November 29 - December 3, 2004
19. J. Y. Ying, "Nanostructure Processing of Advanced Catalytic Materials," Gordon Research Conference on 'Facilitated Chemical Synthesis,' Ventura, California, March 2004.
20. J. Y. Ying, "Nanostructure Processing of Advanced Materials," Symposium on 'Nanostructured Materials for Biomedical Applications,' The Minerals, Metals, and Materials Society Annual Meeting, Charlotte, North Carolina, March 2004.

21. J. Y. Ying, "Nanostructure Processing of Advanced Catalysts and Biomaterials," 7th International Conference on Nanostructured Materials, Wiesbaden, Germany, June 2004.
22. K. F. Jensen, "Microscale Synthesis – Integration of Reactions and Separations;" LabAutomation 2004, San Jose, CA, Feb 2004.
23. K. F. Jensen, MIT MURI program, Fuel Cell Power Sources and Systems, From Basics to the Battlefield, Univ. South Carolina, Feb 2004.
24. K. F. Jensen, "Chemical and Biological Microsystems," Frontiers of Technology, Industrial Research Institute, San Ramon, CA, March 2004.
25. J. Y. Ying, "Nanostructure Processing of Advanced Materials," 2nd International Conference on Technological Advances of Thin Films and Surface Coatings and 1st International Conference on Nanotechnology, Singapore, July 2004.
26. H. L. Tuller, "Thermal Management and Integration Challenges for Systems MicroReactor Based Micro Power," Thermal Management For Micro Power Sources Workshop sponsored by Army Research Office (ARO) and Defense Advanced Projects Research Agency (DARPA), Chicago, IL, May 2004
27. H. L. Tuller, "Microchemical Systems for Chemical and Materials Synthesis," Labfusion, Boston, MA, June 2004
28. H. L. Tuller, "Thin Film Solid State Ionics", Yonsei University, Dept. Ceramic Eng., Seoul, Korea, June 17, 2004
29. H. L. Tuller, "Future Challenges in Catalysis and Process Engineering," *Research Profile* of Technische Universiteit Eindhoven, Eindhoven, The Netherlands, June 2004
30. H. L. Tuller, "Synthesis and Manipulation of Nanoparticles in Microsystems," 13th Association of Crystallization Technology (ACT), North Chicago, October 2004
31. H. L. Tuller, "Integrated Microsystems for Synthesis and Separation," 4th Netherlands Process Technology Symposium (NPS4), Veldhoven, The Netherlands, October 2004
32. H. L. Tuller, "Opportunities in the Small," Session on Future of Chemical Engineering, Annual Meeting of the American Institute of Chemical Engineers (AIChE), Austin, TX, Nov. 2004
33. H. L. Tuller, "Advances in Multiphase Microreactors," Session in honor of Prof. Dudukovic's 60<sup>th</sup> (AIChE), Austin, TX, Nov. 2004
34. H. L. Tuller, "MicroReaction Technology for Energy Conversion," International Symposium on Micro/Nano Thermal and Fluids Systems, Tokyo, Japan, December, 2004
35. J. Y. Ying, "Nanostructure Processing of Advanced Catalysts and Biomaterials," Engineering Conferences International on 'Nanoparticles from the Vapor Phase Synthesis with Chemical and Biochemical Applications,' Davos, Switzerland, Aug. 2004.
36. J. L. Hertz, A. Bieberle, H. L. Tuller, "Processing and Electrochemical Characterization of Microstructured Thin Film Solid Oxide Fuel Cell Systems" 29<sup>th</sup> International Conference on Advanced Ceramics and Composites, January 23-28, 2005, Cocoa Beach, FL.
37. H. L. Tuller, "Materials Optimization and Characterization in Solid Oxide Fuel Cells" 6<sup>th</sup>

- Annual Solid State Energy Conversion Alliance (SECA) Workshop – April 17-20, 2005, Pacific Grove, CA
38. H. L. Tuller, “Integrated Ionics” International Conference on Electroceramics, ICE-2005, June 12-15<sup>th</sup>, 2005, Seoul, Korea
  39. H. L. Tuller, “The Marriage of Solid State Ionics and Electronics: Prospects for Micro-fuel cells, Micro-sensor Arrays and New Science”, 15th International Conference on Solid State Ionics, Baden-Baden, Germany, July 2005. *Plenary lecture*
  40. H. L. Tuller, “The Marriage of Solid State Ionics and Electronics: Prospects for Micro-Fuel Cells, Micro-Sensor Arrays and New Science”, Composites at Lake Louise, Canada-Oct. 2005.
  41. H. L. Tuller, “The Marriage of Solid State Ionics and Electronics: Prospects for Micro-Fuel Cells, Micro-Sensor Arrays and New Science”, The New England Section, The American Ceramic Society, Cambridge, MA, November, 2005.
  42. K. F. Jensen, “Microreactors for Catalyst Discovery and Applications,” 19th North American Catalysis Society Meeting, Philadelphia, Pennsylvania, May 2005. *Keynote lecture*.
  43. J. Y. Ying, "Nanostructure Processing of Advanced Catalysts," 19th North American Catalysis Society Meeting, Philadelphia, Pennsylvania, May 2005. *Keynote lecture*.
  44. J. Y. Ying, "Synthesis and Applications of Nanoporous Materials," Symposium on ‘Novel Porous Materials for Emerging Applications,’ 3rd International Conference on Materials for Advanced Technologies, Singapore, July 2005.
  45. J. Y. Ying, "Nanostructure Processing of Advanced Catalysts and Biomaterials," 7th World Congress of Chemical Engineering, Glasgow, Scotland, July 2005. *Plenary lecture. Chemical Engineering Science Danckwerts Lecture*.
  46. K. F. Jensen, “Micro-Reactors for High Throughput Experimentation,” Plenary Lecture, European Conference of Combinatorial Chemistry II, Winchester, UK, July 2005
  47. H. L. Tuller, “The Marriage of Solid State Ionics and Electronics: Prospects for Micro-Fuel Cells, Micro-Batteries and Micro-Sensor Arrays and New Science”, 8th Annual MIT in Japan Symposium, Tokyo, Japan, January 2006.
  48. H. L. Tuller, “Some Insights Derived from the Study of Lithographically Defined Electrodes”, U.S. Department of Energy- University of Florida High Temperature Electrochemistry Center Workshop: Fundamental Mechanisms of SOFC Cathode Reactions, Cocoa Beach, FL January, 2006.
  49. H. L. Tuller, “Micro-ionics: Prospects for Micro-fuel cells, Micro-sensor Arrays and New Science”, Pacific Northwest National Laboratory, Richland, WA., May, 2006
  50. H. L. Tuller, “Prospects for Micro-ionic Devices” National Microelectronics Centre Barcelona, Spain, June 23, 2006
  51. B.L. Wardle, “Fabrication and Performance of Solid Oxide Fuel Cell Microchemical Power Systems”, XV<sup>th</sup> International Materials Research Congress (IMRC), Cancun, Mexico, August 2006.

52. J. Y. Ying, "Nanostructure Processing of Advanced Catalysts," 7th Netherlands' Catalysis and Chemistry Conference, Noordwijkerhout, Netherlands, March 2006. .
53. J. Y. Ying, "Nanostructure Processing of Advanced Catalysts," CONCORDE Conference on 'Catalytic Nano-Oxides R&D in Europe: Present and Future,' Seville, Spain, May 2006.
54. J. Y. Ying, "Nanostructure Processing of Advanced Catalysts," 11th International Ceramics Congress and 4th Forum on New Materials, Sicily, Italy, June 2006.
55. J. Y. Ying, "Research and Commercialization of Nanostructured Catalysts and Biomaterials," Workshop on Commercialization of Nanotechnology: From Laboratory to Commercial Products, Hong Kong, June 2006.
56. K.F. Jensen, "The Role of Integrated Microsystems in Greening of Chemical Discovery and Development," "Catalysis and Biocatalysis in Green Chemistry, Cambridge, UK, December 2005
57. K.F. Jensen, "Integrated Microsystems for Synthesis and Separation."ACHEMA, Frankfurt, Germany, May 2006
58. K.F.Jensen, "Chemical and biological microsystems: A revolution in discovery and development," 17th International Congress of Chemical and Process Engineering 27-31 August 2006, Prague - Czech Republic

#### **Contributed:**

1. P. I. Barton and C. K. Lee, "Global Dynamic Optimization of Linear Time Varying Hybrid Systems", 3rd International DCDIS Conference on Engineering Applications and Computational Algorithms, Guelph, Ontario, 15-18th May, 2003
2. J. L. Hertz, A. Bieberle and H.L. Tuller, "Microstructured, Thin-Film Noble Metal Cathodes for Micro-Solid Oxide Fuel Cells," Microbattery and Micropower Systems, The Materials Research Society Fall Meeting, Boston, MA (December, 2003)
3. J. L. Hertz, T.S. Stefanik and H.L. Tuller, "Thin Film Materials for a Micro-Solid Oxide Fuel Cell," Electrochemically Active Materials, American Ceramic Society Annual Meeting, Nashville, TN (April 2003)
4. J. L. Hertz and H.L. Tuller, "Electrochemical Characterization of Thin Films for a Micro-Solid Oxide Fuel Cell," Solid State Ionics, The International Conference on Electroceramics, Cambridge, MA (August, 2003)
5. K. T. Turner, V. T. Srikar, T.Y.A. Ie, and S. Mark Spearing, "Design Considerations for Microscale Solid-Oxide Fuel Cells," Presented at MRS Fall Meeting, Symposium CC: Microbattery and Micropower Systems II, Boston, MA, December 2003
6. T. Kraus, A. Guenther, N. de Mas, M.A. Schmidt, and K.F. Jensen, "Flow regime sensing in microchemical systems," presented at the Seventh International Conference on Microreaction Technology, Lausanne, Switzerland, Sep. 2003
7. A. Guenther, M. Jhunjhunwala, T. Kraus, N. de Mas, M.A. Schmidt, and K.F. Jensen, "Gas-liquid flow and mass transfer in microchemical systems," presented at the Seventh

International Conference on Microreaction Technology, Lausanne, Switzerland, Sep. 2003

8. B. A. Wilhite, M.A. Schmidt, and K.F. Jensen, "Palladium Based Micromembranes for Hydrogen Purification: Influence of Material Selection upon Performance," presented at the Annual Meeting of the American Institute of Chemical Engineers, San Francisco, CA, Nov 2003
9. C. D. Baertsch, M. A. Schmidt, and K. F. Jensen, "Development of a Microfabricated Solid-Oxide Fuel Cell for Portable Power, "Experimental Analysis of Fuel Cell Behavior " presented at the Annual Meeting of the American Institute of Chemical Engineers, San Francisco, CA, Nov 2003
10. A. Guenther, M. Jhunjhunwala, M.A. Schmidt, and K.F. Jensen, "Gas-liquid Flow in Microchemical Systems," presented at the Annual Meeting of the American Institute of Chemical Engineers, San Francisco, CA, Nov 2003
11. A. Guenther, M. Jhunjhunwala, M.A. Schmidt, and K.F. Jensen, "Liquid Mixing in a Microdevice by Introduction and Subsequent Removal of an Inert Gas Stream," presented at the Annual Meeting of the American Institute of Chemical Engineers, San Francisco, CA, Nov 2003
12. M. Jhunjhunwala, T. Kraus, M.A. Schmidt, and K.F. Jensen, "Characterization of Multiphase Flow And Mass Transfer in Microfluidic Systems," presented at the Annual Meeting of the American Institute of Chemical Engineers, San Francisco, CA, Nov 2003
13. C. K. Lee and P. I. Barton, "Towards Global Optimization of Hybrid Dynamic Systems", SciCADE'03: International Conference on SCientific Computation And Differential Equations, Trondheim, Norway, 30th June-4th July, 2003
14. T. Kraus, N. de Mas, A. Guenther, M.A. Schmidt, and K.F. Jensen, "Development and Integration of a Flow Regime Sensor for Three-Dimensional Multichannel Microreactors," presented at the Annual Meeting of the American Institute of Chemical Engineers, San Francisco, CA, Nov 2003
15. J. Cui and J. Y. Ying, "Processing and Mechanical Properties of Nanostructured Yttria-Zirconia Ceramics," Materials Research Society Spring Meeting, San Francisco, California, April 2004.
16. D. Quinn, B.L. Wardle, S.M. Spearing, "Residual stress and microstructural evolution in thin film materials for a microfabricated solid oxide fuel cell (SOFC).", Presented at MRS Fall Meeting, Boston, MA, 2004
17. B. Chachuat, A. Mitsos, and P. I. Barton, Optimal Operation and Design of Micro Power Generation Processes, AIChE Annual Meeting, Austin, Texas, 7th-12th November, 2004
18. A. Mitsos, M. Hencke and P.I. Barton, Man-portable power generation based on fuel-cell systems, AIChE Annual Meeting, AIChE Annual Meeting, Austin, Texas, 7th-12th November, 2004
19. A. Mitsos, Hencke M. and P.I. Barton, Comparison of Man-Portable Power Generation Alternatives Based on Fuel-Cell Systems, Army Science Conference, Orlando, Florida, 29th November-2nd December, 2004

20. J. Lappalainen, D. Kek, H.L. Tuller and V. Lantto, Electronic Conductivity and Dielectric Properties of Nanocrystalline CeO<sub>2</sub> films, Finnish Physical Society
21. A. Bieberle-Hütter, H. L. Tuller, "Ce<sub>0.9</sub>Gd<sub>0.1</sub>O<sub>2</sub> and La<sub>1-x</sub>Sr<sub>x</sub>CoO<sub>3</sub> Thin Films for Micro-SOFC" Joint Workshop on Nano Science in Energy Technology, Sept.27-28, 2004, MIT, Cambridge, MA.
22. J. L. Hertz, A. Bieberle and H. L. Tuller, "Characterization of the Electrochemical Performance of YSZ Thin Films with Nanometer-Sized Grain Structure" Joint Workshop on Nano Science in Energy Technology, Sept.27-28, 2004, MIT, Cambridge, MA.
23. B. A. Wilhite, A. Mehta, D. Quinn, J. Hertz, M. Spearing, H.L. Tuller, M.A. Schmidt, and K.F. Jensen, "Development of a membrane-based solid-oxide fuel cell: Microfabrication and performance analysis," Annual AIChE Meeting, Austin, TX, Nov.2004
24. B. A. Wilhite, S.E. Weiss, J. Y. Ying, M. A. Schmidt, and K.F. Jensen,"Microchemical Systems for Hydrogen Generation: Portable Power Applications," Annual AIChE Meeting, Austin, TX, Nov. 2004
25. A. Günther, S. A. Khan, F. Trachsel and K. F. Jensen, "Transport in Microscale Segmented Flow," APS-DFD Meeting, Seattle, November 22, 2004
26. A. Bieberle-Hütter, M. Søgaaard, J. L. Hertz, H. L. Tuller, "Patterned, Thin Film Cathodes for Micro-SOFC" MRS Fall Meeting, Boston, November 29 - December 3, 2004
27. A. Mitsos, B. Chachuat and P. I. Barton, Microfabricated Fuel-Cell Systems: Sustainable Portable Power Generation Devices? Alliance for Global Sustainability, Annual Meeting 2005, Cambridge, 20-23 March 2005
28. A. Bieberle, J. L. Hertz, H. L. Tuller, "Electrochemical Characterization of YSZ and CGO Thin Films on Different Substrates for Micro-SOFC Applications" 29<sup>th</sup> International Conference on Advanced Ceramics and Composites, January 23-28, 2005, Cocoa Beach, FL.
29. J. L. Hertz, A. Bieberle, H. L. Tuller, "Freestanding, Thin-Film Membranes for Solid Oxide Fuel Cells" 29<sup>th</sup> International Conference on Advanced Ceramics and Composites, January 23-28, 2005, Cocoa Beach, FL.
30. T. Hyodo, A. Bieberle, J. L. Hertz and H. L. Tuller, "Preparation of Porous Oxide Films by r.f. Magnetron Sputtering for Electrochemical Device Applications" International Conference on Electroceramics, ICE-2005, June 12-15<sup>th</sup>, 2005, Seoul, Korea
31. A. Bieberle-Hütter, M. Søgaaard and H. L. Tuller, "Electrical and Electrochemical Characterization of Microstructured Thin Film La<sub>1-x</sub>Sr<sub>x</sub>CoO<sub>3</sub> Electrodes" International Conference on Solid State Ionics, July 17th - 22nd, 2005, Baden-Baden, Germany
32. J. L. Hertz and H. L. Tuller, "Enhanced Pt Electrode Performance on YSZ Films with nm-Sized Grains" International Conference on Solid State Ionics, July 17th - 22nd, 2005, Baden-Baden, Germany
33. B. Blackwell, B. Wilhite, L. Arana, O. Nielsen, K. Cheung, M.A. Schmidt, and K.F. Jensen, "Micro Reaction Technology for Energy Conversion," Eight International Conference on Microreaction Technology, Atlanta, GA, April 2005.



34. B.A. Wilhite, S.E. Weiss, J.Y. Ying, M.A. Schmidt and K.F. Jensen, "Microchemical Systems for Portable Hydrogen Generation," 19th North American Catalysis Society Meeting, Philadelphia, PA, May 2005
35. Chachuat B., Mitsos A., and Barton P. I. "Optimal Start-up of Micro Power Generation Processes Employing Fuel Cells", *AIChE Annual Meeting*, Cincinnati, Ohio, 30th October-4th November, 2005.
36. Mitsos A. and Barton P. I. "Parametric Mixed-Integer Linear Programming: The General Case." *AIChE Annual Meeting*, Cincinnati, OH. 30th October-4th November, 2005.
37. Mitsos A., Chachuat B. and Barton P. I. "A Design and Operation Methodology for Man-Portable Power Generation", *AIChE Annual Meeting*, Cincinnati, Ohio, 30th October-4th November, 2005.
38. W. S. Kim, A. Rothschild, J. Hertz, and H. L. Tuller , Novel Method for Fabricating of Nano-porous Platinum Thin Films, MRS, Boston, MA, November 28-December 2, 2005
39. J. L. Hertz, A. Rothschild, and H. L. Tuller "Air-Platinum-YSZ electrode mechanism using sputtered microelectrodes" , E-MRS Meeting, Nice, France, May 29- June 2, 2006
40. W. S. Kim, A. Rothschild, J. L. Hertz, W. C. Jung, and H. L. Tuller, "Nano-porous Pt and Pt/YSZ composite thin films for micro-SOFC electrodes", E-MRS Meeting, Nice, France, May 29- June 2, 2006
41. H. He and J. Y. Ying, "Steam Reforming of Propane over Nickel Aluminate," Materials Research Society Fall Meeting, Boston, Massachusetts, Nov. 2006.
42. J. Cui and J. Y. Ying, "Synthesis and Methane Combustion of Nanostructured Ytria-Zirconia Ceramics Composite," Materials Research Society Fall Meeting, Boston, Massachusetts, Nov. 2006.
43. A. Günther and K.F. Jensen, "Multiphase Microfluidics Near the Speed of Sound," The American Physical Society, 58th Annual Meeting of the Division of Fluid Dynamics, Chicago, Illinois
44. K.T. Deshpande, B.A. Wilhite, M.A. Schmidt, and K.F. Jensen,"Integrated Partial Oxidation and Purification Microsystems for Autothermal Production of Hydrogen from Methanol," *AIChE Annual Meeting*, Cincinnati, OH, November 2005.
45. Mitsos A. and Barton P. I. "The General Case of Parametric Optimization with Mixed-Integer Linear Programs" *Paraopt VIII: Parametric Optimization and Related Topics*, Cairo, Egypt, November 27<sup>th</sup>-December 1<sup>st</sup>,2005
46. K. F. Jensen, N. de Mas, A. Guenther, S. Khan, M. Kreutzer, and E.R. Murphy, "Multiphase Microreactors - Synthesis and Scaling," *AIChE Annual Meeting*, San Francisco, November, 2006
47. K. T. Deshpande, M. A. Schmidt, and K. F. Jensen, ,"Integrated Autothermal Micromembrane Fuel Processor for Fuel Cell Application," *AIChE Annual Meeting*, San Francisco, November, 2006

48. B. S. Blackwell, M. A. Schmidt, and K. F. Jensen, "Thermal Management in Devices for Portable Hydrogen Generation," AICHE Annual Meeting, San Francisco, November, 2006
49. Yunt M., Mitsos A., Chachuat B. and Barton P.I. "Design of Portable Power Generation Systems for Variable Power Demand", *AIChE Annual Meeting*, San Francisco, California, 12th November-17th November, 2006.
50. Mitsos A., Lemonidis P. and Barton P.I. "Global Solution of Bilevel Programs with Nonconvex Functions", *AIChE Annual Meeting*, San Francisco, California, 12th November-17th November, 2006.

#### **11.1.4 Manuscripts submitted, but not published**

~12 papers in preparation for submission

### **11.2 MURI Personnel**

#### **11.2.1 Graduate Students Supported**

1. Leonel Arana (ChE) (PhD, Intel)
2. Brandon Blackwell (ChE) (PhD candidate)
3. Peter Capazzoli (ME) (MSc, SpaceX Inc)
4. Kerry Cheung (EECS) (MSc, PhD candidate EECS)
5. Jeremy Chou (EECS) (MSc., AMD)
6. Jianyi Cui (DMSE) (PhD candidate)
7. Hong He (ChE) (PhD candidate)
8. Josh Hertz (DMSE) (PhD, NIST)
9. Andrew Ie (Aero) (MSc., Singapore)
10. Cha Kun Lee (ChE) (PhD, PB Chemicals)
11. Roger Lin (DMSE) (MSc. YankeeTek)
12. Ankur Mehta (EECS) (MSc, PhD candidate UC Berkely)
13. Alexander Mitsos (ChE) (PhD, Numerica)
14. Ole Nielsen (EECS) (PhD, Boose)
15. David Quinn (ME) (PhD candidate)
16. Todd Stefanik (DMSE) (PhD, Raytheon)
17. Kevin Turner (Aero) (PhD, Univ. Wisconsin)
18. Steven E. Weiss (ChE) (PhD, Ambion)
19. Namiko Yamamoto (Aero) (PhD candidate)

20. Mehmet Yunt (ME) (PhD candidate)

#### **11.2.2 Post Doctorates Supported**

1. Anja Bieberle (DMSE) (Assistant Professor ETH, Zurich)
2. Chelsey Baertsch (ChE) (Assistant Professor Purdue University)
3. Benoit Chachuat (ChE) (Assistant Professor EPFL, Lausanne)
4. Kishori Deshpande (ChE)
5. Axel Guenther (ChE) (Assistant Professor Univ. Toronto)
6. Woosik Kim (DMSE)
7. Avner Rothschild (DMSE) (Assistant Professor Technion-Israel Institute of Technology)
8. John Tolsma (ChE) (Numerica)
9. Benjamin Wilhite (ChE) (Assistant Professor University of Connecticut)
10. V. T. Srikar (Aero) (Assistant Professor McGill University)

#### **11.2.3 Faculty Supported**

1. Paul I. Barton - Chemical Engineering (ChemE) Klavs F. Jensen - Chemical Engineering (ChemE)
2. Martin A. Schmidt- Electrical Engineering and Computer Science (EECS)
3. Mark S. Spearing- Aeronautics and Astronautics (AERO) and University of Southampton, United Kingdom.
4. Harry L. Tuller- Materials Science and Engineering (DMSE)
5. Brian Wardle - Aeronautics and Astronautics (AERO)
6. Jackie Y. Ying - Chemical Engineering (ChemE) and Institute for BioEngineering and Nanotechnology, Singapore

#### **Other Research Staff Supported**

1. Smitha Mathews (partial support)

#### **11.2.4 Under Graduate Students:**

1. Henry A. Bergquist
2. Susan Fredholm
3. Michael Hencke
4. Ruth Misener
5. Namiko Yamamoto

## 6. Sunny Wicks

### 11.2.5 PhDs Awarded: 7

Leonel Arana:	Employed at Intel Thesis Title-“High-Temperature Microfluidic Systems for Thermally-Efficient Fuel Processing,”
Josh Hertz :	Employed at NIST Thesis Title- “Microfabrication Methods to Improve the Kinetics of the Yttria Stabilized Zirconia-Platinum-Oxygen Electrode”
ChaKun Lee:	Employed at BP Chemicals Thesis Title- “Global Optimization of Hybrid Systems”
Alexander Mitsos	Employed at Numerica Thesis title:“Man-Portable Power Generation Devices: Product Design and Supporting Algorithms” June 28, 2006
Todd Stefanik :	Employed at Raytheon Corp. Thesis Title-“Electrical Properties and Defect Structure of Praseodymium-Cerium Oxide Solid Solutions”
Kevin Turner	Employed at University of Wisconsin Thesis Title-“Wafer bonding : mechanics-based models and experiments”
Steve Weiss:	Thesis Title- “Catalysts and Materials Development for Fuel Cell Power Generation”

### 11.2.6 Master Degrees Awarded: 5

Jeremy Chou (EECS)  
 Roger Lin (DMSE)  
 Andrew Ie (Aero)  
 Ankur Metha (EECS)  
 Kerry Cheung (EECS)